HOKKAIDO UNIVERSITY

| | |
|---|---|
| Title | Initiation and propagation processes of internal fatigue cracks in beta titanium alloys |
| Author(s) | XUE, Gaoge |
| Degree Grantor | 北海道大学 |
| Degree Name | 博士(工学) |
| Dissertation Number | 甲第15619号 |
| Issue Date | 2023-09-25 |
| DOI | https://doi.org/10.14943/doctoral.k15619 |
| Doc URL | https://hdl.handle.net/2115/93116 |
| Type | doctoral thesis |
| File Information | XUE_Gaoge.pdf |

Hokkaido University Collection of Scholarly and Academic Papers : HUSCAP

# Initiation and propagation processes of internal fatigue cracks in beta titanium alloys

by

Gaoge XUE



A thesis submitted in partial fulfillment of the requirements for the degree of Doctor of Engineering

Examination Committee:

Takashi Nakamura

Motohiro Sato

Katsuhiko Sasaki

Kosuke Takahashi

Laboratory of Mechanical and Functional Materials

Division of Mechanical and Space Engineering

Graduate School of Engineering, Hokkaido University

## Abstract

Beta titanium alloys have received considerable attention as promising structural materials owing to their excellent mechanical properties and corrosion resistance. As they are increasingly used in the aerospace industry, research on their fatigue behavior has become important in recent years. Recently, internal fatigue fracture has been reported as a novel fatigue fracture mode. When the applied stress is lower than the conventional fatigue limit, a fatigue crack is initiated inside the material. In most high-strength materials, internal fatigue fractures are commonly reported in very high cycle fatigue (VHCF) where the number of cycles exceeds $10^7$ cycles. The “invisible” feature of internal fatigue crack leads to significant challenges in investigating its growth behaviors, leading to the phenomenon of VHCF that is yet to be fully clarified. Moreover, specifically in beta titanium alloys, internal fatigue fractures have been reported one and two orders earlier than in the VHCF regime. The abnormal early internal fatigue fracture brings a significant risk for industrial utilization.

The purpose of the present study is to investigate the characteristics of internal fatigue fractures and the internal crack growth behaviors in beta titanium alloys. The author integrally studied internal fatigue fracture through fractography, direct observation via synchrotron radiation computed tomography (SR-CT), and replicating internal fatigue crack behaviors by surface crack growth tests in a vacuum. The contents of this dissertation are as follows:

Chapter 1: The concept of VHCF associated with internal fatigue fracture, the background of beta titanium alloy with its research status in the VHCF field, and the objective of the present study are introduced.

Chapter 2: Fatigue properties and fractographic features of beta titanium alloys are exhibited. Under a positive stress ratio of 0.1, internal fatigue fracture occurs from $10^5$ cycles in beta titanium alloys, 100 times earlier than (alpha + beta) titanium alloys and high-strength steels. By fractography, multiple facets were observed at the crack initiation site, surrounded by a smooth area feature corresponding to the crack propagation process. Three facet initiation models were proposed based on the surface appearances and the 3D facet bonding patterns of the multiple facets.

Chapter 3: To non-destructively observe the inside of beta titanium alloys, SR-CT experiments were conducted at beamline code "BL20XU" at a synchrotron radiation facility "SPring-8" located in Hyogo, Japan. The details of the SR-CT system at BL20XU including micro-tomography (micro-CT) and nano-tomography (nano-CT), called multiscale SR-CT, are introduced. The optimization results for micro-/nano-CT regarding specimen configuration and imaging conditions are illustrated individually.

Chapter 4: An *in situ* piezoelectric fatigue testing system was developed for efficiently observing fatigue crack growth. A small surface crack growth test was conducted to establish the measurement technique of crack growth by *in situ* multiscale SR-CT and evaluate the accuracy. The crack status, propagation process, and initiation process were successfully obtained. Microstructural visualization and three-dimensional rendering were achieved on a crack in grain size. It showed that the early crack growth was heterogeneous and significantly affected by the microstructure, such as the grain boundary blocking.

Chapter 5: A full-life growth behavior of a naturally initiated internal fatigue crack was observed by multiscale SR-CT. Crack initiation and propagation contributed to 57% and 43% of the fatigue life, respectively. After specimen fracture, the crack

fronts at various cycles were superimposed on the fracture surface. The crack propagation process consisted of multiple facets formations and subsequent growth in the matrix corresponding to the smooth area. The multiple facets formations represented 95% of the crack propagation life, which was dominant in the internal crack propagation in the beta titanium alloy. Moreover, the factor that triggered crack growth associated with facets to the surrounding matrix was examined based on the crack opening and blunting behavior. In addition, the internal crack propagation rate in beta titanium alloy was found to be slower than its surface crack but was 20~100 times faster than the internal crack in the most widely used (alpha+beta) titanium alloys.

Chapter 6: In the case of crack propagation, to explain the significant difference in the internal crack propagation rate between beta and (alpha+beta) titanium alloys, the present study focused on the environment surrounding the internal crack. It was reported that in (alpha+beta) titanium alloys, the crack propagation rate decreased with the increase of vacuum level, and the internal crack has similarities with the crack in a high vacuum. To investigate the appropriate environment surrounding an internal crack in beta titanium alloy, crack propagation tests in a high vacuum were conducted. As a result, the crack propagation rate in a high vacuum is slightly slower than that in the air and agrees with that of the internal crack in beta titanium alloy. It can be concluded that between beta and (alpha+beta) titanium alloys, the environment surrounding the internal cracks is similar but leads to a significant difference in crack propagation behaviors. In other words, various crack mechanisms have different sensitivities against vacuum regarding crack propagation.

Chapter 7: The main findings obtained in the present study were summarized.

# Table List


| | | |
|---|---|---|
| **Chapter 2** | | |
| Table 2-1 | Chemical composition of Ti-22V-4Al (mass %) | 24 |
| Table 2-2 | Mechanical properties of Ti-22V-4Al alloy with different heat treatments | 25 |
| Table 2-3 | Characteristics of the major and minor facet | 40 |
| | | |
| **Chapter 3** | | |
| Table 3-1 | Imaging steps for optimizing the imaging conditions of Ti-22V-4Al | 61 |
| | | |
| **Chapter 4** | | |
| Table 4-1 | Mechanical properties of the applied CP material | 72 |
| Table 4-2 | Imaging conditions of micro-CT and nano-CT | 76 |
| Table 4-3 | $F_1$ values in terms of the crack geometry, $b/a$, and the ratio of the crack depth to the specimen radius, $b/r$ | 84 |
| | | |
| **Chapter 5** | | |
| Table 5-1 | Mechanical properties of the heat-treated alloy Ti-22V-4Al with FP microstructure | 95 |
| Table 5-2 | Imaging conditions of micro-CT and nano-CT | 99 |
| Table 5-3 | Characteristics of crack growth stages of the monitored internal crack | 119 |

# Figure List


| Chapter 1 | | | |
|---|---|---|---|
| Fig. 1-1 | | VHCF properties of an (α+β) titanium alloy | 3 |
| Fig. 1-2 | | The beta transition temperature, plots as a function of MoE for select titanium alloys | 6 |
| Fig. 1-3 | | Commonly applied method for investigating internal fatigue cracks | 8 |
| Fig. 1-4 | | The crack propagation rate by conventional fatigue tests and fractography on high-strength steel | 10 |
| | (a) | Schematic of the fracture surface | |
| | (b) | Derivation of the internal crack propagation rate | |
| Fig. 1-5 | | Internal crack propagation rate estimated by beach marks and the fatigue life on steel | 11 |
| | (a) | Beach marks on the fracture surface | |
| | (b) | Derivation of the internal crack propagation rate | |
| Fig. 1-6 | | Crack propagation rate in various vacuum conditions in Ti-6Al-4V | 13 |
| Fig. 1-7 | | Synchrotron radiation facility, SPring-8@Hyogo, Japan | 16 |
| Fig. 1-8 | | Schematic of the crack observation by multiscale SR-CT system. | 16 |
| Fig. 1-9 | | Structure of the dissertation | 19 |
| | | | |
| Chapter 2 | | | |
| Fig. 2-1 | | Microstructures of Ti-22V-4Al alloy with different heat treatments. | 24 |
| | (a) | Fine α-phase precipitation (FP) | |
| | (b) | Coarse α-phase precipitation (CP) | |
| Fig. 2-2 | | Specimen Configuration for fatigue tests | 25 |
| Fig. 2-3 | | The uniaxial hydraulic servo fatigue testing machine | 27 |
| Fig. 2-4 | | Scanning Electron Microscope, VE-9800 Keyence | 27 |
| Fig. 2-5 | | Fatigue properties of FP material in $R = 0.1$, $R = -0.5$ and $R = -1$ | 30 |

| | | | |
|---|---|---|---|
| Fig. 2-6 | | Fatigue properties of FP and CP material in $R$ = 0.1 and $R$ = −1 | 30 |
| Fig. 2-7 | | SEM images of fracture surface of FP material | 32 |
| | (a) | FP, Surface, $\sigma_{max}$=700MPa, $R$=-1, $N_f$=3.5×10$^4$ | |
| | (b) | FP, Internal, $\sigma_{max}$=975MPa, $R$=0.1, $N_f$=4.5×10$^6$ | |
| Fig. 2-8 | | Schematic of facet angle measurement | 34 |
| Fig. 2-9 | | Statistical characteristics of the facet angle in FP material plotted on a probability paper of normal distribution | 35 |
| Fig. 2-10 | | SEM images of multiple facets under positive stress ratio of FP material | 37 |
| | (a) | $\sigma_{max}$=1125MPa, $R$=0.1, $N_f$=6.5×10$^4$ | |
| | (b) | $\sigma_{max}$=975MPa, $R$=0.1, $N_f$=4.5×10$^6$ | |
| | (c) | $\sigma_{max}$=1000MPa, $R$=0.1, $N_f$=3.0×10$^5$ | |
| Fig. 2-11 | | SEM images of multiple facets under negative stress ratios of FP material | 40 |
| | (a) | $\sigma_{max}$=800MPa, $R$=-0.5, $N_f$=4.7×10$^6$ | |
| | (b) | $\sigma_{max}$=625MPa, $R$=-1, $N_f$=2.0×10$^7$ | |
| Fig. 2-12 | | Schematic of a fatigue crack growth process in beta titanium alloy | 40 |
| Fig. 2-13 | | Schematic of the vertical slope type $\sigma_{max}$=800MPa, $R$= −0.5, $N_f$=4.7×10$^6$ | 42 |
| | (a) | 3D-SEM image | |
| | (b) | 3D-model schematic image | |
| Fig. 2-14 | | Schematic of the horizontal slope type $\sigma_{max}$=975MPa, $R$=0.1, $N_f$=4.5×10$^6$ | 42 |
| | (a) | 3D-SEM image | |
| | (b) | 3D-model schematic image | |
| Fig. 2-15 | | Schematic of the peak type $\sigma_{max}$=1000MPa, $R$=0.1, $N_f$=3.0×10$^5$ | 44 |
| | (a) | 3D-SEM image | |
| | (b) | 3D-model schematic image | |
| Fig. 2-16 | | Schematic of the combination type $\sigma_{max}$=625MPa, $R$=−1, $N_f$=2.0×10$^7$ | 44 |

| | | | |
|---|---|---|---|
| | (a) | 3D-SEM image | |
| | (b) | 3D-model schematic image | |
| Fig. 2-17 | | SEM images of fracture surface of CP material | 46 |
| | (a) | CP, Internal, $\sigma_{max}$=900MPa, $R$=0.1, $N_f$=4.3×10$^5$ | |
| | (b) | CP, Internal, $\sigma_{max}$=875MPa, $R$=0.1, $N_f$=1.4×10$^6$ | |
| Fig. 2-18 | | Multiple facets in CP material. $\sigma_{max}$=875MPa, $R$=0.1, $N_f$=1.4×10$^6$ | 48 |
| | (a) | Facet surface feature | |
| | (b) | SEM 3D image (Slope) | |
| | | | |
| Chapter 3 | | | |
| Fig. 3-1 | | Multiscale SR-CT system at beamline BL20XU @SPring-8, Japan | 54 |
| Fig. 3-2 | | Schematic of relationship between imaging conditions and their effect on experiment | 57 |
| Fig. 3-3 | | Relationship between X-ray transmittance and specimen diameter of Ti-22V-4Al under 20keV, 30 keV and 37.7 keV | 57 |
| Fig. 3-4 | | Configuration of the needle-shape specimen for the optimization of imaging condition | 60 |
| Fig. 3-5 | | SEM image of the microstructure of the heat-treated CP material with coarse, acicular alpha-phase precipitation (the same as Fig. 2-1 (b)) | 60 |
| Fig. 3-6 | | Micro-CT images at various diameter of the needle-shape specimen under 37.7 keV (CP material) | 64 |
| | (a) | φ0.6 mm, X-ray transmittance: ~43% | |
| | (b) | φ1.2 mm, X-ray transmittance: ~19% | |
| | (c) | φ1.6 mm, X-ray transmittance: ~11% | |
| | (d) | φ1.7 mm, X-ray transmittance: ~9% | |
| | (e) | φ1.8 mm, X-ray transmittance: ~8% | |
| Fig. 3-7 | | Nano-CT-imaging conditions in terms of the exposure time (CP material; specimen diameter: 0.7 mm; X-ray energy: 30 keV; transmittance: ~18%). | 66 |
| | (a) | Exposure time: 1000 ms | |
| | (b) | Exposure time: 4000 ms | |

| | | | |
|---|---|---|---|
| Fig. 3-8 | | Nano-CT-imaging conditions in terms of the X-ray energy (CP material; specimen diameter: 0.2 mm; X-ray energy: 20 keV; transmittance: ~21%, exposure time: 1000 ms) | 67 |
| | | | |
| Chapter 4 | | | |
| Fig. 4-1 | | Configuration of the specimen (units: mm) | 72 |
| Fig. 4-2 | | SEM image of the microstructure of the heat-treated CP material with coarse, acicular alpha-phase precipitation (the same as Fig. 2-1 (b)) | 72 |
| Fig. 4-3 | | *In situ* piezo fatigue-testing setup | 74 |
| Fig. 4-4 | | Fatigue properties of the CP material under a stress ratio, $R = -1$ | 76 |
| Fig. 4-5 | | Schematic of the crack and relevant parameters | 77 |
| Fig. 4-6 | | Crack-initiation status (CP material) | 79 |
| | (a) | Crack-initiation location on the plane perpendicular to the loading axis, with the corresponding initiation life and crack length values | |
| | (b) | Crack-initiation location on the side-view of the specimen and the images of the cracks initiated on the virtual cross section parallel to the longitudinal direction | |
| Fig. 4-7 | | Propagation process of crack C-1: Micro-CT images projected on a plane perpendicular to the loading axis (CP material) | 81 |
| | (a) | 1000 | |
| | (b) | 1500 | |
| | (c) | 2000 | |
| | (d) | 3000 | |
| | (e) | 4000 | |
| | (f) | 5000 | |
| | (g) | 6000 | |
| | (h) | 7000 | |
| Fig. 4-8 | | Relationship between the crack length and number of cycles (CP material) | 82 |
| Fig. 4-9 | | Relationship between the aspect ratio of the crack, $b/a$, and crack length, $2a$ (CP material) | 84 |

| | | | |
|---|---|---|---|
| Fig. 4-10 | | Relationship between the crack propagation rate and the stress intensity factor range (CP material) | 86 |
| Fig. 4-11 | | Relationship between the crack initiation rate and the stress intensity factor range (CP material) | 88 |
| Fig. 4-12 | | 3D morphology of C-1 at 1500 cycles by nano-CT (CP material) | 90 |
| Fig. 4-13 | | Nano-CT images of main crack C-1 at 1500 cycles (CP material) | 91 |
| | (a) | Longitudinal section (parallel to crack length direction) | |
| | (b) | Longitudinal section (parallel to crack depth direction) | |
| | (c) | Crack projected on a plane perpendicular to the loading axis | |
| | (d) | Schematic of sectioning and projection view | |
| | | | |
| Chapter 5 | | | |
| Fig. 5-1 | | SEM image of the microstructure of the heat-treated alloy Ti-22V-4Al, with a homogenous and fine alpha-phase precipitation (FP material, the same as Fig. 2-1 (a)) | 95 |
| Fig. 5-2 | | Configuration of the small specimen (units: mm). | 95 |
| Fig. 5-3 | | Fatigue properties of the small specimen and 4 mm specimen in FP material. Test frequency is 120 Hz and stress ratio is $R = 0.1$ | 97 |
| Fig. 5-4 | | Propagation process of an internal crack is shown by projecting micro-CT images under 80% loading on a plane perpendicular to the loading axis in FP material (unit: cycles) | 102 |
| Fig. 5-5 | | Propagation process of an internal crack in its early stage is shown by projecting nano-CT images under 80% loading on a plane perpendicular to the loading axis in FP material (unit: cycles). Linear crack fronts are indicated by red arrows | 103 |

| | | | |
|---|---|---|---|
| Fig. 5-6 | | Magnified micro-CT images of the crack at $4.80 \times 10^5$ and $5.10 \times 10^5$ cycles (FP material). Linear crack fronts are indicated by red arrows | 103 |
| Fig. 5-7 | | 3D rendering results of the crack growth process (FP material) | 104 |
| Fig. 5-8 | | SEM fractography results (FP material) | 107 |
| | (a) | Low-magnification 2D-SEM image of fracture surface | |
| | (b) | High-magnification 2D-SEM image on the crack initiation site; the boundary separating the major and minor facet indicated by black arrow | |
| | (c) | 3D-SEM image with profile data at the largest gradient of the multiple facets indicated by white lines. The solid circles in the 3D-SEM image and profile graph indicate the same locations | |
| Fig. 5-9 | | 2D-SEM image superimposed with crack fronts under various number of cycles (FP material) | 110 |
| | (a) | High-magnification view of the crack initiation site | |
| | (b) | Low-magnification view of the fracture surface | |
| Fig. 5-10 | | Micro-CT images of the longitudinal sections of the internal crack illustrating the crack blunting process (FP material) | 113 |
| Fig. 5-11 | | Schematic of the crack blunting process during a fatigue test. Note that the increment of the crack length is not provided in the schematic | 114 |
| Fig. 5-12 | | Crack propagation rate with the crack growth stages and fraction of crack propagation life $N_p$ (FP material) | 118 |
| | | | |
| Chapter 6 | | | |
| Fig. 6-1 | | Fatigue properties between beta (FP, Ti-22V-4Al) and (alpha+ beta) titanium alloys (Ti-6Al-4V) in $R = 0.1$ | 125 |
| Fig. 6-2 | | Crack propagation rate of beta titanium alloy Ti-22V-4Al (FP material) and a dual-phase (alpha + beta) titanium alloy Ti-6Al-4V | 126 |
| Fig. 6-3 | | Specimen configuration for the crack growth test in vacuum. (unit: mm) | 128 |
| Fig. 6-4 | | Configuration of the small defect | 129 |
| | (a) | Shape on the fracture surface | |

| | | | |
|---|---|---|---|
| | (b) | Shape on the specimen surface | |
| Fig. 6-5 | | The ultra high vacuum fatigue testing machine | 131 |
| | (a) | Setup in the experimental room | |
| | (b) | Schematic of the testing machine system | |
| Fig. 6-6 | | Observation system of the crack growth test in vacuum | 132 |
| Fig. 6-7 | | Schematic of crack shape with relevant parameter (the same as Fig. 4-5) | 133 |
| Fig. 6-8 | | Relationship between the crack length 2*a* and the number of cycles *N* (FP material) | 135 |
| Fig. 6-9 | | Relationship between crack propagation rate d*a*/d*N* and stress intensity factor range Δ*K* with the surface crack in a high vacuum, surface crack (in air) by SR-CT and the internal crack by SR-CT (FP material) | 137 |
| Fig. 6-10 | | Relationship between crack propagation rate d*a*/d*N* and stress intensity factor range Δ*K* with the surface crack in air and a high vacuum for beta titanium alloy (FP material) and Ti-6Al-4V | 138 |
| Fig. 6-11 | | Dual-phase (alpha + beta) titanium alloy Ti-6Al-4V with equiaxed alpha grains and grains containing alternating lamellae of alpha and beta phases. Ave. grain size is 10 μm. | 141 |
| Fig. 6-12 | | Fracture surface image of an internal crack in Ti-6Al-4V ($R$ = 0.1, $\sigma_{max}$= 600 MPa, $f$ = 120 Hz) | 142 |
| | (a) | Low magnification image | |
| | (b) | High magnification image in Stage II-a | |

# Contents

**1. Introduction ..... 2**

**1.1 Very high cycles fatigue and internal fatigue fracture ..... 2**

**1.2 Beta titanium alloy ..... 4**

**1.3 Methodology in VHCF field ..... 7**

1.2.1 Fractography ..... 9

1.2.2 Surface crack growth test in vacuum ..... 12

1.2.3 Non-destructive inspection ..... 14

**1.4 Objective and structure of the present dissertation ..... 17**

**2. Fatigue properties and fractographic feature of beta titanium alloys ..... 22**

**2.1 Methodology ..... 22**

2.1.1 Material and specimen configuration ..... 22

2.1.2 Testing equipment and conditions ..... 26

**2.2 Fatigue test results ..... 28**

**2.3 Fractography results of FP material ..... 31**

2.3.1 Fracture surface characteristics ..... 31

2.3.2 Facet angle statistics ..... 33

2.3.3 Facet surface features in positive stress ratio ..... 36

2.3.4 Facet surface features in negative stress ratios ..... 38

2.3.5 Facet bonding patterns ..... 41

**2.4 Fractography results of material with coarse α-phase precipitation ..... 45**

2.4.1 Fracture surface characteristics ..... 45

2.4.2 Facet surface features and bonding pattern ..... 47

**2.5 Summary of Chapter 2 ..... 49**

**3. Multiscale SR-CT technique and the imaging condition optimization for beta titanium alloy ..... 52**

**3.1 System overview of multiscale SR-CT system of BL20XU@SPring-8 ..... 52**

**3.2 Optimization of imaging condition ..... 55**

3.2.1 The principle of determining the imaging condition. ..... 55

3.2.2 Experimental details for optimization ..... 58
**3.3 Micro-CT image under various imaging conditions. ..... 62**
**3.4 Nano-CT image under various imaging conditions. ..... 65**
**3.5 Summary of Chapter 3 ..... 68**
**4. *In situ* small crack growth test by multiscale SR-CT ..... 70**
**4.1 Methodology ..... 70**
4.1.1 Specimen configuration and material ..... 70
4.1.2 Instrumentation of fatigue testing setup ..... 73
4.1.3 Testing procedure ..... 75
**4.2 Crack initiation status ..... 78**
**4.3 Crack propagation process ..... 80**
4.3.1 Crack-shape evolution and the corresponding stress intensity factor ..... 83
4.3.2 Crack propagation rate ..... 85
**4.4 Crack initiation process ..... 87**
4.4.1 Crack initiation rate ..... 87
4.4.2 Crack initiation site in the microstructure ..... 89
**4.5 Summary of Chapter 4 ..... 92**
**5. Full-life growth behavior of a naturally initiated internal fatigue crack by multiscale SR-CT ..... 94**
**5.1. Methodology ..... 94**
5.1.1 Materials and specimens ..... 94
5.1.2 Fatigue properties of the FP small specimen ..... 96
5.1.3 Procedure for the *in situ* fatigue test and CT observations ..... 98
**5.2 Overall crack growth behavior via multiscale-CT ..... 100**
**5.3 Fractography features with regard to crack growth stages ..... 105**
**5.4 Comparison between fractography and SR-CT images ..... 108**
5.4.1 Stage I ..... 108
5.4.2 Stage II ..... 109
**5.5 Crack opening and blunting behavior during crack growth on multiple facets 111**
**5.6 Crack propagation rate ..... 115**
**5.7 Summary in Chapter 5 ..... 120**

**6. Effect of environment and microstructure on internal crack propagation .. 122**

**6.1 Comparison of fatigue properties and crack propagation behaviors between beta and (alpha + beta) titanium alloys ..... 122**

**6.2 Methodology ..... 127**

6.2.1 Material and Specimen ..... 127

6.2.2 Experimental setup and conditions ..... 130

**6.3 Crack propagation behaviors ..... 134**

6.3.1 Relation between crack length and the number of cycles ..... 134

6.3.2 Crack propagation rate ..... 136

**6.4 Microstructural factors in beta and (alpha + beta) titanium alloys related to various vacuum sensitivity on crack propagation ..... 139**

**6.5 Summary of Chapter 6 ..... 143**

**7. Conclusions ..... 146**

# Chapter 1

## Introduction

# 1. Introduction

## 1.1 Very high cycles fatigue and internal fatigue fracture

Fatigue fracture is the topic that always has the most concern in the field of material strength. Recently, when the number of load cycles exceeds $10^7$ where the conventional fatigue limit of the material is determined, it has been discovered that fatigue fractures still occur in metallic materials, and the fracture mode shifts from the surface into the interior originated (Fig. 1-1)[1]. This phenomenon, so-called very high cycle fatigue (VHCF), overturned the traditional concept that fatigue never exists when the stress is below its fatigue limit. In other words, the conventional fatigue safety design could not be considered safe anymore [2,3].

Internal fatigue fractures have been reported in many significant structural metallic materials such as high-strength steels [4–9], titanium alloys [1,2,10,11], aluminum alloys [12], magnesium alloys [13], etc. Due to the increasing demand for lighter equipment and the more severe operating conditions, the use of the above has increased, and elucidating the mechanism of VHCF as a safety issue is an urgent priority. However, previous studies found that internal fatigue cracks initiate from the fatal constitution on a micro-order scale. For instance, nonmetallic inclusions in high-strength steels and crystallographic grains in titanium alloys are recognized as the crack-initiation site with only several micrometers. Therefore, detecting “invisible” internal fatigue cracks of such a small size is still hindering the progress of cutting-edge VHCF research for decades, leading to the VHCF behaviors still not being thoroughly clarified and there is a lack of evaluation methods in the VHCF regime.

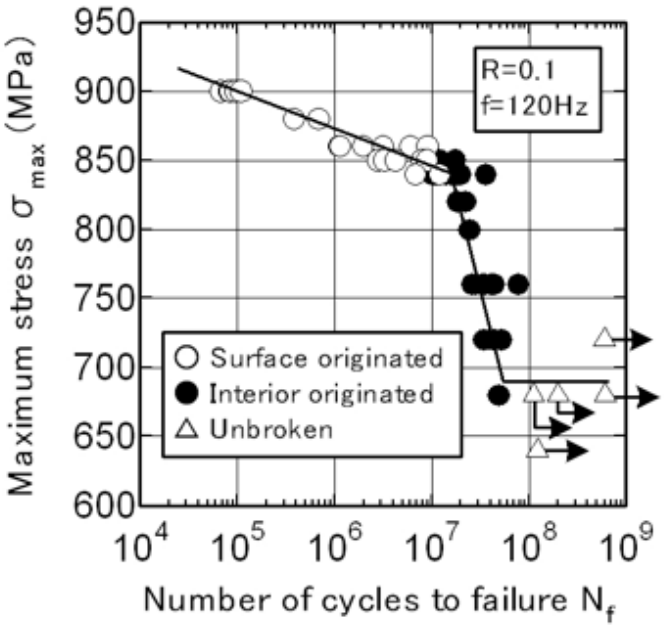



Fig. 1-1. VHCF properties of an (α+β) titanium alloy [1]

## 1.2 Beta titanium alloy

Pure titanium exists in the hexagonal close-packed structure (HCP) known as the alpha phase, and transforms to the body-centered cubic (BCC) known as the beta phase when the temperature is higher than 882 °C (beta transus temperature). A widely accepted definition of beta titanium alloy is: “A titanium alloy sufficiently rich in beta phase stabilizers that the beta phase can be retained untransformed by quenching from the beta phase field to room temperature”. Beta phase stabilizers are elements including V, Zr, Nb, Mo, Hf, Ta, etc., which can expand the beta phase field and shift the beta/(alpha+beta) phase boundary to lower temperatures [14]. The effect of beta phase stabilizers can be quantitively described by the Equivalent Molybdenum Value (MoE) which is shown as follows from <Handbook: Titanium Alloys ASM International>:

$$\begin{aligned} MoE = {} & 1.0(wt.\%\ Mo) + 0.67(wt.\%\ V) + 0.44(wt.\%\ W) + 0.28(wt.\%\ Nb) + \\ & 0.22(wt.\%\ Ta) + 2.9(wt.\%\ Fe) + 1.6(wt.\%\ Cr) + 1.25(wt.\%\ Ni) + 1.70(wt.\%\ \\ & Mn) + 1.70(wt.\%\ Co) - 1.0(wt.\%\ Al) \end{aligned} \qquad (1\text{-}1)$$

Fig. 1-2 shows the relationship between beta transus temperature with MoE for various beta titanium alloys [15]. With the increase of MoE, the transus temperature decreases, thus can lead to better stability of the beta phase in low temperature.

The advantage of beta titanium alloy is not only the common advantage of titanium alloy such as high corrosion resistance, but is also characterized by good cold workability and the highest specific strength among all types of titanium alloys. Therefore, they are increasingly used in the aerospace industry. There are some well-known cases of the utilization of beta titanium alloys: SR-71 “black-bird” was covered

by 93% of titanium alloys, and most of them are beta titanium alloy Ti-13V-11Cr-3Mo, which is also known as B120VCA. The first titanium strings were made from beta titanium alloy Ti-13V-11Cr-3Al and were introduced on the DC-10. The landing gear structures of Boeing 777, Airbus 340-500/600 were fabricated from Ti-10V-2Fe-3Al with a minimum ultimate tensile strength of 1193 MPa [14,16,17], research on their mechanical properties [18–21] and fatigue behavior has become important in recent years [10,11,19,21–34]. It is clear that the crack initiation and early crack propagation are from a crystallographic and microstructural sensitive regime [35].

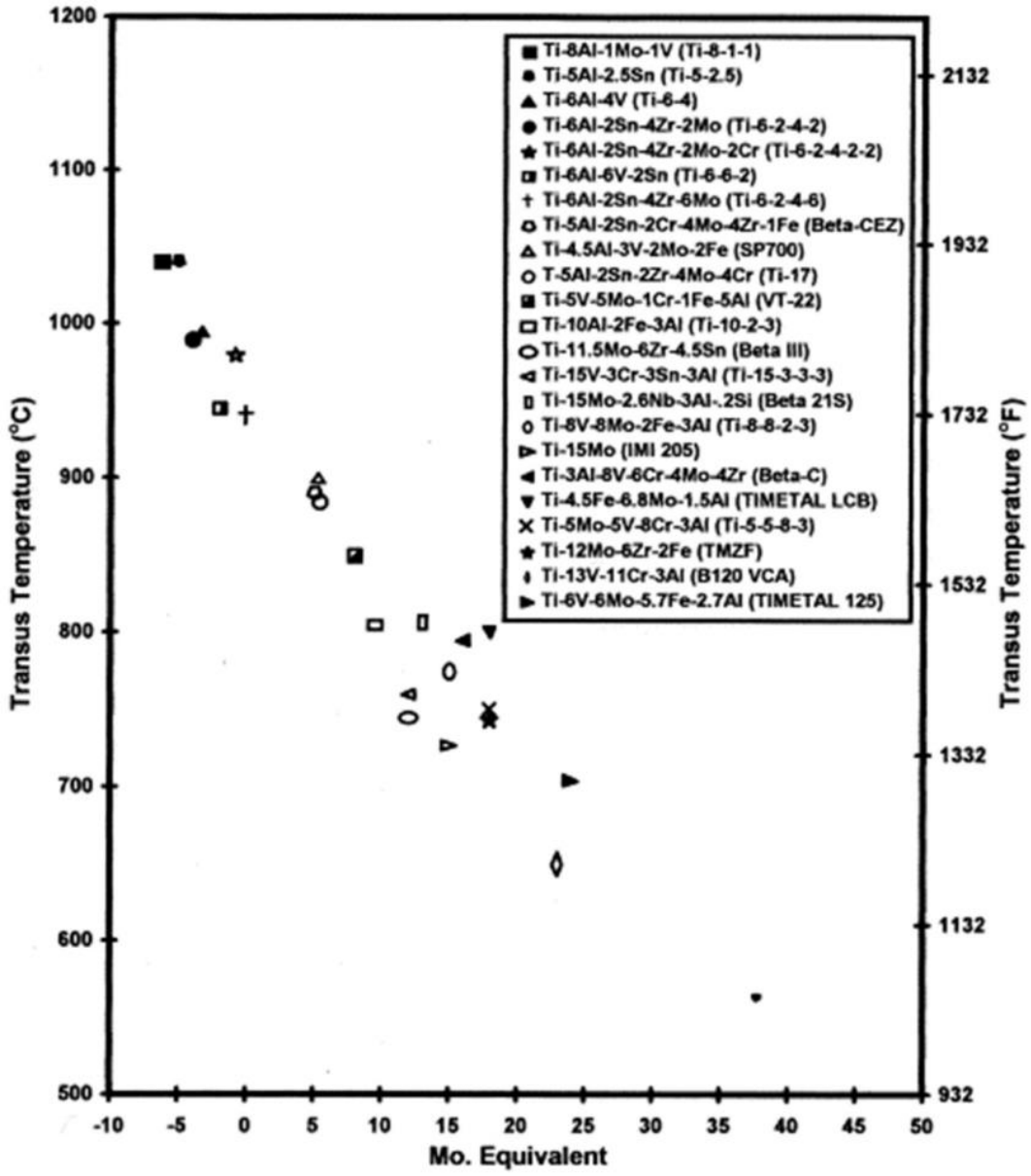



Fig. 1-2. The beta transition temperature, plots as a function of MoE for select titanium alloys [15]

## 1.3 Methodology in VHCF field

To understand VHCF, the initiation and propagation behaviors of internal fatigue cracks are indispensable. Basically, the experimental methodology on internal fatigue cracks can be classified into the indirect method and direct method as shown in Fig. 1-3. Indirect methods, such as fractography and replicating tests, are the most popular in the VHCF field because they can be easily carried out in laboratory conditions, but their validities are uncertain. On the other hand, the direct method simply means to non-destructively detect internal fatigue cracks. In the present study, synchrotron radiation X-ray computed tomography (SR-CT) was applied to directly observe internal fatigue behaviors. However, SR-CT is well-known for the difficulty of experiments, limited operation slots, enormous time consumption, and high financial cost. Meanwhile, applying either individual direct or indirect methods has limitations in revealing the mechanism of VHCF comprehensively. In this study, therefore, to avoid one-sided conclusions, the author simultaneously employed indirect and direct methods, including fractography, surface crack growth tests in a vacuum environment, and non-destructive inspection to explore the behavior of internal fatigue cracks. The details of the above will be introduced in the following content.

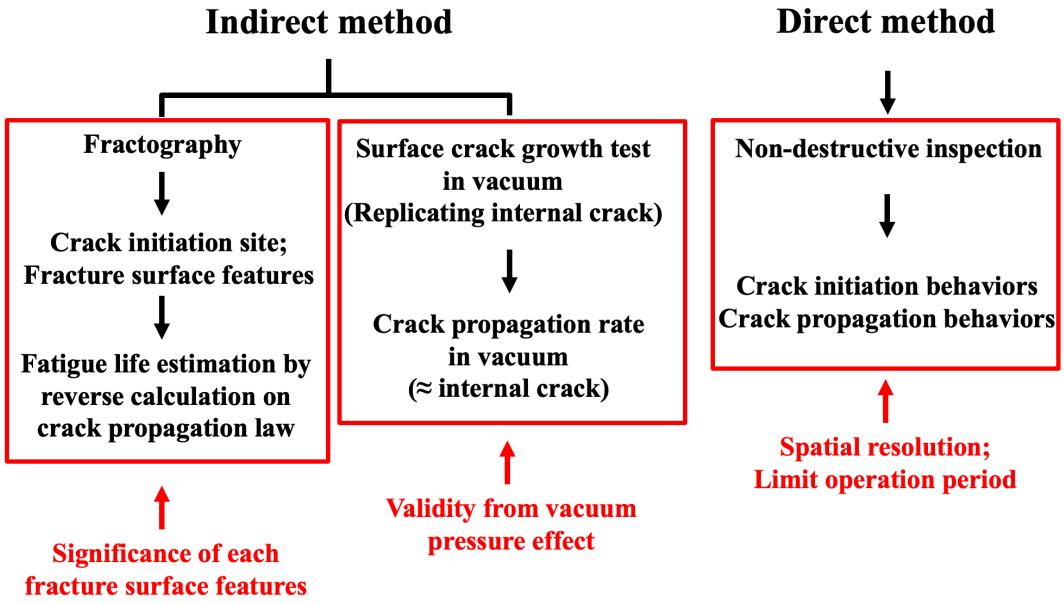
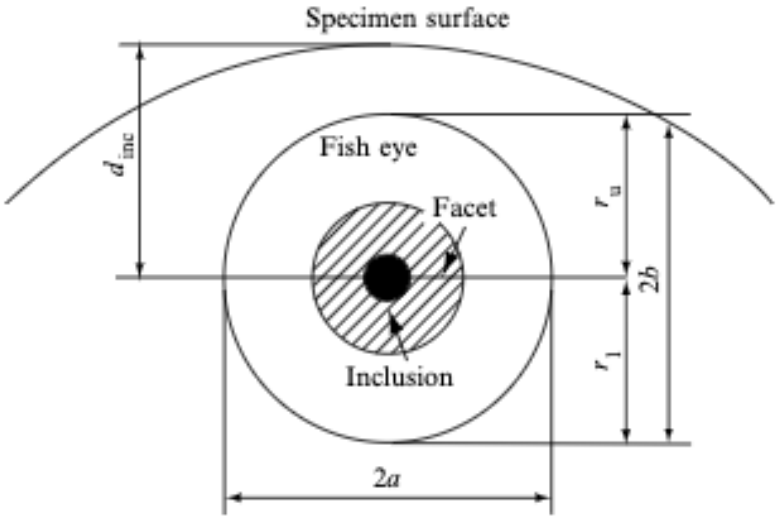


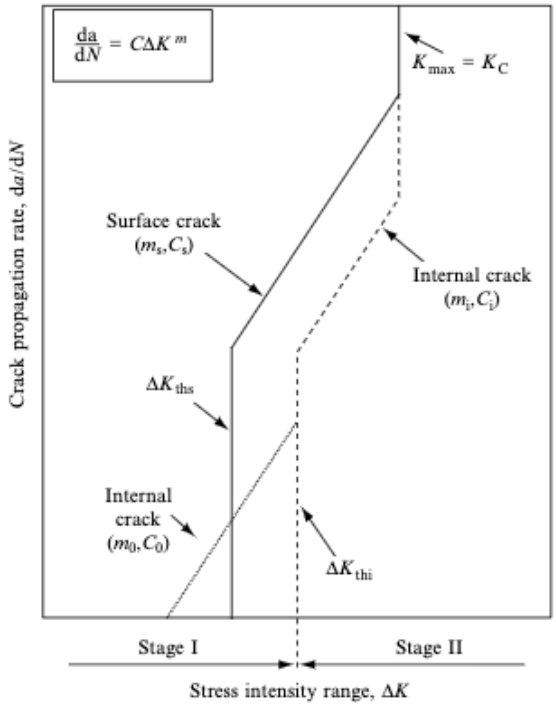

Fig. 1-3. Commonly applied method for investigating internal fatigue cracks

### 1.2.1 Fractography

Fractography analysis means observing the fracture surface after the specimen is fractured. By recognizing the crack initiation site and other remarkable fracture surface features, important parameters for describing internal fatigue crack behaviors such as the crack propagation rate, fatigue life, etc., can be estimated by the reverse calculation of crack propagation law (e.g. the Paris law). Some inspirational results have been published. Tanaka et al. tried to acquire the crack propagation rate by only conventional fatigue tests and fractography on high-strength steel (Fig. 1-4) [36]. Furuya et al. also established fractographic models such as beach marks for estimating the internal crack propagation rate and the fatigue life on steel (Fig. 1-5) [37,38]. The crucial point for fractography is to understand the significance of each fracture surface feature on fatigue properties, such as the fraction of fatigue life represented by each fracture surface feature. Meanwhile, correctly determining the real crack initiation site also strongly influences the accuracy of estimation. It is because the reverse calculation on crack propagation law is mainly based on the integral calculation, and the lower limit of the integral formula is related to the size of the crack initiation site.

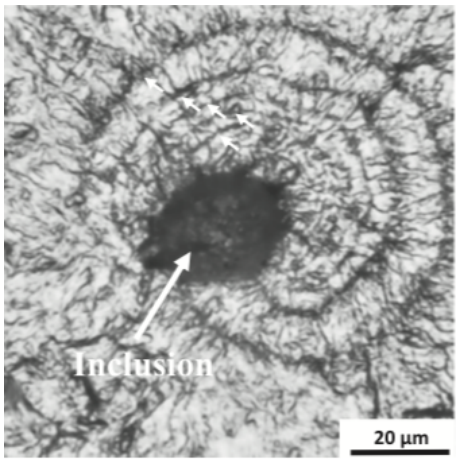



(a) Schematic of the fracture surface

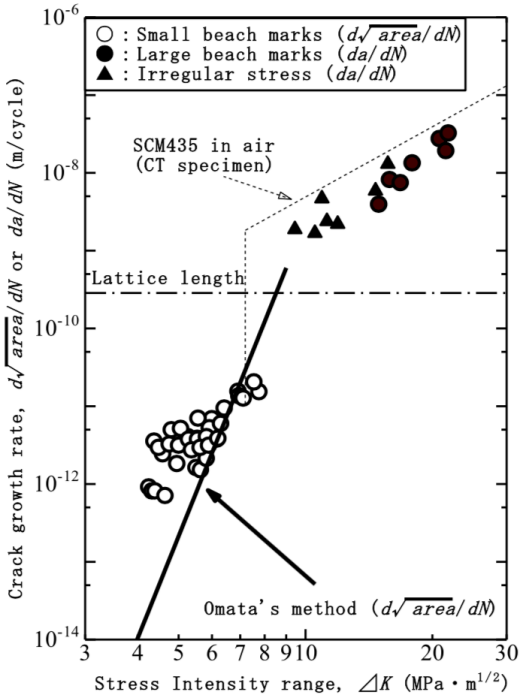



(b) Derivation of the internal crack propagation rate

Fig. 1-4. The crack propagation rate by conventional fatigue tests and fractography on high-strength steel [36]




(a) Beach marks on the fracture surface




(b) Derivation of the internal crack propagation rate

Fig. 1-5. Internal crack propagation rate estimated by beach marks and the fatigue life on steel [37,38]

### 1.2.2 Surface crack growth test in vacuum

Another example of an indirect method is to simulate the internal fatigue cracks' growth process by conducting surface crack growth tests under various vacuum pressures based on the idea that the environment around internal cracks is vacuum-like [39]. Previous studies have investigated the effect of a vacuum environment on the crack propagation of high-strength steels and titanium alloys [39–41]. On the basis of the results, the behaviors of surface fracture under vacuum, such as the crack propagation rate and fracture surface features, were found to have characteristics very similar to those of internal fractures. These phenomena show that it is acceptable to clarify the internal fracture mechanism by means of simulating surface fractures in a vacuum. However, some of the earlier studies, which were conducted primarily around the time of the Space Race, provided important results that the fatigue life of some alloys increased with decreasing vacuum pressure [42]. Gao et al. reported that on A7075 alloys, the crack propagation rate was sensitive to variations in vacuum pressure [43]. The previous study on Ti-6Al-4V also found that the crack propagation rate decreased with the decrease in vacuum pressure (Fig. 1-6) [44]. Therefore, it is not reasonable to summarize all vacuum conditions using only the word "vacuum", and it is necessary to investigate the crack growth behavior for various vacuum pressures. Because of the difficulty associated with measuring precisely the pressure around internal cracks, it is important to focus on the crack propagation behavior under various vacuum pressure conditions in order to simulate accurately internal fatigue cracks, and to help us to understand further the internal crack mechanism.

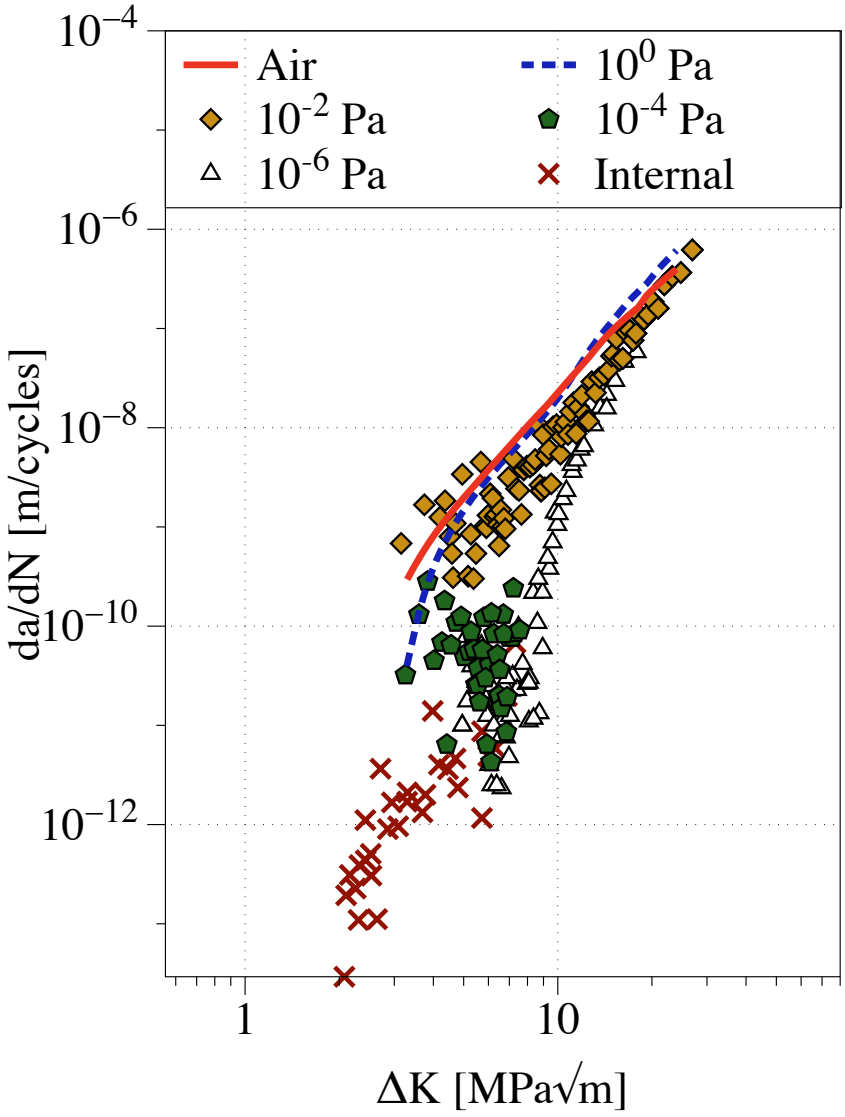



Fig. 1-6. Crack propagation rate in various vacuum conditions in Ti-6Al-4V [44]

### 1.2.3 Non-destructive inspection

Needless to say, the most effective way to investigate internal fatigue cracks is to detect them directly without fracturing the sample, or called a non-destructive inspection. Non-destructive inspection requires a form of energy that can penetrate the sample and be detectable by the meter or detector, such as sound, heat, and light. Accordingly, ultrasonic damage detection, thermal meter, and neutron radiation are widely developed to find the damage inside components for industrial utilization. However, conventional non-destructive inspection at the industrial level can hardly fulfill the requirement for the studies of internal fatigue cracks. One reason is that the target materials in the VHCF field are mostly metallic materials with high density, which makes the energy difficult to transmit through the sample. Another one is as mentioned in section 1.1, internal fatigue cracks can initiate from a very small size within a micrometer order, thus requiring an extremely high spatial resolution on the non-destructive inspection technique.

In recent years, SR-CT has emerged as a promising method for non-destructive detecting defects/inclusions in materials [45–48] and observing fracture processes [49–55]. Some studies on internal fatigue fractures have been conducted using microtomography (micro-CT). Messager et al. conducted *in situ* ultrasonic fatigue tests and captured the internal crack initiation from an artificial casting defect in an A357 Al alloy [51]. Yoshinaka et al. observed an internal crack initiation and propagation process in an (alpha + beta) titanium alloy Ti-6Al-4V and found that the internal crack propagated at an extremely slow rate (between $10^{-13}$ and $10^{-11}$ m/cycle) [53]. Chapman et al. evaluated surface and internal cracks in air and vacuum at elevated temperatures in a near-alpha titanium alloy [55]. Micro-CT provides a spatial resolution of the order of micrometers and a field of view (FOV) of the order of

millimeters, which are suitable for detecting initiated cracks in bulky specimens. However, a higher resolution is required to observe a just-initiated crack with microstructural effects. High-energy nanotomography (nano-CT) [56,57] has also been introduced, which provides a spatial resolution of approximately 200 nm and allows sufficient X-ray transmittance for sample sizes that are relevant to industrial applications. However, the narrow FOV of nano-CT makes it challenging to locate the initiated crack. Specifically, it is necessary to synthetically employ micro-CT and nano-CT to understand internal crack growth behavior from a very early stage. The previous studies successfully detected a small internal crack with the surrounding microstructure in Ti-6Al-4V using nano-CT [58] and observed a single carbon fiber transversely embedded in an epoxy sample [59].

In this study, the author employed a beamline BL20XU at SPring-8 (Fig. 1-7), a third-generation synchrotron radiation facility located in Hyogo, Japan [60], which enables multiscale tomography and provides both micro-CT and nano-CT [61]. As the schematic shown in Fig. 1-8 , Micro-CT was used to detect the crack initiation and propagation behavior. Nano-CT was applied to analyze the characteristics of just-initiated cracks. The details of the imaging system will be introduced in Chapter 3.



Fig. 1-7. Synchrotron radiation facility, SPring-8@Hyogo, Japan

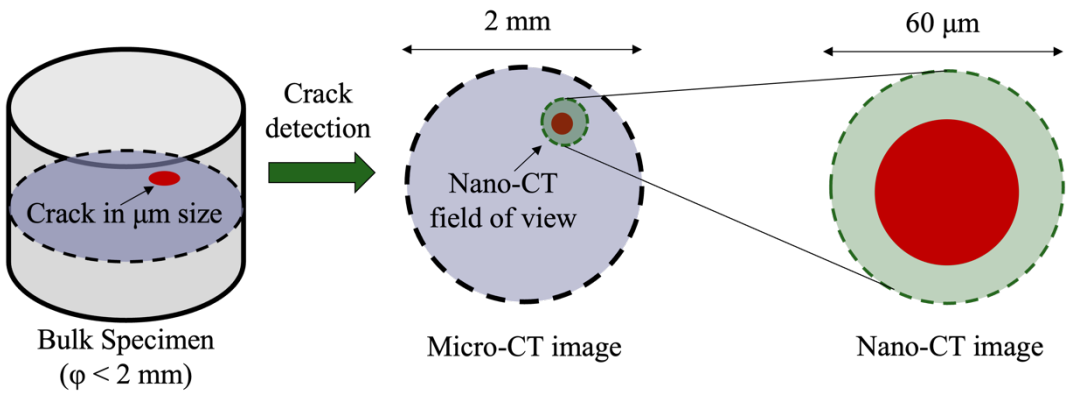



Fig. 1-8. Schematic of the crack observation by multiscale SR-CT system

## 1.4 Objective and structure of the present dissertation

The objective of the present study is to investigate the characteristics of internal fatigue fractures and the internal crack growth behaviors in beta titanium alloys.

The structure of the present dissertation is shown in Fig. 1-9. the author integrally studied internal fatigue fracture through fractography, direct observation via synchrotron radiation computed tomography, and replicating internal fatigue crack behaviors by surface crack growth tests in a vacuum.

In Chapter 2, basic fatigue tests were conducted to obtain the fatigue properties of the applied beta titanium alloy. Then, fractography was applied to recognize the fracture surface features and the crack initiation site.

Chapters 3, 4, and 5 describe the attempt at non-destructively and directly observing the interior information of beta titanium alloys using multiscale SR-CT. In Chapter 3, the content includes the details of the imaging system and the principle of determining imaging conditions for various imaging modes. In Chapter 4, the author tried to continuously observe small fatigue crack growth. An *in situ* piezoelectric fatigue testing system was developed. A small surface crack growth test was conducted to establish the measurement technique of crack growth by *in situ* multiscale SR-CT and evaluate the accuracy. In Chapter 5, the full-life internal fatigue crack behaviors were introduced, including the initiation life and propagation life of the internal fatigue crack. Meanwhile, the crack front was superimposed on the fracture surface, and the propagation rate of the internal fatigue crack was measured to understand the relationship between crack growth stages with the fracture surface features. In addition, the crack blunting behaviors were observed.

In Chapter 6, an indirect method which is to replicate internal fatigue crack growth behaviors by a crack growth test in a vacuum environment was conducted. The

crack propagation rate in a high vacuum was measured and compared with that of internal crack and surface crack in air. It was found that the crack propagation rate of internal crack and surface crack in a high vacuum are in good agreement. By discussing with (alpha+beta) titanium alloys, the environment surrounding the internal cracks is similar in beta and (alpha+beta) titanium alloys but leads to a significant difference in crack propagation behaviors. The microstructural factors which may influence the vacuum sensitivity on crack propagation in beta and (alpha+beta) titanium alloys was discussed.

In Chapter 7, the main findings obtained in the present study were summarized.

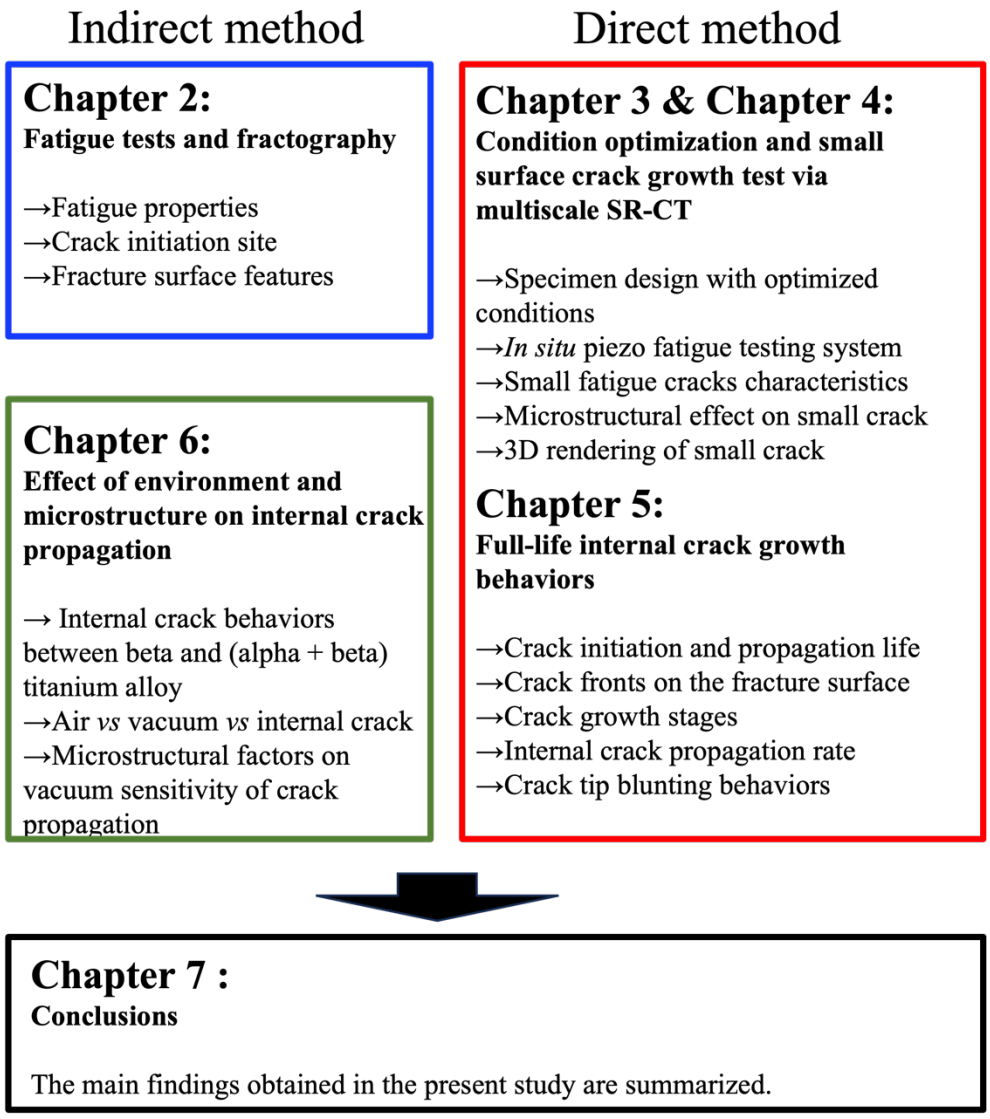



Fig. 1-9. Structure of the dissertation

# Chapter 2

## Fatigue properties and fractographic feature of beta titanium alloys

# 2. Fatigue properties and fractographic feature of beta titanium alloys

On a commercial beta titanium alloy, various heat treatments were conducted which provided two microstructures including a fine alpha phase precipitation and a coarse alpha phase precipitation. In this chapter, the fatigue properties of the different two heat-treated materials were investigated under various stress ratios. After fatigue test, fractography analysis was conducted to capture the fracture surface features. Multiple facets were observed at the crack initiation site regardless of microstructure, and their formation process was discussed.

## 2.1 Methodology

### 2.1.1 Material and specimen configuration

The material used in this study was a metastable β titanium alloy Ti-22V-4Al (Material code DAT51 [62]), and the chemical composition of this alloy is listed in Table. 2-1.

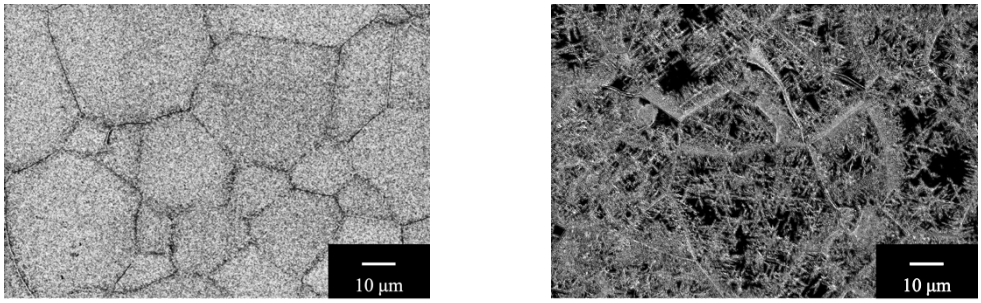
The as-received materials were Φ18 mm × 250 mm round bars. The heat treatment was designed as solution treatment (ST) at 1023K for 1 hour followed by water quenching, then proceeding to aging (A) at 823K for 4 hours followed by air cooling. Two different alpha phase precipitation, including fine precipitation (FP) and coarse precipitation (CP), was chosen in the present study. FP material has uniform alpha precipitates with nanometer scale inside the beta grain. On the other hand, CP material has a beta residual phase in the center of the grain and an acicular alpha phase near the grain boundary. To obtain the FP microstructure (Fig. 2-1 (a)), bars were set into an ambient temperature furnace and then heated gradually in both ST and A

(heating rate = 50 K/h). In the case of CP microstructure (Fig. 2-1 (b)), the bars were directly put into a pre-heated furnace which was set up at the target temperature (ST = 1023 K; A = 823 K), promoting the precipitation of a coarse α-phase. The average grain size of both heat-treated materials was approximately 20 μm. The mechanical properties of two heat-treated materials are measured by tensile tests and the results are shown in Table. 2-2. Specimens with a 6 mm diameter and 30 mm straight length were applied for the tensile tests. Three and five specimens were tested for FP and CP material, respectively. Strain control of 0.5%/min and stroke control of 3 mm/min (equivalent to 10%/min) were used in the tensile test before and after the yield point (elastic limit).

For the fatigue tests, the hourglass configuration was accepted to make specimens with a 4 mm diameter and 6mm straight length of control volume as shown in Fig. 2-2. To diminish the influence of work hardened layer caused by the lathe turning process, the specimen surface was finished by polishing with #120 to #2000 emery papers.

Table. 2-1. Chemical composition of Ti-22V-4Al (mass %)

| Al | V | Fe | C | O | N | H | Ti |
|---|---|---|---|---|---|---|---|
| 4.15 | 21.17 | 0.15 | 0.013 | 0.14 | 0.012 | 0.0124 | Bal. |




(a) Fine α-phase precipitation (FP) (b) Coarse α-phase precipitation (CP)

Fig. 2-1. Microstructures of Ti-22V-4Al alloy with different heat treatments.

Table. 2-2. Mechanical properties of Ti-22V-4Al alloy with different heat treatments

| | 0.2% Proof Stress [MPa] | Tensile Strength [MPa] | Elongation [%] | Reduction of Area [%] |
|---|---|---|---|---|
| FP | 1154 | 1235 | 9.3 | 21.9 |
| CP | 850 | 967 | 21.9 | 58.2 |

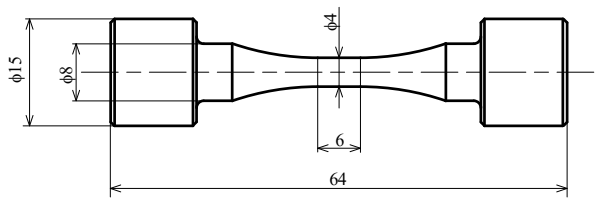



Fig. 2-2. Specimen Configuration for fatigue tests

2.1.2 Testing equipment and conditions

The fatigue tests were carried out by the uniaxial hydraulic servo fatigue testing machine shown in Fig. 2-3. The FP materials were tested under three stress ratios ($R = -1$; $R = -0.5$; $R = 0.1$), and CP materials were tested under two stress ratios ($R = -1$; $R = 0.1$). The load was provided as a sinusoidal wave under a frequency of 120 Hz. The experimental run-out was set at $10^8$ cycles.

The fracture surface features were observed by Scanning Electron Microscope (SEM) with a three-dimensional modeling function (VE-9800 Keyence, Fig. 2-4). The 3D images were created using two SEM images of the same position and magnification: one was taken by tilting the sample stage at 5° and the other without tilting. The resolution of the 3D images was approximately 100 nm/pixel so that it could reflect the fracture surface on a micrometer scale. The obtained SEM images were analyzed with the ImageJ image processing program [63].

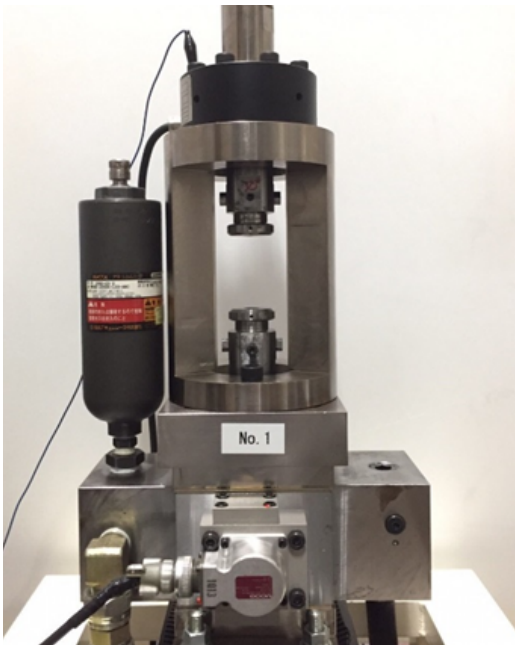



Fig. 2-3. The uniaxial hydraulic servo fatigue testing machine




Fig. 2-4. Scanning Electron Microscope, VE-9800 Keyence

2.2 Fatigue test results

Fig. 2-5 shows the *S–N* curves which is the relationships between the maximum applied stress ($\sigma_{max}$) and the number of cycles to fracture ($N_f$) for the different stress ratios of FP material.

When $R = -1$, the *S–N* curve exhibited a step-wise (or duplex) shape. In addition, the gradient of the *S–N* curve changed twice (the changing point is hereafter referred to as the "knee point"). First, the fracture mode of the specimens was a surface fracture mode in the high-stress regime, and the first knee point occurred at approximately $5\times10^4$ cycles. Then, a region in which surface fracture does not occur, which represents the fatigue limit of surface fracture, lasted until $2\times10^7$ cycles, which is regarded as the second knee point. After the second knee point, the fracture mode of the specimens changed into an internal fracture. Similarly, when $R = -0.5$, the *S–N* curve of the specimens exhibited a step-wise shape. In addition, the first knee point at $R = -0.5$ occurred at a similar cycle as $R = -1$. However, the second knee point characterized by internal fracture appeared earlier than $R = -1$. In contrast to $R = -1$ and $R = -0.5$, when $R = 0.1$, only one surface fracture was obtained, and it was difficult to accurately determine the first knee point, leading to an asymptotic shape of the *S–N* curve under $R = 0.1$. In addition, run-out was observed at 950 MPa, which was 82.3% of the proof stress. For comparison, the run-out stress under the same stress ratio and test frequency in a bimodal (alpha + beta) titanium alloy Ti-6Al-4V was 75.6% of the proof stress. Therefore, the applied beta titanium alloy has a pronounced fatigue strength among titanium alloys.

Fig. 2-6 shows a comparison of fatigue properties between FP and CP materials under $R = -1$ and $R = 0.1$. The tests of CP material have not reached in internal fractures regime in $R = -1$, and have not reached until run-out in $R = 0.1$. By comparing

the *S-N* data under the same stress ratio, the *S-N* curve of CP shows a similar trend to that of FP in terms of stress ratios. The earliest fatigue life for internal fracture appears slight longer in CP material than FP material.

In summary, for both FP and CP materials, when the stress ratios are negative, *S-N* curve is considered as a step-wise (or duplex) shape. However, with the stress ratios increasing, the fatigue limit of surface fractures becomes less pronounced, and the *S-N* curve finally exhibits an asymptote shape in a positive stress ratio. In addition, in the positive stress ratio, the internal fatigue fractures can be found in the $10^5$ cycles regime, which is much earlier than the VHCF regime. These observations are consistent with the findings of Shiozawa et al., indicating that the trend in Fig. 2-5 and Fig. 2-6 is a common fatigue characteristic of beta titanium alloys [11]

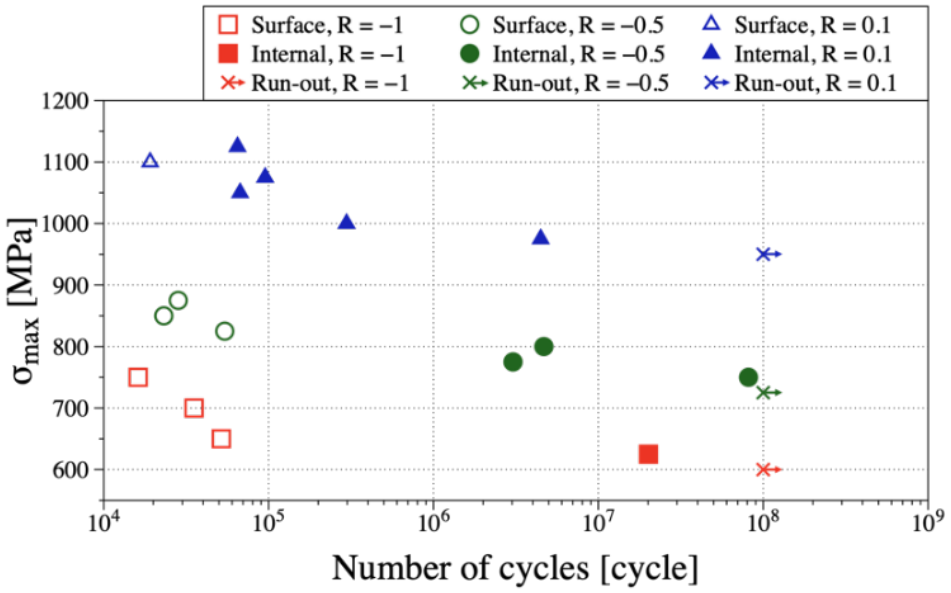



Fig. 2-5. Fatigue properties of FP material in $R = 0.1$, $R = -0.5$ and $R = -1$

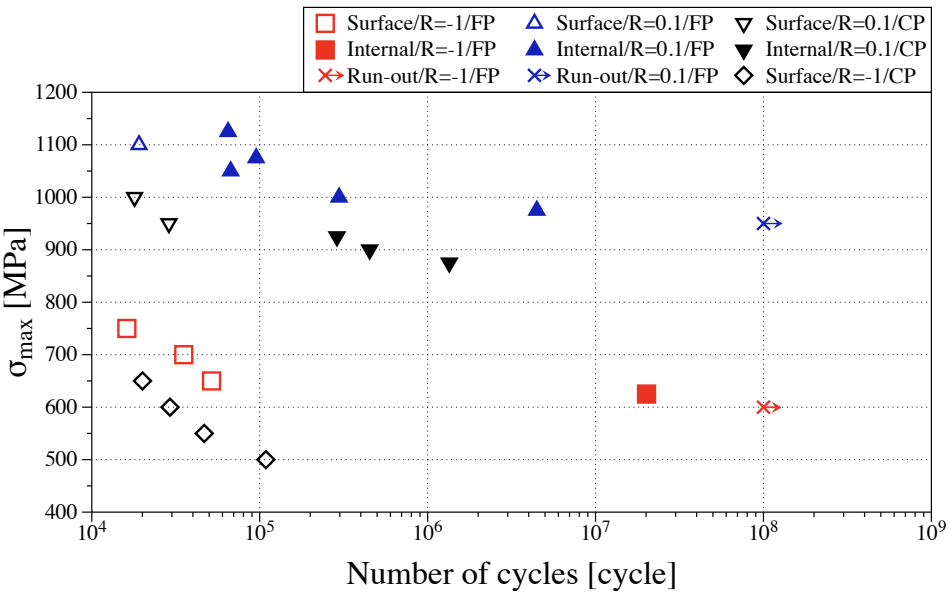


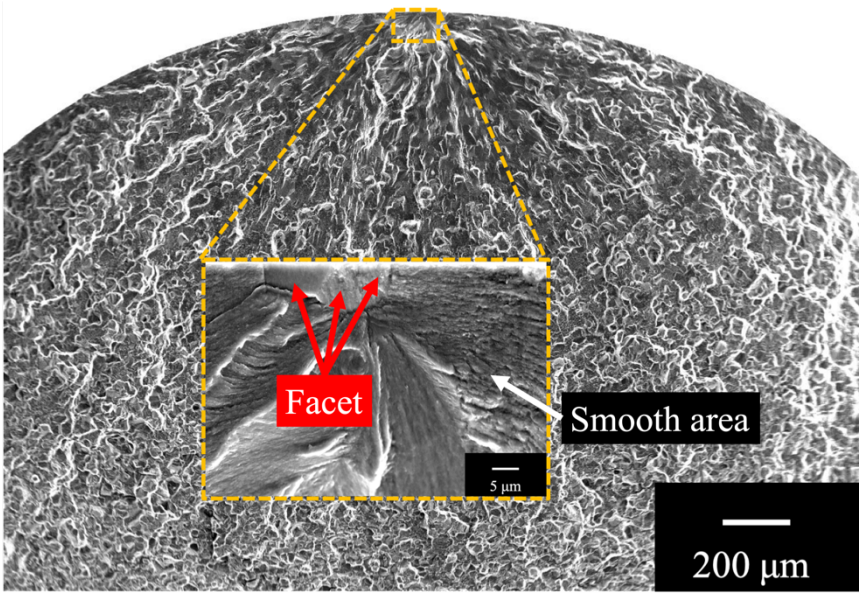

Fig. 2-6. Fatigue properties of FP and CP material in $R = 0.1$ and $R = -1$

## 2.3 Fractography results of FP material

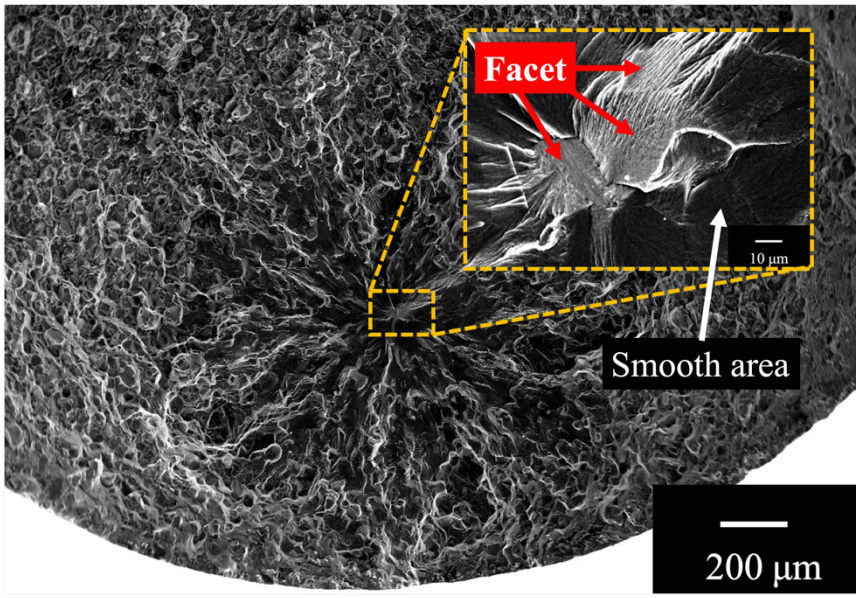
### 2.3.1 Fracture surface characteristics

Fig. 2-7 exhibits the surface and internal fracture images of FP materials. Only one fracture initiation site is observed without inclusions in each specimen regardless of stress ratios. Radial patterns initiated from the crack initiation site are confirmed on the fracture surfaces [25,64].

At the crack initiation site, crystallographic flat surfaces with grain-like boundary, so-called facets, are observed. Additionally, in most cases are multiple facets (14 of 16). Unlike the dispersive characteristic in Ti-6Al-4V [65], the multiple facets in Ti-22V-4Al connect each other as a whole part. Around crack initiation site, the morphology represented a smooth texture, defined as a “smooth area” in the present study. Similar characteristics of fracture surfaces in beta titanium alloys have also been exhibited in other articles [10,11,29,33].




(a) FP, Surface, $\sigma_{max}$=700MPa, $R$=-1, $N_f$=3.5×10$^4$




(b) FP, Internal, $\sigma_{max}$=975MPa, $R$=0.1, $N_f$=4.5×10$^6$

Fig. 2-7. SEM images of fracture surface of FP material

2.3.2 Facet angle statistics

The schematic of facet angle measurement is shown in Fig. 2-8. The facet angle $\theta$ was calculated from the arc tangent of the vertical height and horizontal length. A total of 41 facets were measured, and the measured angles were plotted into a normal distribution paper regardless of the fracture mode, as shown in Fig. 2-9. The cumulative probability was calculated using Eq. (2-1).

$$F_i(\theta_i) = i/(n+1) \ (i = 1,2,\ldots,41) \tag{2-1}$$

where $F_i$ is the cumulative probability, $\theta_i$ is the angle of facet, and "$n$" is the sample's capacity, which is 41 in this equation. The plots in the normal distribution probability paper showed a clear linear relationship, indicating that the measured facet angles strongly obey a normal distribution ($R^2$ = 98.99%). In addition, the average value of the facet angle was 44.7° with a standard deviation of 5.4°, which indicates that slip deformation was the dominant mechanism for the facet formation.

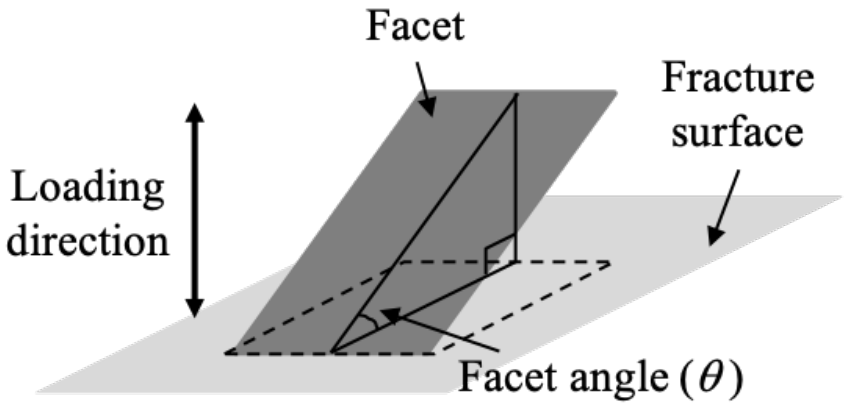



Fig. 2-8. Schematic of facet angle measurement

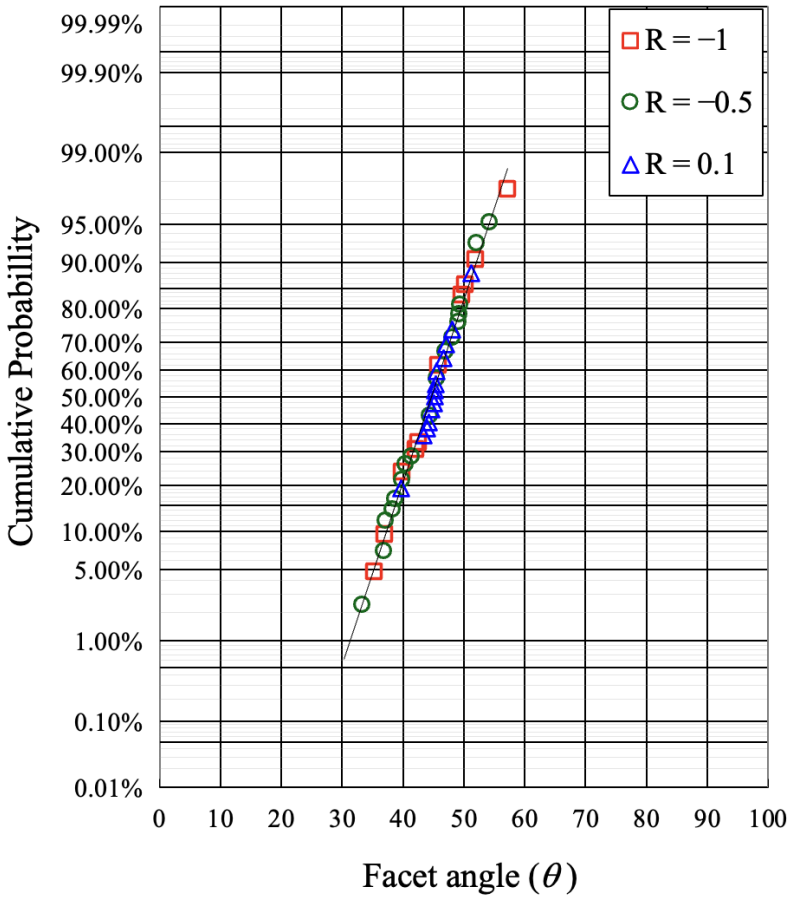
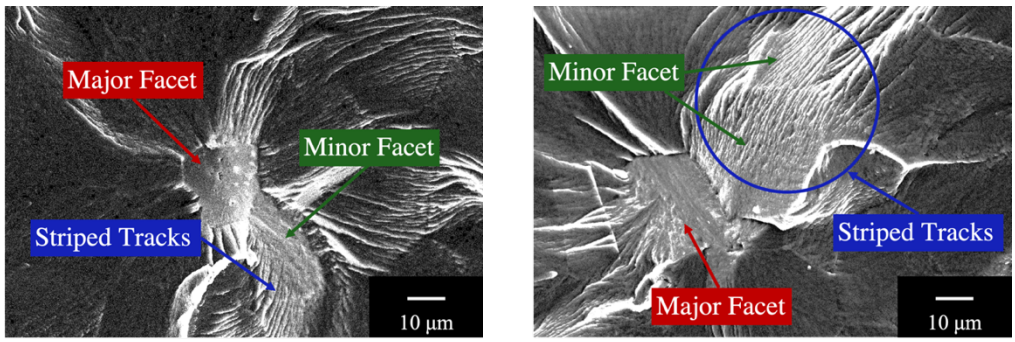



Fig. 2-9. Statistical characteristics of the facet angle in FP material plotted on a probability paper of normal distribution

2.3.3 Facet surface features in positive stress ratio

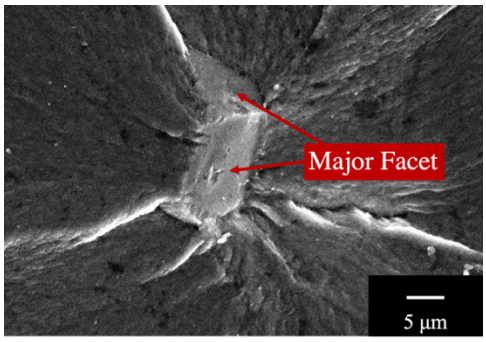
Fig. 2-10 shows the SEM images of multiple facets of the internal fracture under a positive stress ratio. The observed facets were classified into two types based on their surface features: First, facets with smooth surfaces, which were observed in all specimens. The other facet type was randomly distributed facets with obvious striped tracks on their surfaces. These results indicated that the facets with smooth surfaces were the crack-initiating facets. Therefore, in this study, to describe the role of various facets in the crack initiation process, the facet with smooth surfaces were defined as the “major facet,” and the facet with striped tracks was defined as the “minor facet”.

Based on the facet boundaries, the major facet had a relatively clearer grain-shaped boundary compared with the minor facet. This phenomenon can be attributed to the restrain of the grain boundary. Because the first facet is formed at a grain size, the slip band in the first facet formation was smaller than the grain size. Tanaka et al., J Lankford et al., and Zhai et al. reported the that the grain boundary blocking effect on slip bands is significant when the length of the slip band is on or below the order of the grain size [66–68]. This suggested that the major facet was the first generated facet, and the grain boundary blocking effect played a significant role during the major facet formation process. However, as the crack propagation proceeded, the length of the slip band during the minor facet formation increased, thus diminishing the blocking effect of the grain boundary. This was further confirmed by the unclear boundary of the minor facet.




(a) $\sigma_{max}$=1125MPa, $R$=0.1, $N_f$=6.5×10$^4$

(b) $\sigma_{max}$=975MPa, $R$=0.1, $N_f$=4.5×10$^6$




(c) $\sigma_{max}$=1000MPa, $R$=0.1, $N_f$=3.0×10$^5$

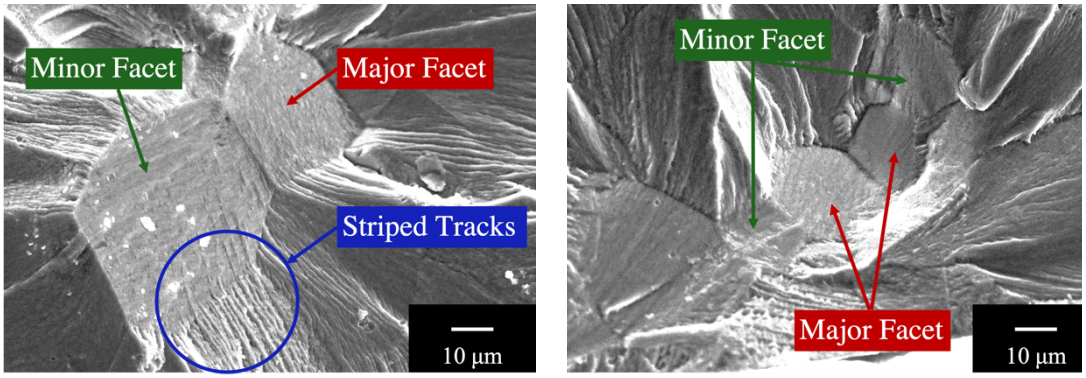
Fig. 2-10. SEM images of multiple facets under positive stress ratio of FP material

2.3.4 Facet surface features in negative stress ratios

Fig. 2-11 shows the 2D-SEM images of the multiple facets of the internal fracture under negative stress ratios. Similar to the fractographic results obtained under a positive stress ratio, major facet(s) with a smooth surface and clear grain-shaped boundary, and minor facet(s) with striped tracks were observed. However, compared with the striped tracks of the minor facet surfaces under positive stress ratios (Fig. 2-10), those under negative stress ratios were less remarkable (Fig. 2-11). This phenomenon can be explained by the fact that the striped tracks on the facet surfaces were already completely formed during the formation of the minor facets before the propagation of the crack outside the multiple facets. However, they were subsequently diminished by the compressive process under a negative stress ratio. This provides insights on the different formation processes of the major and minor facet.

In summary, multiple facets that approached 45° were observed at the fracture initiation site regardless of the stress ratios and fracture mode (i.e., surface fracture and internal fracture), and were classified into the major facet and the minor facet based on their surface appearances. The surface characteristics of the major and minor facet are shown in Table. 2-3. The major facet, which was observed in all specimens, had a relatively clear boundary and smooth surface. In contrast, the surface of the randomly distributed minor facet had striped tracks. The stress ratios had a significant effect on the striped tracks of the minor facets, but had no significant effect on the surface of the major facet, indicating that the smooth surface of the major facet was not formed by the compressive process but by its own initiation process. These fractography results indicate that the formation process of the major and minor facets was dissimilar. In other words, the fatigue process includes a two-step facet initiation and propagation processes as the schematic shown in Fig. 2-12. The crack initiation life stands for the

loading cycles before the first facet formation; the crack propagation life is subdivided into facet formation life and loading cycles consumed after facet formation, respectively. In the next section, the bonding pattern of the facets was discussed to describe the various facet formation processes.




(a) $\sigma_{max}$=800MPa, $R$=-0.5, $N_f$=4.7×10$^6$ (b) $\sigma_{max}$=625MPa, $R$=-1, $N_f$=2.0×10$^7$

Fig. 2-11. SEM images of multiple facets under negative stress ratios of FP material

Table. 2-3. Characteristics of the major and minor facet

| | Surface feature | Boundary | Distribution in every specimen |
|---|---|---|---|
| The major facet | Smooth | Clear | At least one |
| The minor facet | Striped Tracks, less pronounced in negative stress ratios. | Unclear | Random |

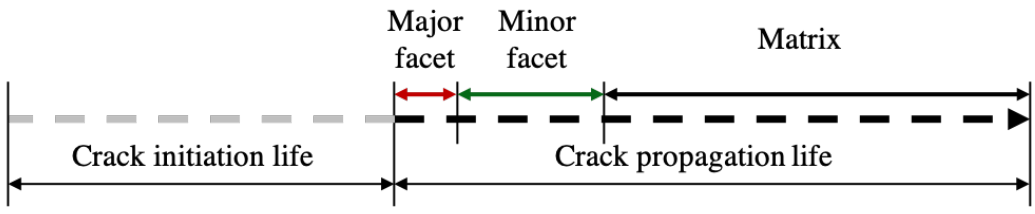


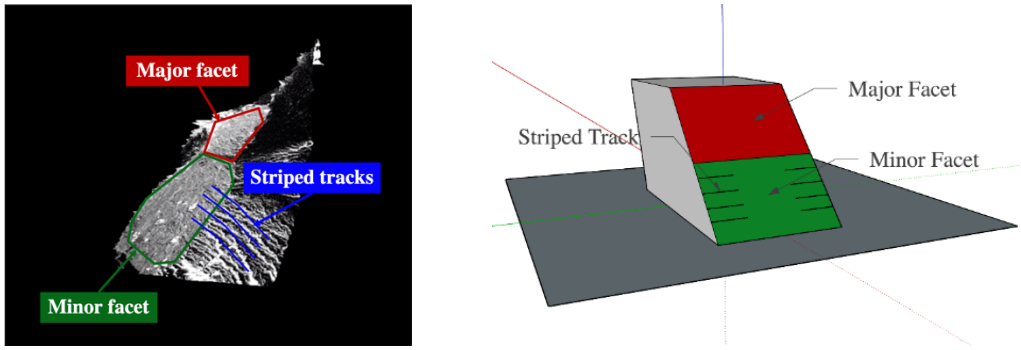

Fig. 2-12. Schematic of a fatigue crack growth process in beta titanium alloy

### 2.3.5 Facet bonding patterns

As mentioned above, although all facets were likely formed by slip deformation, the sequences of their formation should be considered different. Therefore, the author classified the relationship of normal vectors on various facets via 3D fractography in order to reveal the interaction between major and minor facets.

(1) Slope type

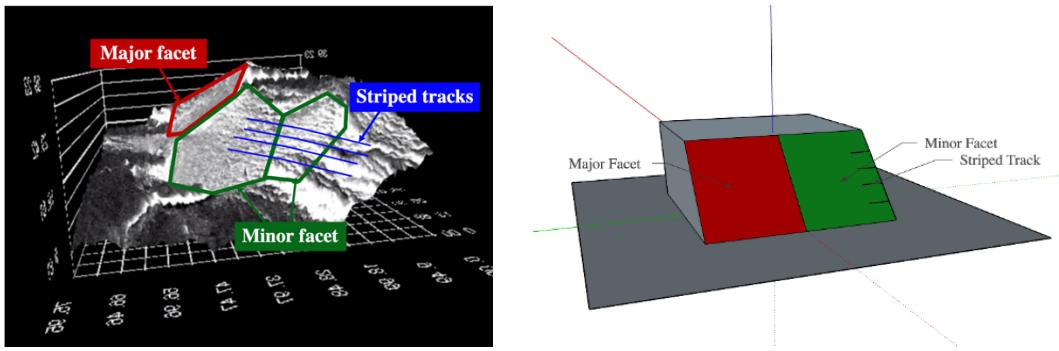
Some specimens showed a pattern wherein the normal vectors of the facets were parallel. This pattern can be defined as the “slope type.” Based on the altitude relations between the major and minor facet(s), the slope types can be further sub-classified into the vertical slope type (Fig. 2-13) and the horizontal slope type (Fig. 2-14). The slip system of the minor facet could easily be activated by the crack tip stress concentration after the major facet initiation, indicating that the slope type exhibited a two-step facet growth behavior.




(a) 3D-SEM image (b) 3D-model schematic image

Fig. 2-13. Schematic of the vertical slope type

$\sigma_{max}$=800MPa, $R$= −0.5, $N_f$=4.7×10$^6$




(a) 3D-SEM image (b) 3D-model schematic image

Fig. 2-14. Schematic of the horizontal slope type

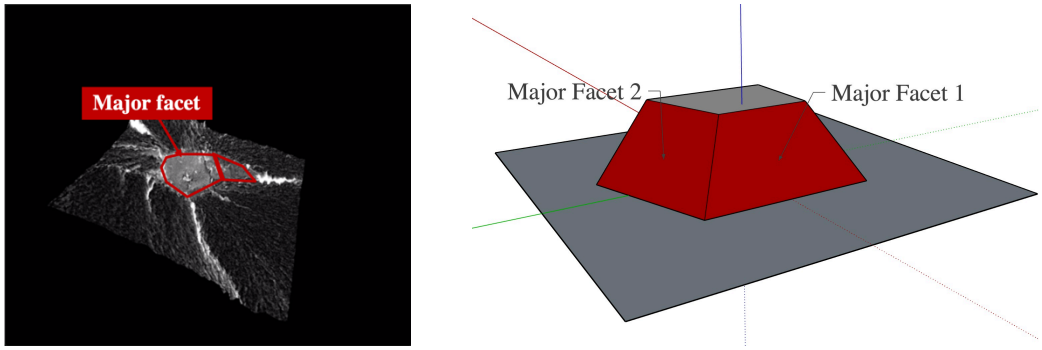
$\sigma_{max}$=975MPa, $R$=0.1, $N_f$=4.5×10$^6$

(2) Peak type

The specimens exhibited a pattern in which the normal vectors of the facets were pointing in different directions, as shown in Fig. 2-15. This pattern can be defined as the “peak type” and it indicates that it is difficult to activate one facet slip system using another one, and as thus, the two bonding facets were formed simultaneously. This consideration is consistent with the definition of major facets.

(3) Combination type

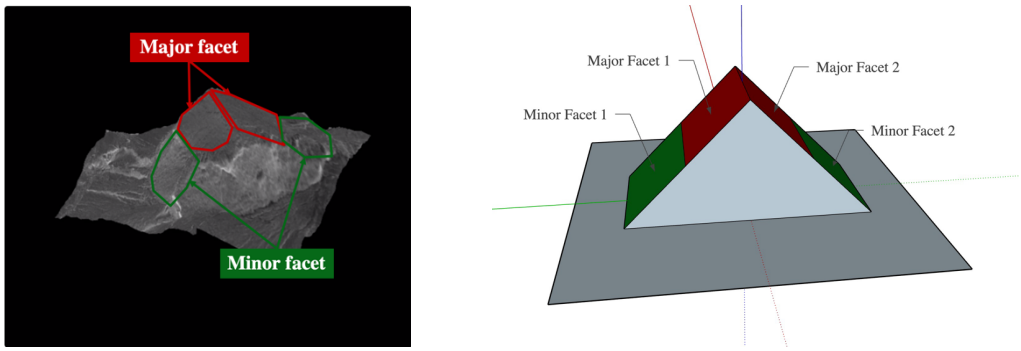
The combination of the two bonding types was also observed in some specimens and was defined as the “combination type” (Fig. 2-16). The top two facets were selected as the major facets due to the different orientations of normal vectors (i.e., peak type), and the pattern with the bottom minor facets connecting the major facets was considered as the slope type.




(a) 3D-SEM image (b) 3D-model schematic image

Fig. 2-15. Schematic of the peak type

$\sigma_{max}$=1000MPa, $R$=0.1, $N_f$=3.0×10$^5$




(a) 3D-SEM image (b) 3D-model schematic image

Fig. 2-16. Schematic of the combination type

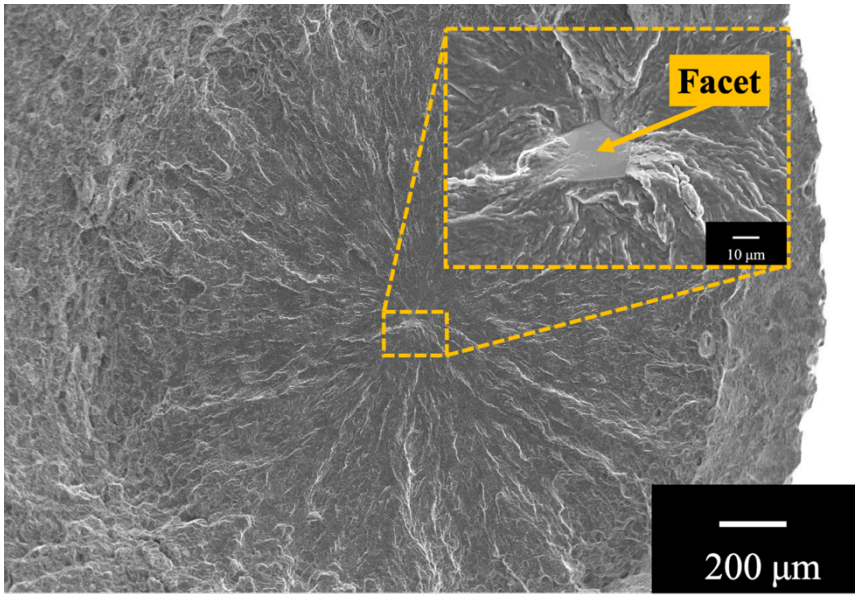
$\sigma_{max}$=625MPa, $R$=−1, $N_f$=2.0×10$^7$

## 2.4 Fractography results of material with coarse α-phase precipitation

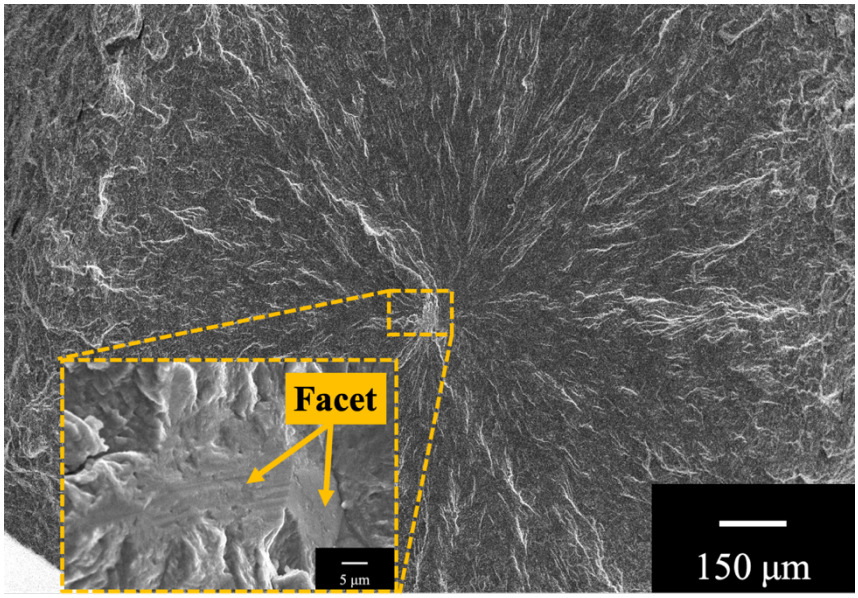
### 2.4.1 Fracture surface characteristics

Fig. 2-17 exhibits SEM images of the internal fractures in CP material. Similar to FP material, only one fracture initiation site with facet(s) is observed in each specimen. However, compared with the fracture surface of FP (Fig. 2-10), the radial pattern in CP material has less contrast compared with that in FP material. Additionally, the fracture surface of CP material also shows a smoother texture than FP material.

The different microstructures between FP and CP material are considered to account for these phenomena. The formation of the radial pattern is considered by the shear failure that occurred when the grains at the crack front are not perfectly coplanar. In other words, during the shear deformation process, the higher resistance it has from the microstructure, the more apparent radial patterns will appear. In FP material, grains are hardened by the fine alpha phase precipitation. However, grains in CP materials have the soft beta residual portion without alpha phase precipitation, thus provide less resistance against shear than the grains in FP material.




(a) CP, Internal, $\sigma_{max}$=900MPa, $R$=0.1, $N_f$=4.3×10$^5$



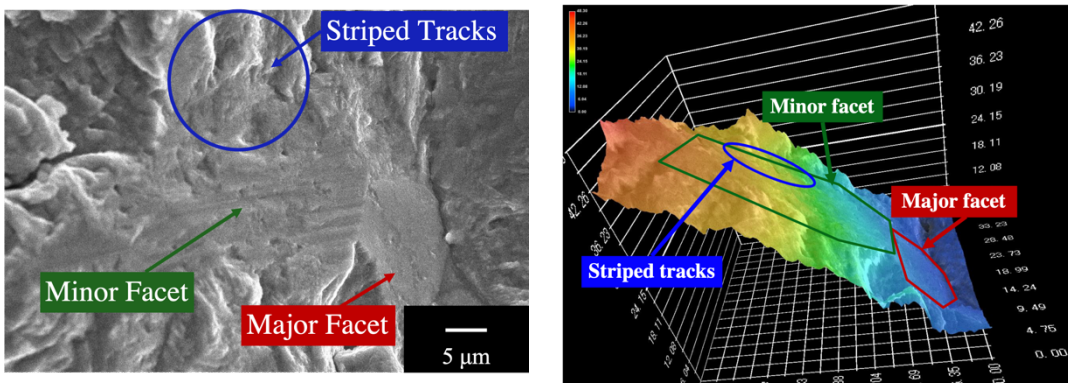

(b) CP, Internal, $\sigma_{max}$=875MPa, $R$=0.1, $N_f$=1.4×10$^6$

Fig. 2-17. SEM images of fracture surface of CP material

2.4.2 Facet surface features and bonding pattern

Fig. 2-18 shows the SEM images of facets under a positive stress ratio in CP material with the description of the major and minor facet(s). The facet surfaces in CP material have similar features to FP material, that is, clear grain-like boundary and smooth surface on the major facet, and unclear boundary with striped tracks on the minor facet. The distinct features between major and minor facet in CP material can reflect their different growth behaviors. However, the boundary of minor facet(s) in CP material is significantly more unclear compared with that in FP material, and striped tracks are rougher as well.

From the viewpoint of bonding patterns, the example shown in Fig. 2-18 is observed to have the feature of vertical slope type. Both facets approach 45 degrees to the fracture surface, which means the slip deformation may take charge of their formation. Above all, It can conclude that the facet surface features and multiple-facets bonding patterns established in Section 2.3.5 are the universal characteristics of internal fractures in beta titanium alloys.




(a) Facet surface feature (b) SEM 3D image (Slope)

Fig. 2-18. Multiple facets in CP material. $\sigma_{max}$=875MPa, $R$=0.1, $N_f$=1.4×10$^6$

## 2.5 Summary of Chapter 2

In this chapter, the fatigue properties of beta titanium alloys with two microstructures (i.e. FP and CP) were obtained by a hydraulic fatigue testing machine.

In FP material, the *S*-*N* curves under negative stress ratios represent a step-wise shape with a fatigue limit of surface fracture. However, in the case of a positive stress ratio, the fatigue limit of surface fracture becomes less remarkable and the *S*-*N* curve is close to an asymptote shape. The fatigue life for internal fracture can be seen at around $10^5$ cycles which is much earlier than the VHCF regime. The CP material has a similar trend of *S*-*N* curves with the FP material, but the earliest fatigue life for internal fracture occurred slightly later than FP material.

Then, from the fractographic analysis, multiple facets are observed at the crack initiation site surrounded by the smooth area. The major/minor facet(s) and facet bonding patterns have been confirmed regardless of microstructures, which suggests that they are universal characteristics of internal fractures in beta titanium alloys. Both major and minor facet(s) have 45 degrees to fracture surfaces, indicating they are presumably formed by slip deformation. The two-step facet initiation and propagation processes were proposed to describe the multiple facet growth behavior.

# Chapter 3

## Multiscale SR-CT technique and the imaging condition optimization for beta titanium alloy

# 3. Multiscale SR-CT technique and the imaging condition optimization for beta titanium alloy

To directly observe the inside of beta titanium alloy, the non-destructive inspection technique, multiscale SR-CT was applied in the present study. In this section, the SR-CT imaging system and the experimental details for optimizing the imaging conditions will be introduced. CP material with an remarkable difference between each phase was applied to evaluate the imaging quality by distinguishing those phases.

## 3.1 System overview of multiscale SR-CT system of BL20XU@SPring-8

The beamline BL20XU at SPring-8 includes two experimental hutches, which are separated by 160 m as shown in Fig. 3-1. The sample was set up in the first hutch. The imaging mode can be switched between micro-CT and nano-CT without moving the sample.

The micro-CT mode employs simple X-ray projection optics; the X-rays directly passed through the sample and were detected by an image detector located just behind the sample. By contrast, the nano-CT mode was based on full-field X-ray microscope optics consisting of a hollow-cone illuminating system using a condenser zone plate and pinhole, Fresnel zone plate objective, Zernike phase plate for high-sensitive phase contrast imaging, and an image detector located at the second hutch. Switching between the two measurement modes was made quick and easy by moving the apparatus in and out using a stepping motor drive. Additional details of the employed CT system can be found in the literature [56,61]. For both imaging modes, the sample

was rotated about the longitudinal axis from 0° to 180° with a step of 0.1° during the CT measurement, which provided 1800 radiographs per scan.

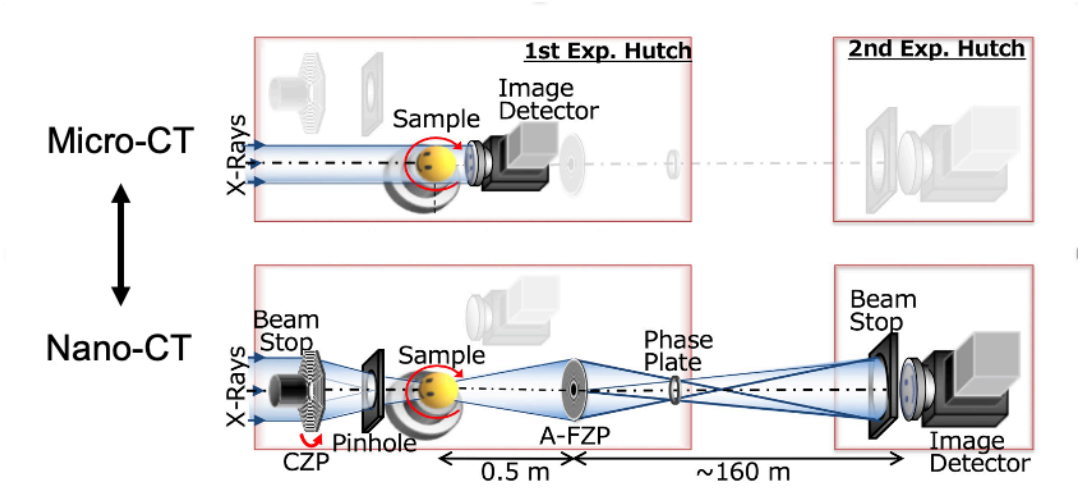



Fig. 3-1. Multiscale SR-CT system at beamline BL20XU @SPring-8, Japan[56]

## 3.2 Optimization of imaging condition

The objective of optimization was to improve the image quality with reasonable imaging conditions for micro-CT and nano-CT. In this section, the principle and details of determining critical factors for imaging quality will be introduced. Then, the CT images under various imaging conditions will be exhibited.

### 3.2.1 The principle of determining the imaging condition.

The imaging qualities are mainly determined by the X-ray energy, X-ray transmittance, and exposure time as the schematic shown in Fig. 3-2.

X-ray energy is determined by the imaging hardware system of the beamline. At BL20XU, micro-CT could be conducted at 30 keV and 37.7 keV. Nano-CT could be conducted at 20 keV and 30 keV (p.s., by 2023/7). In general, decreasing the X-ray energy is often considered a simple, helpful technique to improve the imaging quality from the viewpoint of increasing the X-ray absorption coefficient and its sensitivity between different phases in a material. However, X-ray energy can also affect the X-ray transmittance and the exposure time.

X-ray transmittance is a parameter describing how much X-ray can pass through an object to a detector, and is roughly determined by the X-ray energy, specimen diameter, and material chemical composition. Fig. 3-3 shows the relationship between X-ray transmittance and specimen diameter of the applied beta titanium alloy Ti-22V-4Al at various X-ray energy. The X-ray transmittance decreases with the increase in the specimen diameter. On the other hand, a too-thin specimen may cause extra difficulty in the fatigue test. Therefore, it is needed to find the appropriate specimen diameter which can fulfill the requirement for CT imaging as well as fatigue tests. From the guidance of researchers at SPring-8, micro-CT and nano-CT requires an X-ray transmittance of at least around 10% and 20%, respectively. According to Fig. 3-

3, the maximum feasible specimen diameters were ~1.6 mm for micro-CT under 37.7 keV, ~1.0 mm for micro-CT under 30.0 keV, ~0.7 mm for nano-CT under 30.0 keV and ~0.2 mm for nano-CT under 20.0 keV.

Exposure time, most commonly called “shutter speed,” is the length of time the detector collects X-ray for each radiograph. A higher X-ray energy may require a longer exposure time to enhance the X-ray absorption thus improving the imaging quality. However, since the operation time of the beamline is very limited (~30 hours per year), a long exposure time may also lead to an unreasonable long imaging duration (the length of time per CT scan in total).

Above all, the purpose of optimization of imaging condition is to investigate the balance between X-ray energy, X-ray transmittance, and exposure time, that is, the trade-off between imaging quality, fatigue test difficulty, and imaging duration.

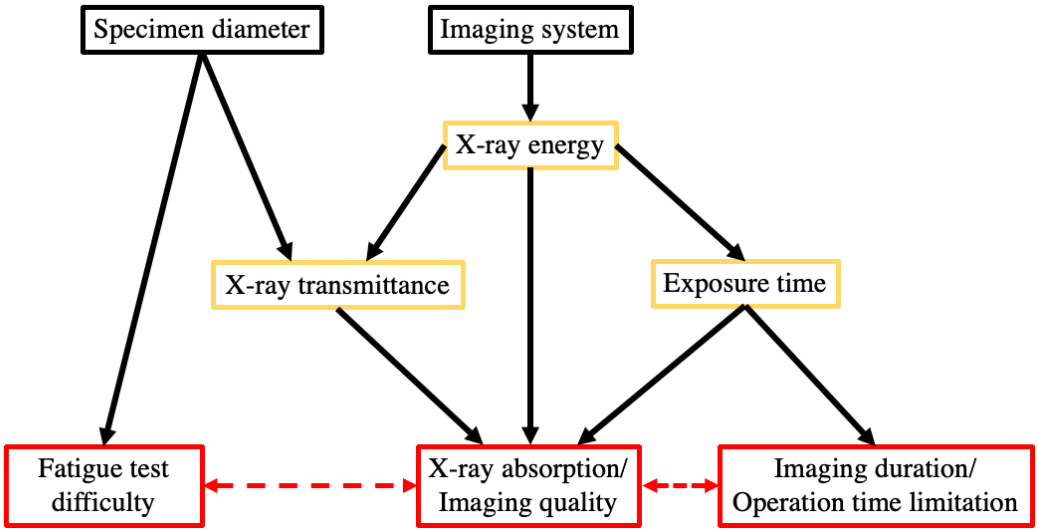



Fig. 3-2. Schematic of relationship between imaging conditions and their effect on experiment

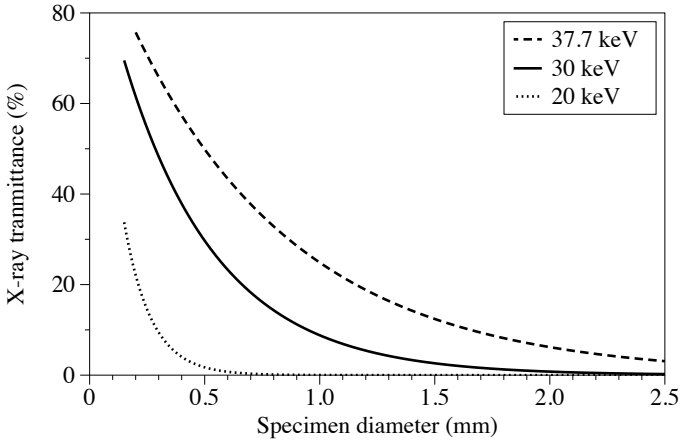



Fig. 3-3. Relationship between X-ray transmittance and specimen diameter of Ti-22V-4Al under 20keV, 30 keV and 37.7 keV

3.2.2 Experimental details for optimization

To study the image quality of various specimen diameters, a needle-shape configuration was designed as shown in Fig. 3-4. The specimen includes two portions: The portion with a ditch shape defect was made for micro-CT whose imaging quality will be evaluated by the clearness of the ditch boundary. On the other hand, the tip portion was designed for nano-CT. Meanwhile, since the nano-CT system can enhance the difference of each microstructural phase (i.e. alpha phase, alpha grain boundary, beta phase), the image quality of nano-CT was evaluated by visibility of each phase. Therefore, as mentioned in Section 2.1.1, CP material, which has a beta-phase residual in the center of the grain and an acicular alpha phase near the grain boundary, provided more distinct visibility of each phase and thus was chosen to make the needle-shape specimen. The microstructure of CP material is again exhibited in Fig. 3-5 which is the same as Fig. 2-1 (b).

The needle-shape specimen was set on the beamline and its images were taken by following the steps listed in Table. 3-1. For micro-CT (step 1), the author focused on the relationship between image quality with the specimen diameter. From the X-ray transmittance calculation in section 3.2.1, the maximum available specimen size for nano-CT is 0.7 mm. Therefore, to confirm the image quality at a specimen diameter compatible with both micro-CT and nano-CT, the minimum size tested in the micro-CT was set at 0.7 mm as well. Moreover, the maximum size of the micro-CT test was limited to 1.8 mm because the field of view of the micro-CT system was smaller than 2 mm and an appropriate margin was necessary. In addition, it is important to note that although micro-CT can be conducted under both 30.0 and 37.7 keV, the optimization for micro-CT in the present study was only conducted under 37.7 keV. This was because 37.7 keV was the maximum X-ray energy for micro-CT@BL20XU which

provided a larger available specimen diameter but a relatively worse imaging quality. In other words, at the same X-ray transmittance, the image quality of micro-CT under 30.0 keV should be reliable if those under 37.7 keV are acceptable.

In the case of nano-CT, the author focused on the effect of exposure time (step 2) and X-ray energy (step 3). In step 2, the effect of exposure time was investigated on the 0.7 mm diameter portion under 30 keV. The lower/upper limit of exposure time was determined by the acceptable imaging duration for each nano-CT imaging process. In step 3, low X-ray energy condition (20 keV) was tested on the 0.2 mm diameter portion which provided similar X-ray transmittance to step 2. Meanwhile, the low X-ray energy condition applied the lower limit of exposure time in step 2 to investigate the efficiency of increasing image quality by decreasing the X-ray energy.

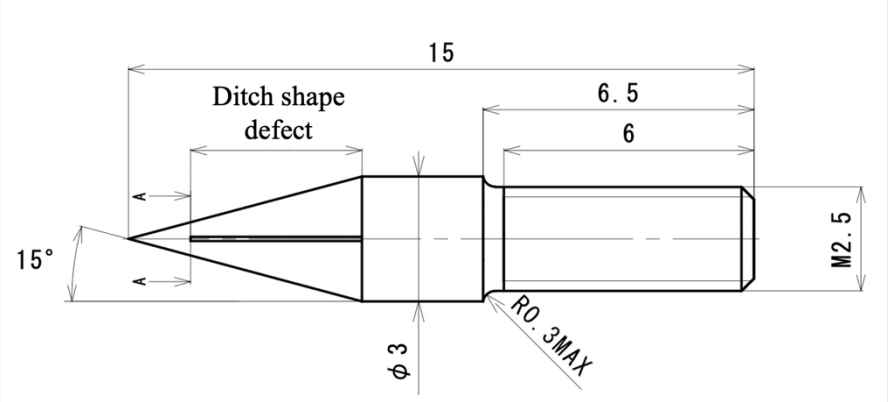



Fig. 3-4. Configuration of the needle-shape specimen for the optimization of imaging condition

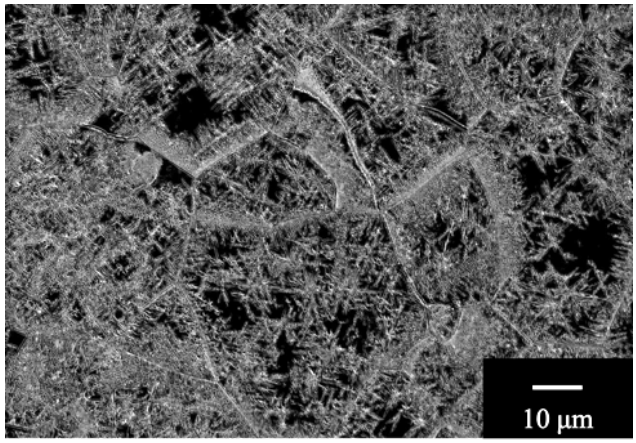



Fig. 3-5. SEM image of the microstructure of the heat-treated CP material with coarse, acicular alpha-phase precipitation (the same as Fig. 2-1 (b))

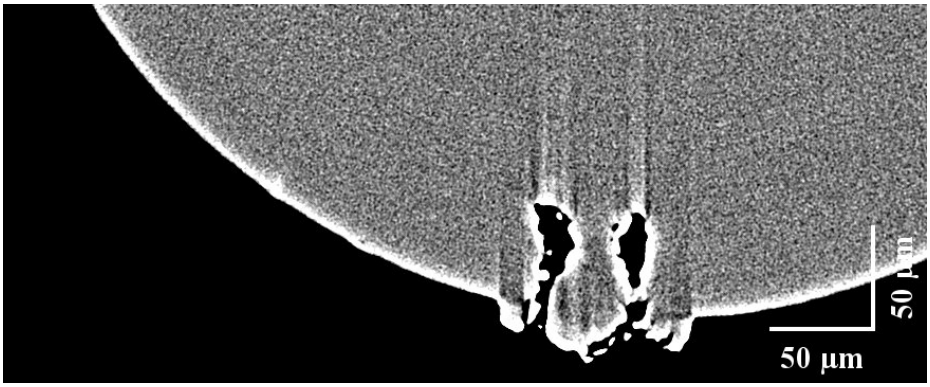
Table. 3-1. Imaging steps for optimizing the imaging conditions of Ti-22V-4Al

| Step | Imaging mode | X-ray energy | Specimen diameter | Exposure time |
|---|---|---|---|---|
| 1 | Micro-CT | 37.7 keV | 0.7 ~ 1.8 mm | 25 ms |
| 2 | Nano-CT | 30 keV | 0.7 mm | 1000 ~ 4000 ms |
| 3 | Nano-CT | 20 keV | 0.2 mm | 1000 ms |

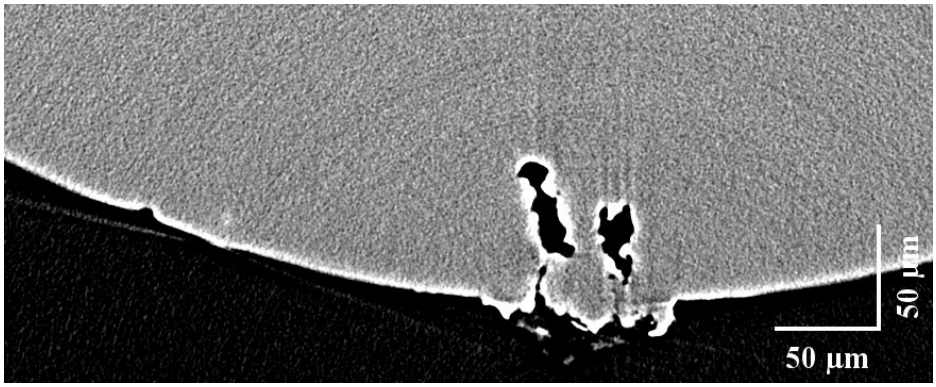
3.3 Micro-CT image under various imaging conditions.

The micro-CT images at various diameters of the needle-shape specimen under 37.7 keV are listed in Fig. 3-6. The exposure time was 25 ms determined by the empirical value. The gray portion represents the bulky specimen. Some defects from the ditch could be recognized at the bottom of the images. The imaging quality was evaluated by the clearness of the defect boundary. Note that the shape of the defect is different at each specimen diameter due to the manufacturing deviation/error.

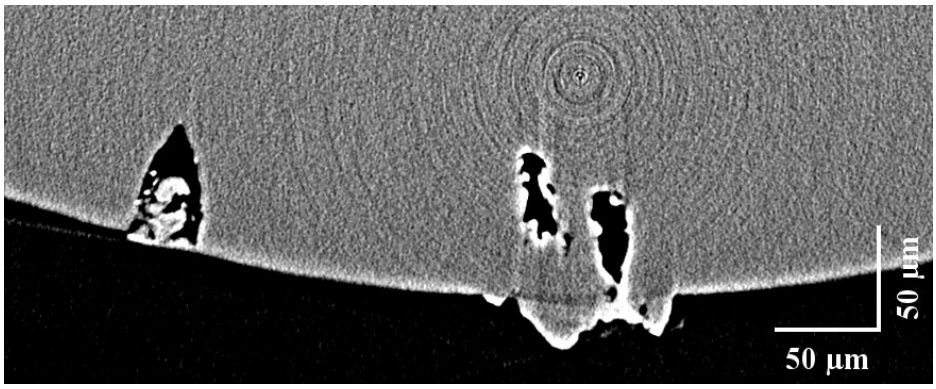
Generally, the defect boundaries of all the specimen diameters can be clearly recognized even for those under X-ray transmittance smaller than 10% (Fig. 3-6 (d), (e)). On the other hand, with the decrease of specimen diameter (i.e. the increase of X-ray transmittance), artifacts represented by the white edges at the specimen surface and streak pattern at the defect tip were observed as more remarkable, which indicates the excessive X-ray transmittance may also worsen the imaging quality.



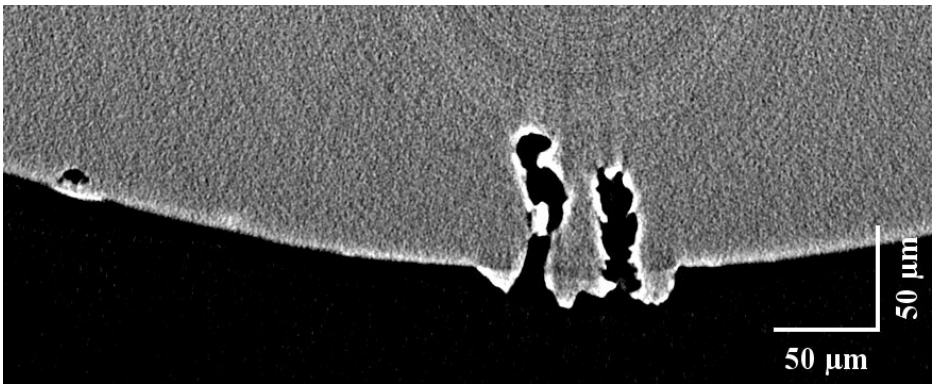

(a) φ0.6 mm, X-ray transmittance: ~43%



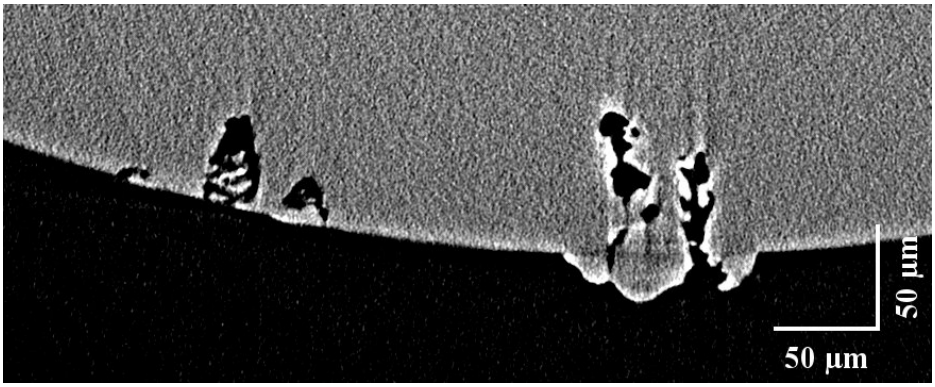

(b) φ1.2 mm, X-ray transmittance: ~19%




(c) φ1.6 mm, X-ray transmittance: ~11%




(d) φ1.7 mm, X-ray transmittance: ~9%



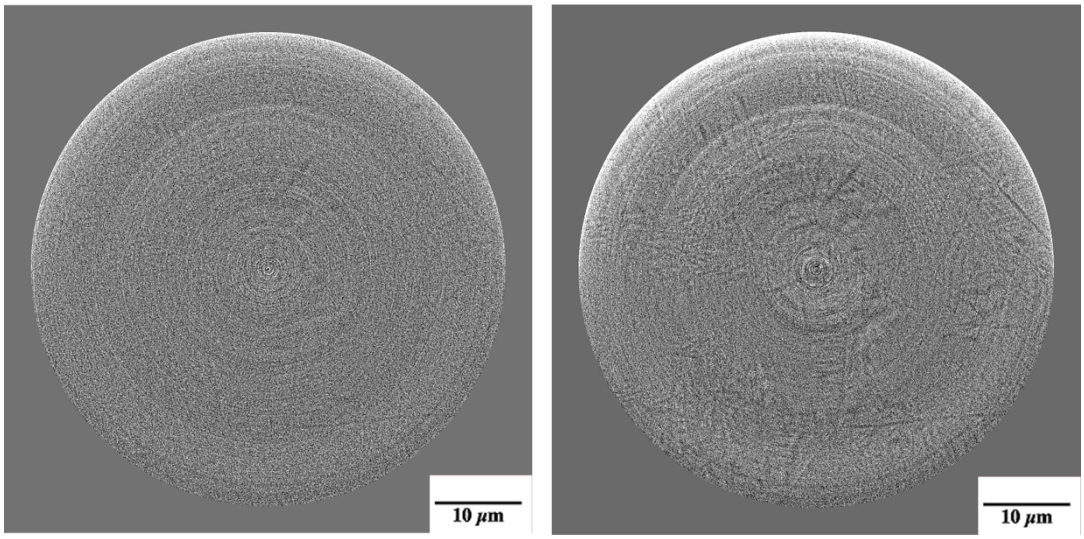

(e) φ1.8 mm, X-ray transmittance: ~8%

Fig. 3-6. Micro-CT images at various diameter of the needle-shape specimen under 37.7 keV (CP material;)

3.4 Nano-CT image under various imaging conditions.

The nano-CT images at 0.7 mm diameter under 30 keV are illustrated in Fig. 3-7, where Fig. 3-7 (a) and (b) represent the images using exposure times of 1000 ms and 4000 ms, respectively. The corresponding X-ray transmittance was approximately 18%. The grain boundary was barely observed at an exposure time of 1000 ms. In contrast, the grain boundary and acicular alpha-phase precipitation are discernible at 4000 ms of exposure.

The nano-CT images at 0.2 mm diameter under 20 keV are presented in Fig. 3-8 with a similar X-ray transmittance to those in Fig. 3-7. The exposure time was 1000 ms which was the same as that in Fig. 3-7 (a). The microstructural details, such as grain boundary, acicular alpha-phase precipitation, and residual beta-phase, are more clearly observed in Fig. 3-8 than in Fig. 3-7 (a) and Fig. 3-7 (b), indicating that the decrease in X-ray energy significantly improves the quality of microstructural visualization.




(a) Exposure time: 1000 ms (b) Exposure time: 4000 ms

Fig. 3-7. Nano-CT-imaging conditions in terms of the exposure time (CP material; specimen diameter: 0.7 mm; X-ray energy: 30 keV; transmittance: ~18%)

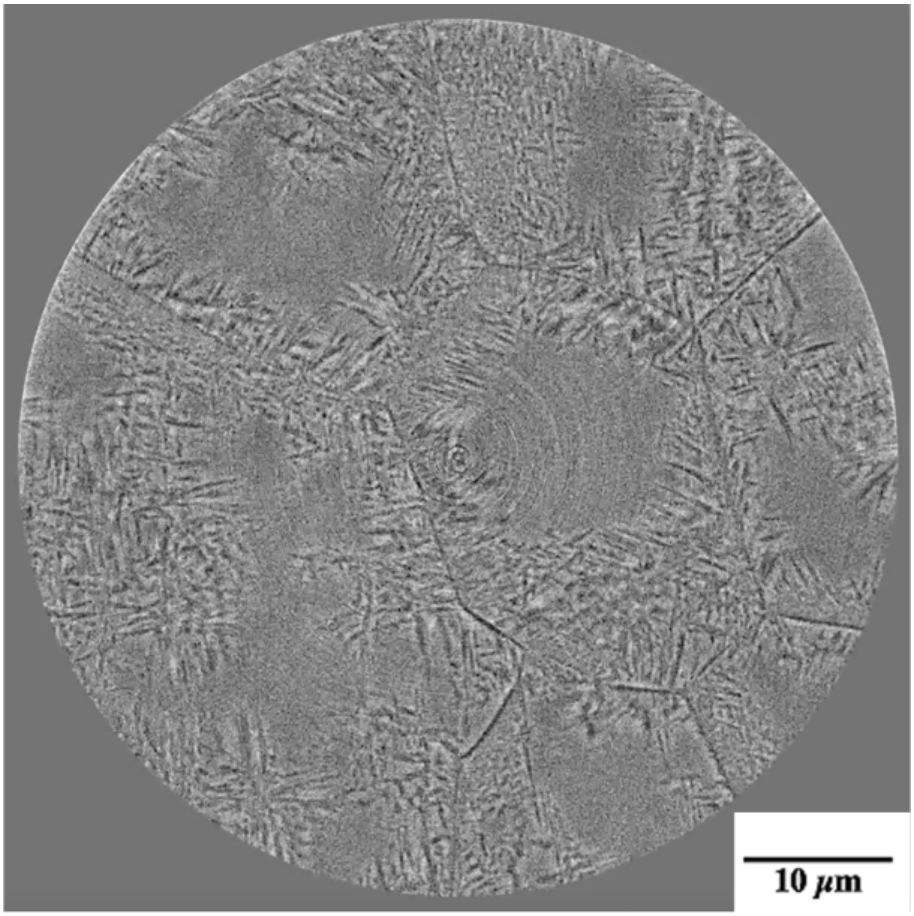



Fig. 3-8. Nano-CT-imaging conditions in terms of the X-ray energy (CP material; specimen diameter: 0.2 mm; X-ray energy: 20 keV; transmittance: ~21%, exposure time: 1000 ms)

## 3.5 Summary of Chapter 3

In this chapter, the multiscale SR-CT system, including micro-CT and nano-CT, @BL20XU, SPring-8 was introduced. Meanwhile, the principle of determining imaging conditions and the restraint between each condition was explained. In addition, the experimental conditions the author focused on for micro-CT and nano-CT were introduced respectively. As a result, the micro-CT images exhibited satisfying quality from 0.7 mm to 1.8 mm under 37.7 keV and had no apparent difference. In the case of nano-CT, under the same X-ray energy of 30 keV, longer exposure time provided more details of each phase. However, with consistent X-ray transmittance using a thinner specimen, reducing the X-ray energy can significantly improve the image quality even applying a short exposure time.

# Chapter 4

## *In situ* small crack growth test by multiscale SR-CT

# 4. *In situ* small crack growth test by multiscale SR-CT

After achieved in obtaining the internal information of beta titanium alloy with microstructure visualization, the author made an attempt to continuously observe the crack growth process by multiscale SR-CT. To avoid moving the specimen between the fatigue test and CT imaging, a piezo fatigue testing machine for the *in situ* observation was developed which means the fatigue test can be conducted on the beamline. This section will introduce the details of the piezo fatigue testing machine and the small surface crack behaviors observed by multiple SR-CT. Similar to chapter 3, to evaluate the imaging quality of multiscale SR-CT, fatigue test in this chapter was conducted on CP material which has remarkable phase difference.

## 4.1 Methodology

### 4.1.1 Specimen configuration and material

As mentioned in Chapter 3, to obtain adequate X-ray transmittance, the specimen diameter should be sufficiently small. Although the imaging optimization of nano-CT showed that a 0.2 mm specimen under 20 keV represented the best quality of microstructure visualization; however, conducting fatigue tests with a specimen of 0.2 mm diameter is challenging and may not attract industrial attention. Therefore, the author adopted the second-best condition using a specimen of 0.7 mm diameter. In this study, the control volume of the specimen was first lathe-turned to a diameter of 0.8 mm with a length of 3 mm, as shown in Fig. 4-1. To remove the hardened layer due to the lathe-turning process, the control volume was sequentially polished using #800–#2000 emery papers to achieve a diameter of 0.7 mm. The material adopted for the small surface crack growth test was the CP material which has a beta-phase residual in the center of the grain and an acicular alpha phase near the grain boundary. Its

microstructure and mechanical properties are again presented in Fig. 4-2 (same as Fig. 2-1 (b)) and Table 4-1 (included in Table. 2-2), respectively.

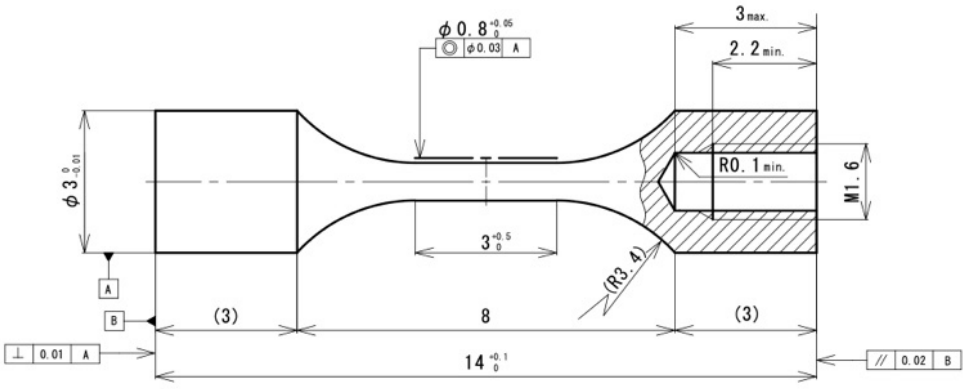



Fig. 4-1. Configuration of the specimen (units: mm)

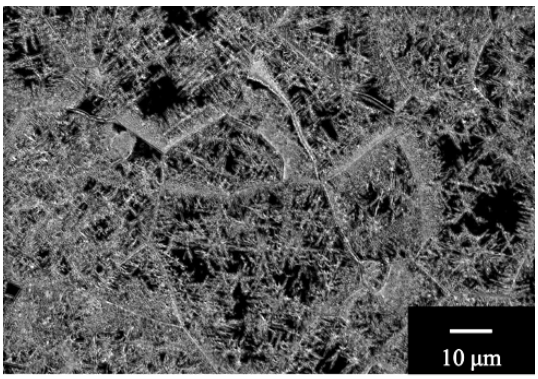



Fig. 4-2. SEM image of the microstructure of the heat-treated CP material with coarse, acicular alpha-phase precipitation (the same as Fig. 2-1 (b))

Table 4-1. Mechanical properties of the applied CP material.

| 0.2% Proof Stress [MPa] | Tensile Strength [MPa] | Elongation [%] | Reduction of Area [%] |
|---|---|---|---|
| 850 | 967 | 21.9 | 58.2 |

4.1.2 Instrumentation of fatigue testing setup

An *in situ* piezo fatigue-testing machine was developed to perform fatigue tests on the beamline, as illustrated in Fig. 4-3. The hardware of the machine was mainly developed by Yuma Kon in his Master's course from 2019. The author was taking charge of the design of the specimen gripping mechanical system and the calibration of the testing system including tuning up of the control parameters optimized for accurate fatigue tests. The employed piezo actuator was PSt 150/10/200 VS15 (Piezomechanik Co., Ltd). The working range of the voltage was from −30 V to 150 V, providing a maximum stroke of 270 μm. The capacities of the tensile and compressive loads were 600 N and 3800 N, respectively. During the imaging process, the entire system was set on a rotation stage. According to Fig. 4-3, X-rays originate from the left direction, pass through the PMMA (polymethyl methacrylate) cylinder and the specimen, and finally enter the image detector. In addition, to avoid overheating of the piezo actuator, an air coolant was introduced through the air inlet. A digital servo controller (Shimadzu 4830) was applied to generate a waveform and to control the fatigue test.

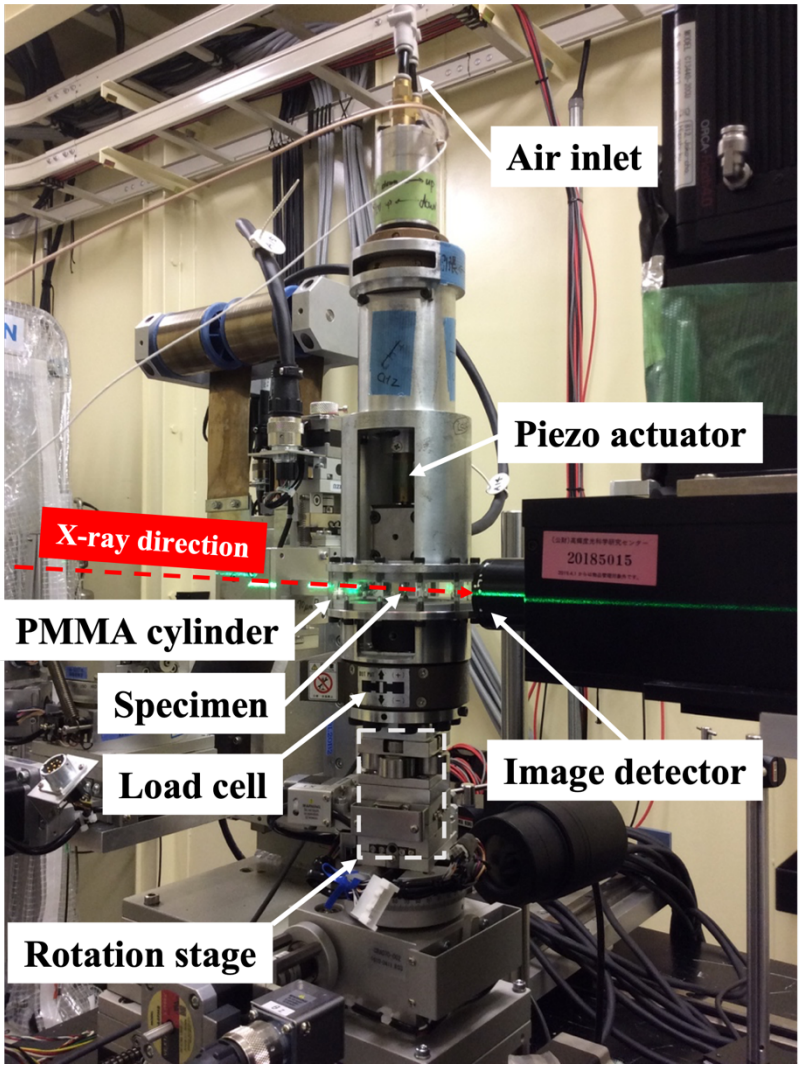



Fig. 4-3. *In situ* piezo fatigue-testing setup

4.1.3 Testing procedure

The fatigue properties of the experimental material are demonstrated in Fig. 4-4 (included in Fig. 2-6). Owing to the limit of the beamline operation time, the test condition was determined as the maximum stress of 650 MPa, which was 76% of the proof stress under a stress ratio $R = -1$ to reach a relatively short fatigue life. The corresponding fatigue life was approximately $10^4$ cycles. For the *in situ* small-crack growth test, the experimental steps were as follows. First, a micro-CT image was captured prior to the fatigue test. The fatigue test and CT imaging were then repeated. The intervals of the loading cycles ($\Delta N$) and CT mode were determined for each purpose. To capture the small-crack initiation, micro-CT was conducted with a $\Delta N$ of 500 cycles until 2000 cycles. Micro-CT images were obtained at 0, 500, 1000, 1500, and 2000 loading cycles. Subsequently, nano-CT was performed on the initiated crack for additional local microstructural details. After 2000 cycles, CT imaging was conducted with a $\Delta N$ of 1000 cycles to clearly observe the crack-propagation behavior until the specimen was fractured. The CT imaging conditions are listed in Table 4-2. The testing frequency was set at 10 Hz. To open the crack, a tensile load equivalent to 50% of the maximum stress was applied to the specimen during CT imaging.

The obtained CT images were analyzed using ImageJ software [63]. A schematic of a crack with relevant parameters is shown in Fig. 4-5. The horizontal crack length at the specimen surface, $2a$ (hereinafter called “crack length”), and crack depth, $b$, were specifically focused in this study.

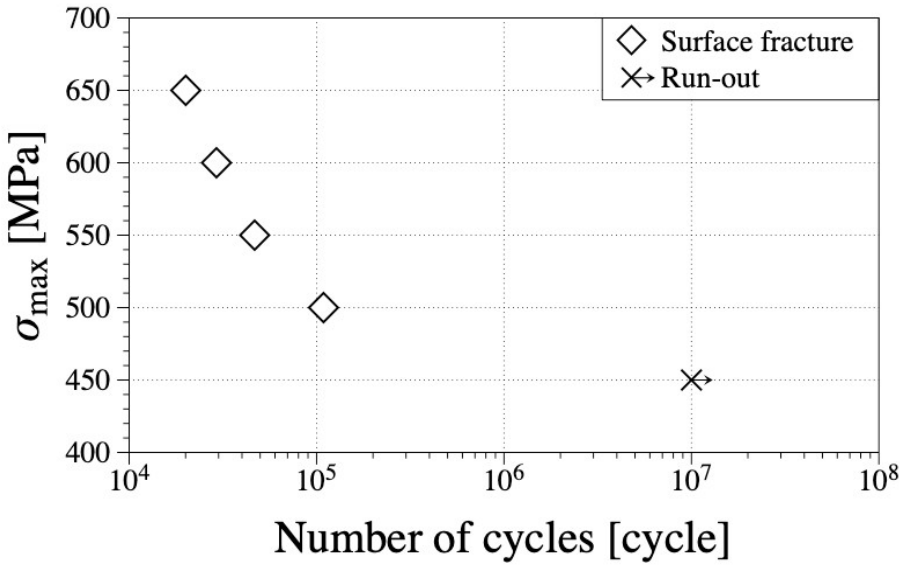



Fig. 4-4. Fatigue properties of the CP material under a stress ratio, $R = -1$

Table 4-2. Imaging conditions of micro-CT and nano-CT.

| Imaging mode | Micro-CT | Nano-CT |
|---|---|---|
| X-ray energy (keV) | 30 | |
| Binning mode | 1 × 1 | |
| Exposure time (ms) | 25 | 4000 |
| Voxel size (μm) | 0.5 | 0.0387 |
| Sample–detector distance (m) | 0.06 | ~160 |
| Field of view (mm × mm) | 1 × 1 | 0.063 × 0.063 |
| Total scan duration (min) | ~10 | ~120 |

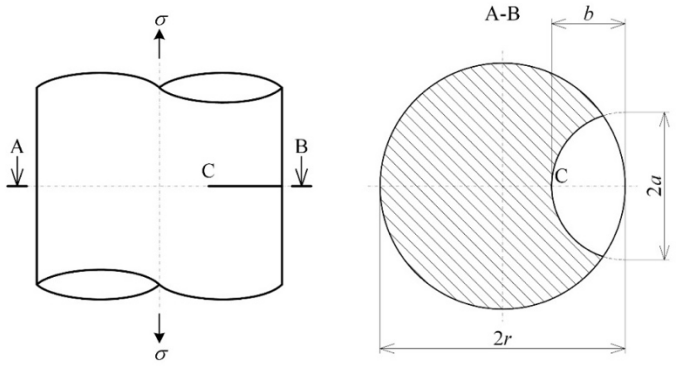
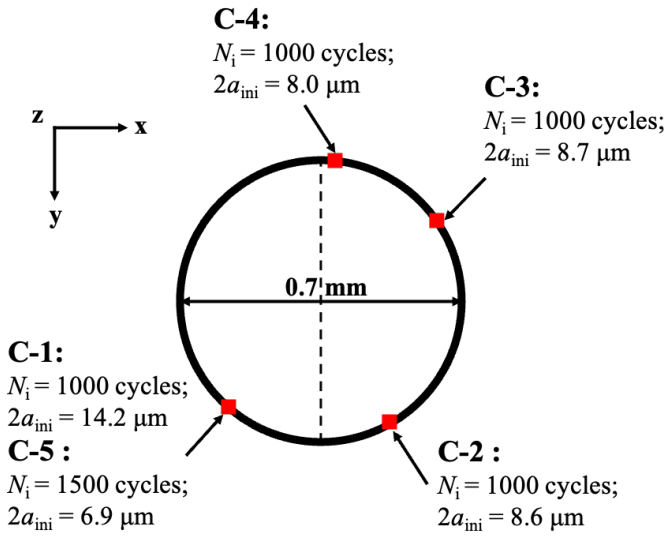



Fig. 4-5. Schematic of the crack and relevant parameters

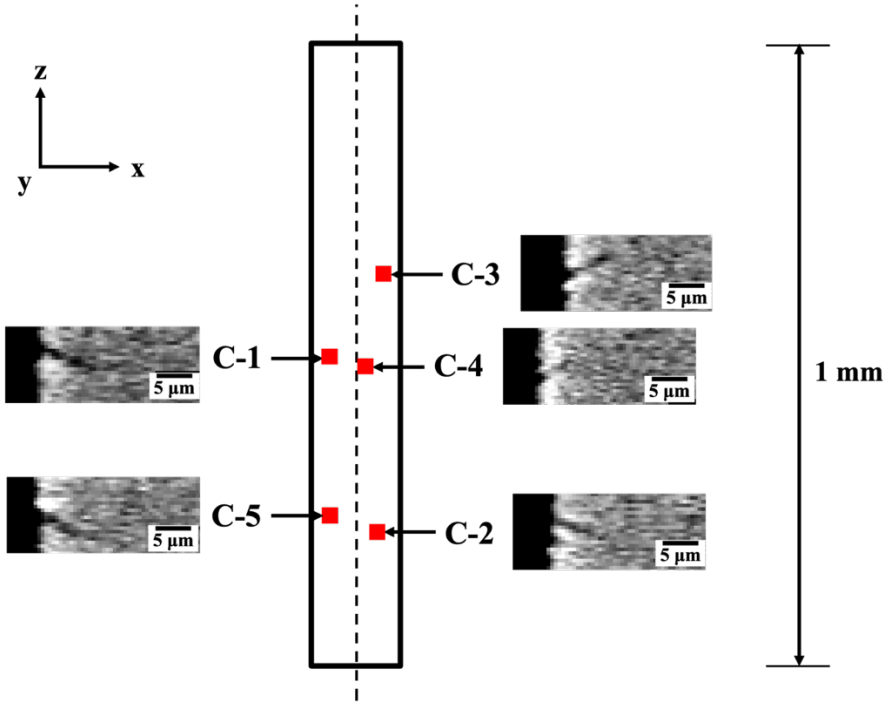
## 4.2 Crack initiation status

During the tests, multiple small cracks were initiated at the specimen surface. The crack initiation location on a plane perpendicular to the loading axis, as well as the crack-initiation life ($N_i$) and crack-initiation length ($2a_{ini}$), are illustrated in Fig. 4-6 (a). The side view of the specimen as well as the images of the cracks initiated on the virtual cross section parallel to the longitudinal direction are demonstrated in Fig. 4-6 (b). In this study, $N_i$ and $2a_{ini}$ of each crack were defined as the number of cycles and the crack length upon crack detection, respectively.

As described in Section 4.1.3, micro-CT imaging was conducted at 0, 500, 1000, 1500, and 2000 cycles to detect the initiated cracks. The first four cracks are detected at 1000 cycles, which is approximately 10% of the average fatigue life. These four cracks, labeled counterclockwise from C-1 to C-4, were randomly distributed on the specimen surface. In addition, another crack, C-5, which was initiated at 1500 cycles, was detected at the same location as that of C-1 in the XY plane but on a different Z axis. The average $2a_{ini}$ of the five cracks was 9.3 μm, which was much smaller than the average grain size (20 μm), implying that crack initiation was successfully captured. In the present study, these five cracks were chosen for further investigation of crack growth behaviors.




(a) Crack-initiation location on the plane perpendicular to the loading axis, with the corresponding initiation life and crack length values

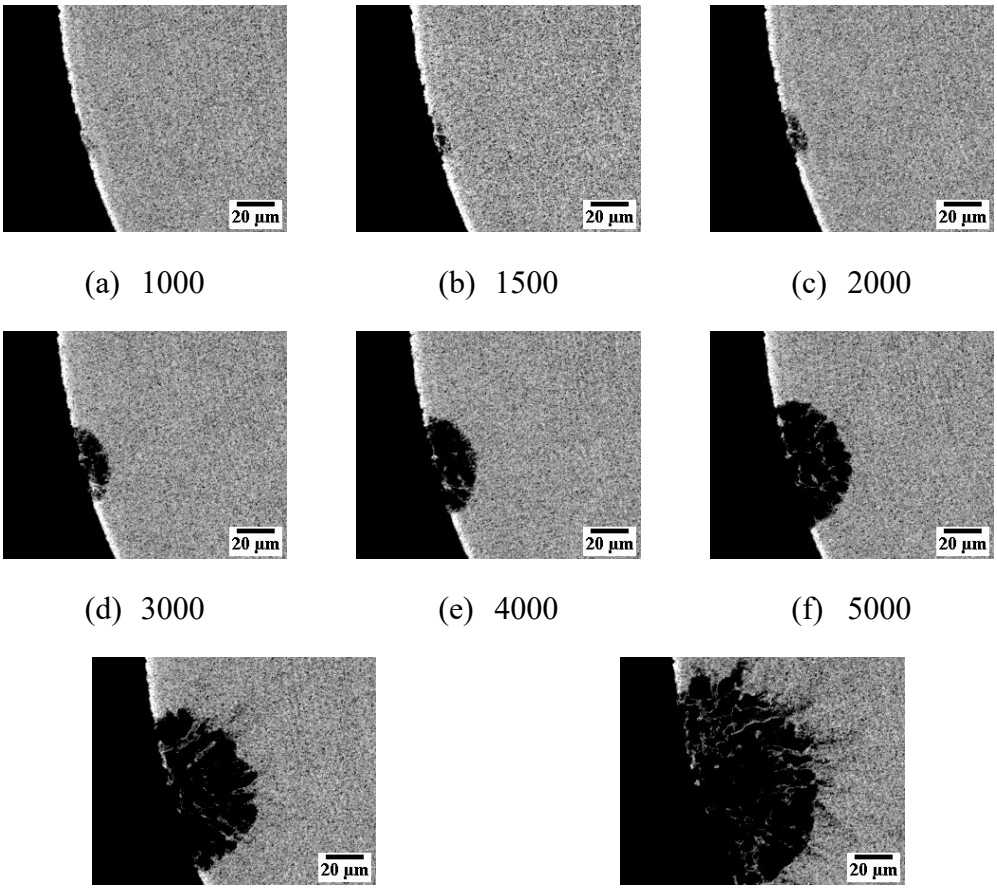



(b) Crack-initiation location on the side-view of the specimen and the images of the cracks initiated on the virtual cross section parallel to the longitudinal direction

Fig. 4-6. Crack-initiation status (CP material)

4.3 Crack propagation process

As an example, the propagation process of C-1 until 7000 cycles is depicted in Fig. 4-7, which shows the micro-CT images projected on a plane perpendicular to the loading axis. The crack depths and lengths ($b$ and $2a$, respectively) were measured from these images. In the CT images, the low-density materials or the defects and voids appear darker than their surroundings. Therefore, the shadow features in Fig. 4-7 indicate an open crack. After the crack is initiated, it propagates symmetrically from the center. The relationship between the crack length, $2a$, and the number of cycles, $N$, for all five cracks, is demonstrated in Fig. 4-8. The fatigue life of this specimen was 9751 cycles, and C-1 was the main crack that led to the final fracture.




(a) 1000 (b) 1500 (c) 2000

(d) 3000 (e) 4000 (f) 5000

(g) 6000 (h) 7000

Fig. 4-7. Propagation process of crack C-1: Micro-CT images projected on a plane perpendicular to the loading axis (CP material)

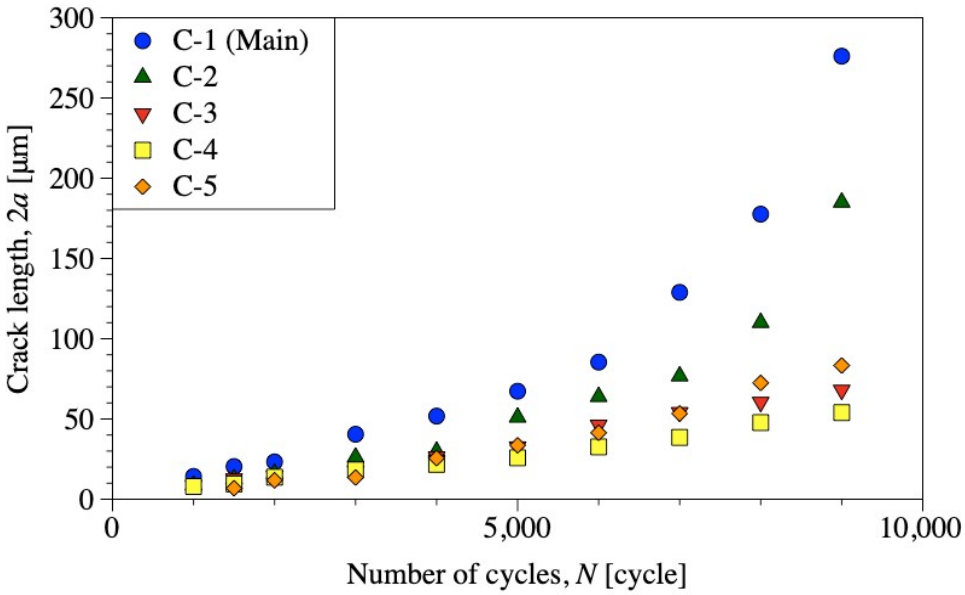



Fig. 4-8. Relationship between the crack length and number of cycles (CP material)

4.3.1 Crack-shape evolution and the corresponding stress intensity factor

According to Fig. 4-7, crack C-1 exhibits a semi-elliptic shape before 4000 cycles (Fig. 4-7 (a)–(e)), and changes into a semicircular shape after 5000 cycles (Fig. 4-7 (f)–(h)). To describe the crack shape, the aspect ratio of the crack ($b/a$) was plotted with respect to the crack length, as shown in Fig. 4-9. In general, the deviation in $b/a$ of all five cracks is relatively large in the small crack-length region. However, when the crack length increases, the deviation in $b/a$ becomes less pronounced, and the value of $b/a$ approaches 1. This indicates that microstructural factors affect the propagation of a small crack, which leads to a less stable crack shape than a large crack.

For comparison with the large cracks, the author adopted the stress intensity factor range, $\Delta K$, for the small cracks. To calculate $\Delta K$ corresponding to the current crack shape, the author have used the method proposed by Nisitani et al. [69], as shown in Eq. (4-1):

$$\Delta K = F_1 \Delta\sigma\sqrt{\pi b}, \tag{4-1}$$

where $\Delta K$ is the stress intensity factor range at the crack front; $F_1$ represents a factor related to the aspect ratio in terms of the crack geometry, $b/a$, and the ratio of the crack depth to the specimen radius, $b/r$. Some $F_1$ values are listed in Table 4-3. The calculated values were linearly interpolated according to the crack length and shape. $\Delta\sigma$ indicates the range of applied positive stress.

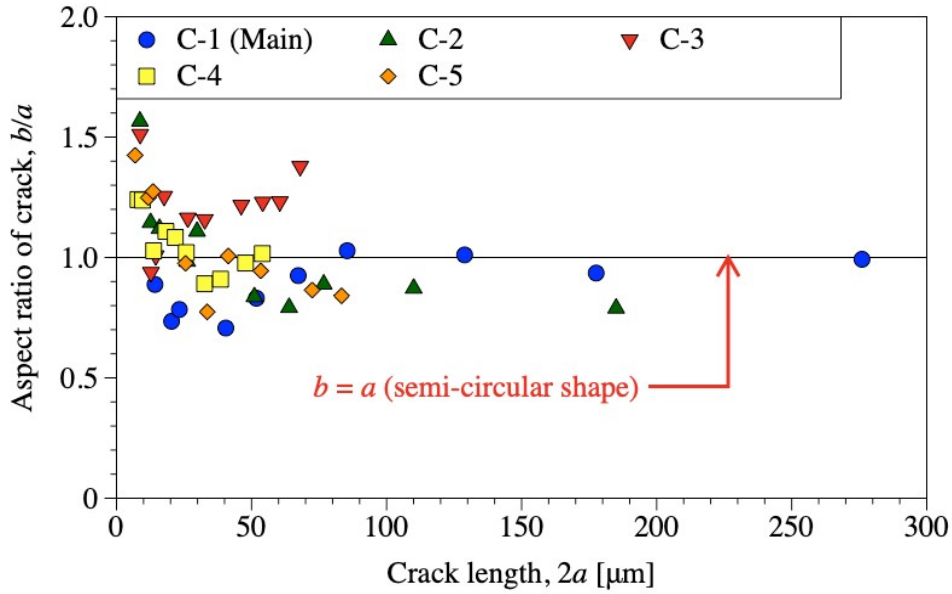



Fig. 4-9. Relationship between the aspect ratio of the crack, $b/a$, and crack length, $2a$ (CP material)

Table 4-3. $F_1$ values in terms of the crack geometry, $b/a$, and the ratio of the crack depth to the specimen radius, $b/r$

| $b/a$ \ $b/r$ | 0 | 0.125 | 0.250 | 0.375 | 0.5 |
|---|---|---|---|---|---|
| 1 | 0.66 | 0.665 | 0.683 | 0.714 | 0.758 |
| 0.5 | 0.884 | 0.890 | 0.980 | 0.976 | 1.064 |

4.3.2 Crack propagation rate

A comparison between the d$a$/d$N$ values of all five cracks against $\Delta K$ is presented in Fig. 4-10. The crack lengths and shapes of these five cracks are dissimilar, as shown in Fig. 4-8 and Fig. 4-9; however, their d$a$/d$N$-$\Delta K$ curves exhibit a good agreement, signifying that the shape evolution of naturally initiated cracks does not critically affect the d$a$/d$N$–$\Delta K$ curves. In addition, with a decrease in $\Delta K$, the deviation in d$a$/d$N$ increases. Tokaji et al. also conducted a $\Delta K$-decreasing test using a compact tension specimen of Ti–22V–4Al, represented by the dashed line in Fig. 4-10 [33].In the high-$\Delta K$ regime (over 4–5 MPa√m), the d$a$/d$N$–$\Delta K$ in the present study was consistent with that of large cracks. In contrast, in the low-$\Delta K$ regime, most of d$a$/d$N$ of small cracks were faster than that of large cracks at the same $\Delta K$. The above results can be explained by the fact that a smaller crack follows a path with less resistance, and its growth can be hindered by the local microstructural factors.

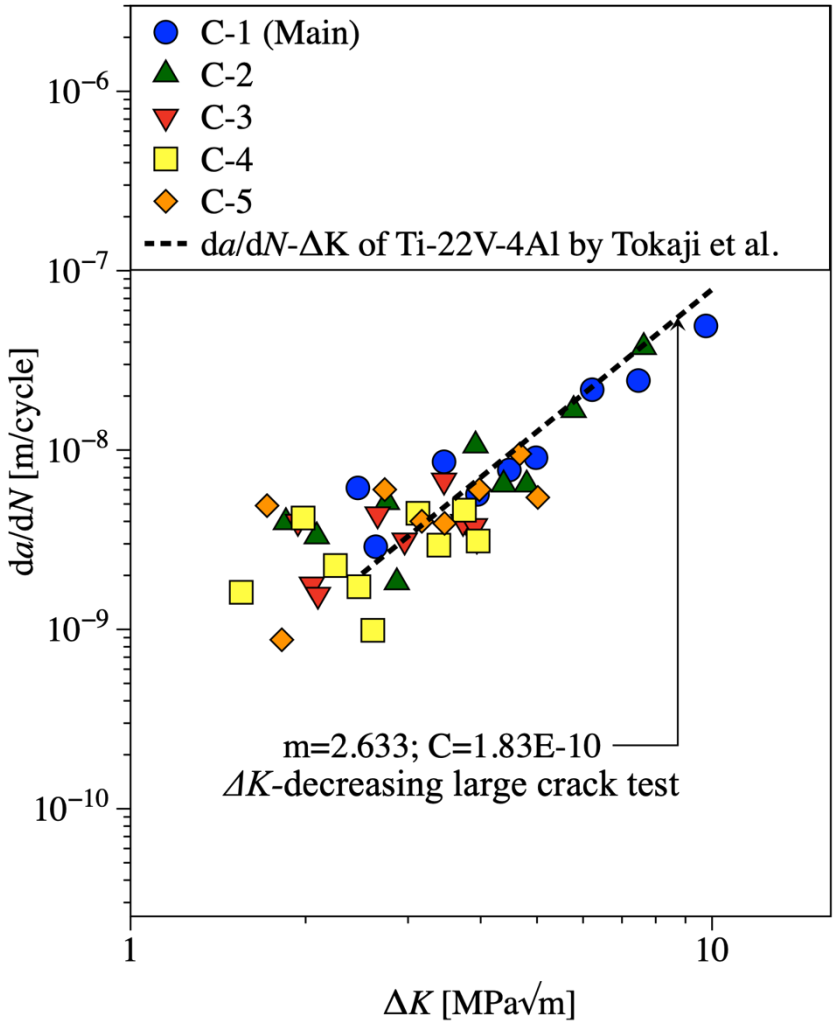



Fig. 4-10. Relationship between the crack propagation rate and the stress intensity factor range (CP material)

## 4.4 Crack initiation process

### 4.4.1 Crack initiation rate

The five cracks initiated naturally but at different cycles. Yoshinaka et al. defined the crack initiation rate, ($\left.\frac{\mathrm{d}a}{\mathrm{d}N}\right|_{\mathrm{i}}$), as shown in Eq. (4-2), which is comparable to the crack propagation rate but describes the speed of crack initiation [70].

$$\left.\frac{\mathrm{d}a}{\mathrm{d}N}\right|_{i} = \frac{a_{\mathrm{ini}}}{N_{\mathrm{i}} - N_{\mathrm{i}-1}} \tag{4-2}$$

Here, $a_{\mathrm{ini}}$ is half of the initial crack length, $N_{\mathrm{i}}$ is the number of cycles corresponding to the detection of the first crack (crack initiation life), and $N_{\mathrm{i-1}}$ is the number of cycles one step before $N_{\mathrm{i}}$ during the CT scanning. Because of the consistent scanning intervals at the early stage of the experiment, $N_{\mathrm{i}} - N_{\mathrm{i-1}}$ was 500 for all five cracks, thus eliminating the influence of dissimilar crack initiation lives. The initiation rate of all five cracks against $\Delta K$ are illustrated in Fig. 4-11, along with the integration of the crack propagation rate shown in Fig. 4-10 for comparison. The crack initiation rate was plotted at approximately $10^{-8}$ m/cycles, which is 5 to 10 times larger than the crack propagation rate in the early stage. Meanwhile, the crack initiation rate has a more concentrated distribution than the crack propagation rate. Therefore, the crack initiation process has a consistent mechanism regardless of the number of cracks and occurs faster than the subsequent propagation process. Other studies on the crack-initiation process also infer similar results. Yoshinaka et al. reported that the internal crack initiation rate in Ti–6Al–4V is similar among various cracks and faster than the subsequent propagation rate [70]. Meanwhile, in an alpha titanium alloy, Pilchak et al.

discovered that the crack initiated on the alpha grain facet in the faceted growth mode is one or two orders of magnitude faster than that in the striated growth mode [71].

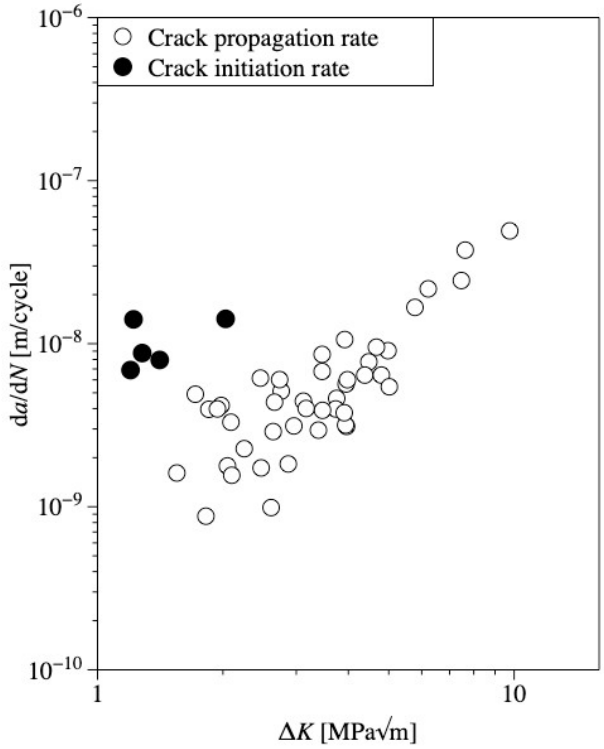



Fig. 4-11. Relationship between the crack initiation rate and the stress intensity factor range (CP material)

4.4.2 Crack initiation site in the microstructure

The crack initiation site in the microstructure of beta titanium alloys is much debated. Tokaji et al. mentioned that the crack presumably initiates from the alpha phase or the grain boundary in Ti–22V–4Al [10]. Uematsu et al. pointed out that cracks initiate in the beta grain with rich alpha-phase precipitation in Ti–22V–4Al [32]. Shiozawa et al. reported that the crack originates inside a beta grain in Ti–15V–3Cr–3Sn–3Al (Ti-15-3-3-3) [11]. Therefore, the author focused on revealing the mutual relationship between the crack initiation site and microstructure using nano-CT.

The 3D morphology of crack C-1 at 1500 cycles is shown in Fig. 4-12, and the sliced images are presented in Fig. 4-13. The grain boundary and acicular alpha phase are discernible from Fig. 4-13 (a) and (b), which are the nano-CT images resliced in the directions of crack length and depth, respectively. First, the crack does not cross the grain boundary in either image, which indicates that the crack initiates inside the beta grain rather than the grain boundary. In addition, the crack is located at the center of the grain. As mentioned in Section 4.3, the crack propagates symmetrically, which implies that the crack presumably initiates from the center and not near any side of the grain boundary. Although it is difficult to recognize the acicular alpha-phase precipitation near the crack, the comparison of the microstructure and nano-CT images in Fig. 4-2 and Fig. 3-8, respectively, reveals that the grain center mostly has a residual beta phase. These results indicate that the crack likely initiates from a residual β phase without alpha-phase precipitation. G. Lütjering et al. reported that fracture deformation in high-strength Al and Ti alloys preferentially occurs at the grain boundary owing to the soft precipitation-free zones (PFZs) lacking solute atoms [72]. Although this conclusion is inconsistent with the present findings, the PFZ theories support the findings of this study. This is because the PFZs in CP material also exist in the center

of the grain owing to the incomplete alpha-phase precipitation process from aging. Therefore, the PFZs at both the grain boundary and the grain center can deform; the crack is initiated at either of these locations.

The nano-CT image projected on a plane perpendicular to the loading axis is shown in Fig. 4-13 (c). Similar to that observed in the micro-CT images in Fig. 4-7, an open crack is reflected by the shadow feature. The crack propagation is restrained by the grain boundary, as indicated by the red arrow. This phenomenon is referred to as the grain boundary blocking effect, which occurs when the crack size is similar to or below the grain size order [66–68]. Therefore, it can be concluded that, at the early stage of a crack, its facet-like behavior and boundary blocking effect can be captured by nano-CT.

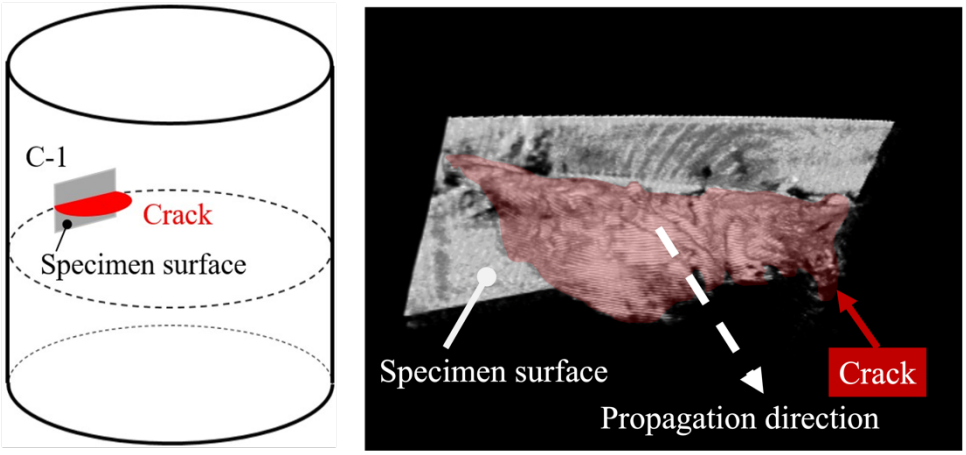
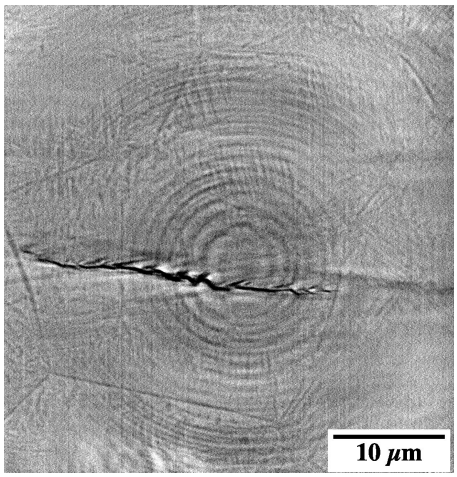
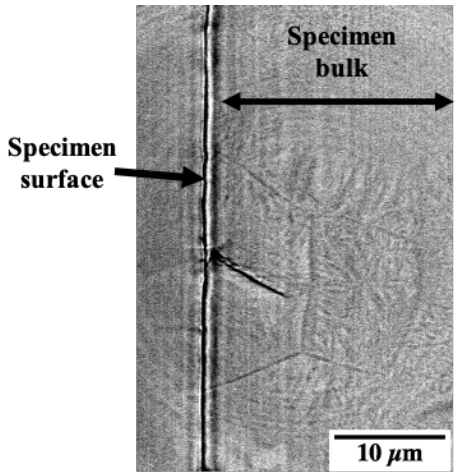


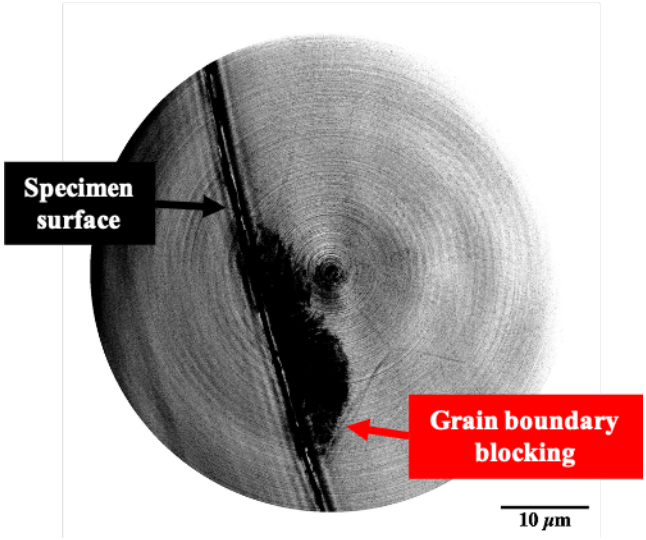

Fig. 4-12. 3D morphology of C-1 at 1500 cycles by nano-CT (CP material)



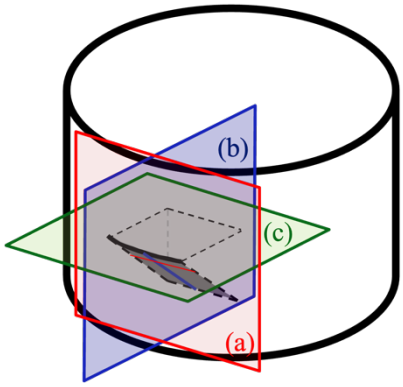

(a) Longitudinal section
(parallel to crack length direction)




(b) Longitudinal section
(parallel to crack depth direction)




(c) Crack projected on a plane
perpendicular to the loading axis




(d) Schematic of sectioning
and projection view

Fig. 4-13. Nano-CT images of main crack C-1 at 1500 cycles (CP material)

## 4.5 Summary of Chapter 4

Chapter 4 introduced the attempt to obtain small crack initiation and propagation behavior by multiscale SR-CT. CP material was applied to evaluate the imaging quality. Meanwhile, the detail of the *in situ* piezo fatigue testing system is presented.

As a result, the multiscale SR-CT system with the new developed *in situ* piezo fatigue testing system is able to capture the just-initiated crack within a size of 10 μm and observe the crack propagation process till the fracture. The 3D rendering of the crack is also achieved.

It was observed that the small crack was significantly affected by the local microstructure. The crack initiation site was located at the PFZs, and the following propagation was strongly hindered by the grain boundary. In the propagation process, small cracks exhibited an unstable crack-shape behavior at the early stage but gradually approached a semicircular shape. The d$a$/d$N$–Δ$K$ for five cracks illustrated a good agreement, indicating that the crack-shape evolution was negligibly related to d$a$/d$N$–Δ$K$. On the other hand, the crack initiation rate exhibited lesser deviation and was larger than the crack propagation rate, which can be explained by the uniform crack-initiation mechanism and the relatively low crack-growth resistance at the PFZs.

# Chapter 5

## Full-life growth behavior of a naturally initiated internal fatigue crack by multiscale SR-CT

# 5. Full-life growth behavior of a naturally initiated internal fatigue crack by multiscale SR-CT

After understanding the importance of the microstructural effect on small cracks introduced in Chapter 4, the author conducted the *in situ* multiscale SR-CT test to observe the growth process of a naturally initiated internal fatigue crack. The author especially focused on the crack fronts which were significantly influenced by microstructure. The experimental details will be introduced in the following contents. Different to chapters 3 and 4 where CP material was used in the experiment, in this chapter, FP material was applied due to the higher industrial interests from its better mechanical properties.

## 5.1. Methodology

### 5.1.1 Materials and specimens

The applied material was the FP material with a fine and homogeneous alpha-phase precipitation. The microstructure and mechanical properties of the FP materials are presented in Fig. 5-1 (same as Fig. 2-1 (a)) and Table 5-1 (included in Table. 2-2), respectively. The reason for adopting FP instead of CP was that FP has better mechanical properties and higher industrial interests. On the other hand, due to the increase in test loading, the screw portion of the specimen configuration used in Chapter 4 for CP can be fractured before the specimen. Therefore, the design of the specimen was changed into a male type as shown in Fig. 5-2 to reduce the stress on the screw portion. The control volume of the specimen was first lathe-turned to a diameter of 0.8 mm with a length of 3 mm. Then, to remove the hardened layer resulting from the lathe-turning process, the control volume was sequentially polished to a diameter of 0.6 mm using #800 – #2000 emery papers. The corresponding transmittance for 30 keV X-rays was ~23% for the 0.6 mm specimen.

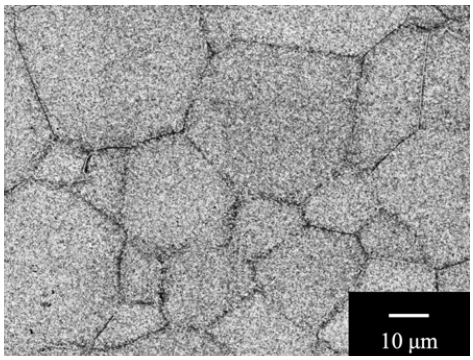



Fig. 5-1. SEM image of the microstructure of the heat-treated alloy Ti-22V-4Al, with a homogenous and fine alpha-phase precipitation (FP material, the same as Fig. 2-1 (a))

Table 5-1. Mechanical properties of the heat-treated alloy Ti-22V-4Al with FP material.

| 0.2% Proof Stress [MPa] | Tensile Strength [MPa] | Elongation [%] | Reduction of Area [%] |
|---|---|---|---|
| 1154 | 1235 | 9.3 | 21.9 |

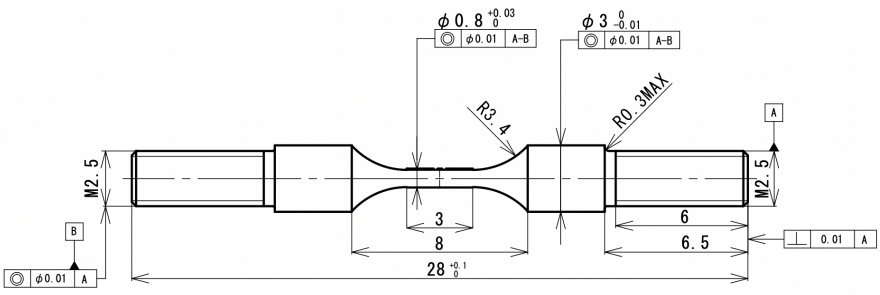



Fig. 5-2. Configuration of the small specimen (units: mm)

5.1.2 Fatigue properties of the FP small specimen

With the decrease of specimen diameter, the fatigue properties in terms of internal fatigue fracture can be different from the large size specimen, which is the so-called “control volume effect”. Therefore, the fatigue properties of FP small specimens are required to be obtained for determining the imaging interval.

The fatigue properties of the small specimen (configuration in Fig. 5-2) and the specimen used for obtaining fatigue properties (4mm in diameter, configuration shown in Fig. 2-2, fatigue properties included in Fig. 2-5) are shown in Fig. 5-3. The fatigue tests were conducted at a frequency of 120 Hz and a stress ratio of $R = 0.1$. A deviation of fatigue properties can be found between two type of specimen configurations, which represented the above-mentioned “control volume effect”. Focus on the small specimen, the fatigue strength decreased with an increase in fatigue life throughout the run-out range. The surface fractures exhibited a relatively shorter fatigue life than the internal fractures did. Moreover, internal fractures occurred in the regime of $10^5$ order cycles, which was relatively shorter than that of the VHCF regime. Therefore, the applied beta titanium alloy has a pronounced fatigue strength but a relatively early fatigue life for internal fractures. In this study, the *in situ* fatigue test condition for CT imaging was determined to be 120 Hz, $R = 0.1$, and the maximum stress of 1050 MPa, which was 91% of the proof stress. The internal fracture monitored in the SR-CT test is shown in Fig. 5-3, with a circular frame.

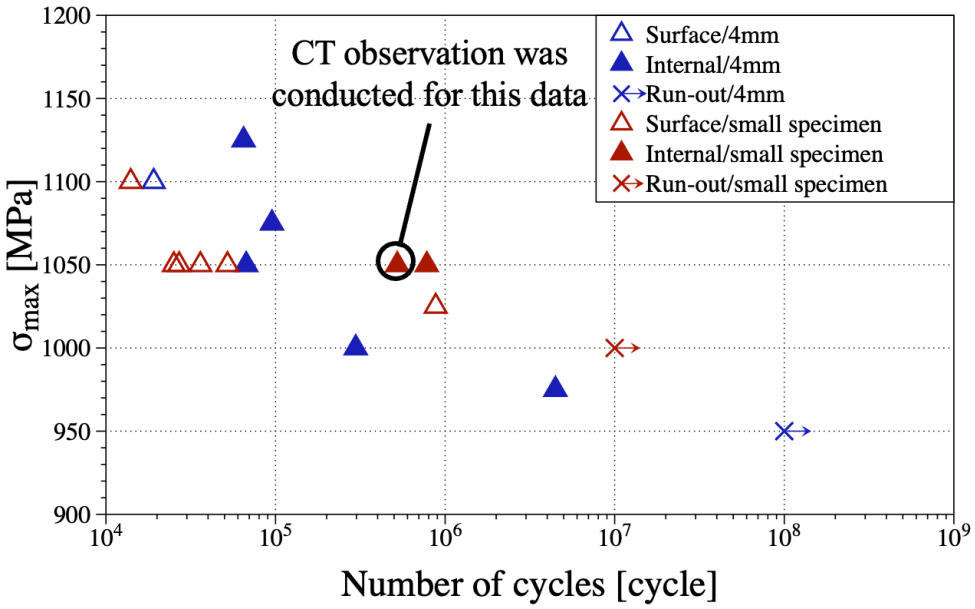



Fig. 5-3. Fatigue properties of the small specimen and 4 mm specimen in FP material. Test frequency is 120 Hz and stress ratio is $R = 0.1$

5.1.3 Procedure for the *in situ* fatigue test and CT observations

The experimental procedure was as follows. First, a micro-CT image was taken before the fatigue test. The fatigue test and micro-CT measurements were repeated until the specimen was fractured.

To detect crack initiation, the imaging procedure was determined as follows: as shown in Fig. 5-3, the fatigue data of the applied stress level represents surface and internal fracture before $1.00 \times 10^5$ cycles and before $1.00 \times 10^6$ cycles, respectively. Therefore, to detect the potentially initiated surface crack, micro-CT was conducted every $1.00 \times 10^4$ cycles until $1.00 \times 10^5$ cycles. After $1.00 \times 10^5$ cycles, micro-CT was conducted at $2.00 \times 10^5$ cycles and continued with an interval of $2.00 \times 10^5$ cycles for any initiated internal crack. The micro-CT images at each number of cycles were manually examined, and the test was continued to the next step until cracks were initiated. When the crack initiation was captured, nano-CT measurements were performed at the early stage of crack growth to obtain magnified details. The imaging conditions for the micro-CT and nano-CT are listed in Table 5-2.

To compare the crack opening behavior under various loading conditions, the author applied two loading conditions during the observation of micro-/nano-CT: 0% and 80% loadings, which represent a condition without a tensile load and a condition with a tensile load equivalent to 80% of the maximum stress of the fatigue test. The obtained CT images were analyzed using the “ImageJ” imaging processing program [63]. Fractography analysis was conducted using SEM with three-dimensional (3D) analysis functions (Keyence VE-9800).

Table 5-2. Imaging conditions of micro-CT and nano-CT

| Imaging mode | Micro-CT | Nano-CT |
|---|---|---|
| X-ray energy (keV) | 30 | 30 |
| Exposure time (msec) | 50 | 500 |
| Voxel size (μm) | 0.5 | 0.08 |
| Field of view (mm × mm) | 1 × 1 | 0.06 × 0.06 |
| Total scan duration (min) | ~5 | ~30 |

5.2 Overall crack growth behavior via multiscale-CT

Micro-CT images under 80% loading were projected onto a plane perpendicular to the loading axis, as shown in Fig. 5-4. Each image was projected from 500 layers of micro-CT images. The dark shadowed pattern represents an open crack. During the entire fatigue test, only one internal crack and no surface cracks were observed in the bulky specimen. The internal crack was detected at $4.00 \times 10^5$ cycles and could not be recognized in the previous imaging step at $2.00 \times 10^5$ cycles. After crack initiation, cracks gradually propagated inside the material. At $5.21 \times 10^5$ cycles, this internal crack front reached the specimen surface and transitioned to a surface crack. The last micro-CT scan was recorded at $5.22 \times 10^5$ cycles. The specimen fractured only after $0.00221 \times 10^5$ cycles, which was negligible for the total fatigue life. Consequently, the fatigue life ($N_f$) was determined to be $5.22 \times 10^5$ cycles. The internal crack initiated between the number of cycles of the first crack detection and that of the previous imaging step; therefore, in this study, the author defined the crack initiation life ($N_i$) as the average value between these two values, which was $3.00 \times 10^5$ cycles. Accordingly, the crack propagation life ($N_p$) was determined to be $2.22 \times 10^5$ cycles, which was the $N_f$ except $N_i$. In this study, $N_i$ and $N_p$ of the internal cracks accounted for 57% and 43% of $N_f$, respectively.

However, in the early stages, the crack front was difficult to be determined using micro-CT owing to its relatively low spatial resolution. The nano-CT images at $4.00 \times 10^5$ and $4.40 \times 10^5$ cycles are shown in Fig. 5-5. The loading condition was 80%, which was the same as that in the micro-CT images shown in Fig. 5-4. Each image was projected from 400 layers of nano-CT. Compared with the micro-CT images under the same number of cycles as shown in Fig. 5-4, the crack front captured using nano-CT was more clearly recognized than that using micro-CT. Moreover, a portion of the crack front exhibited an unnatural linear shape, as indicated by the red arrows. Similarly, the linear shape crack front could also be recognized in the magnified micro-CT images of $4.80 \times 10^5$ and $5.10 \times 10^5$ cycles shown in Fig. 5-6, which implies that the crack growth was restrained by the local microstructure, such as the grain boundary blocking effect [66,67].

In addition, the 3D rendering of the crack growth was reconstructed, as shown in Fig. 5-7. A profile reference line was added to exhibit the crack-growth morphology. The cracks of the $4.00 \times 10^5$ and $4.40 \times 10^5$ cycles were obtained using nano-CT, whereas the others were obtained using micro-CT. The crack growth was observed to be uneven: first, after $4.00 \times 10^5$ cycles, the crack front on the left side propagated on a plane approximately 45° to the loading direction; however, the crack growth on the right side was blocked. The crack front at $5.10 \times 10^5$ cycles was located on both planes, at 45° and perpendicular to the loading direction. Finally, the crack front at $5.21 \times 10^5$ cycles was mostly on the plane perpendicular to the loading direction. The complex crack growth behaviors signify the interaction between the crack front and local microstructure.

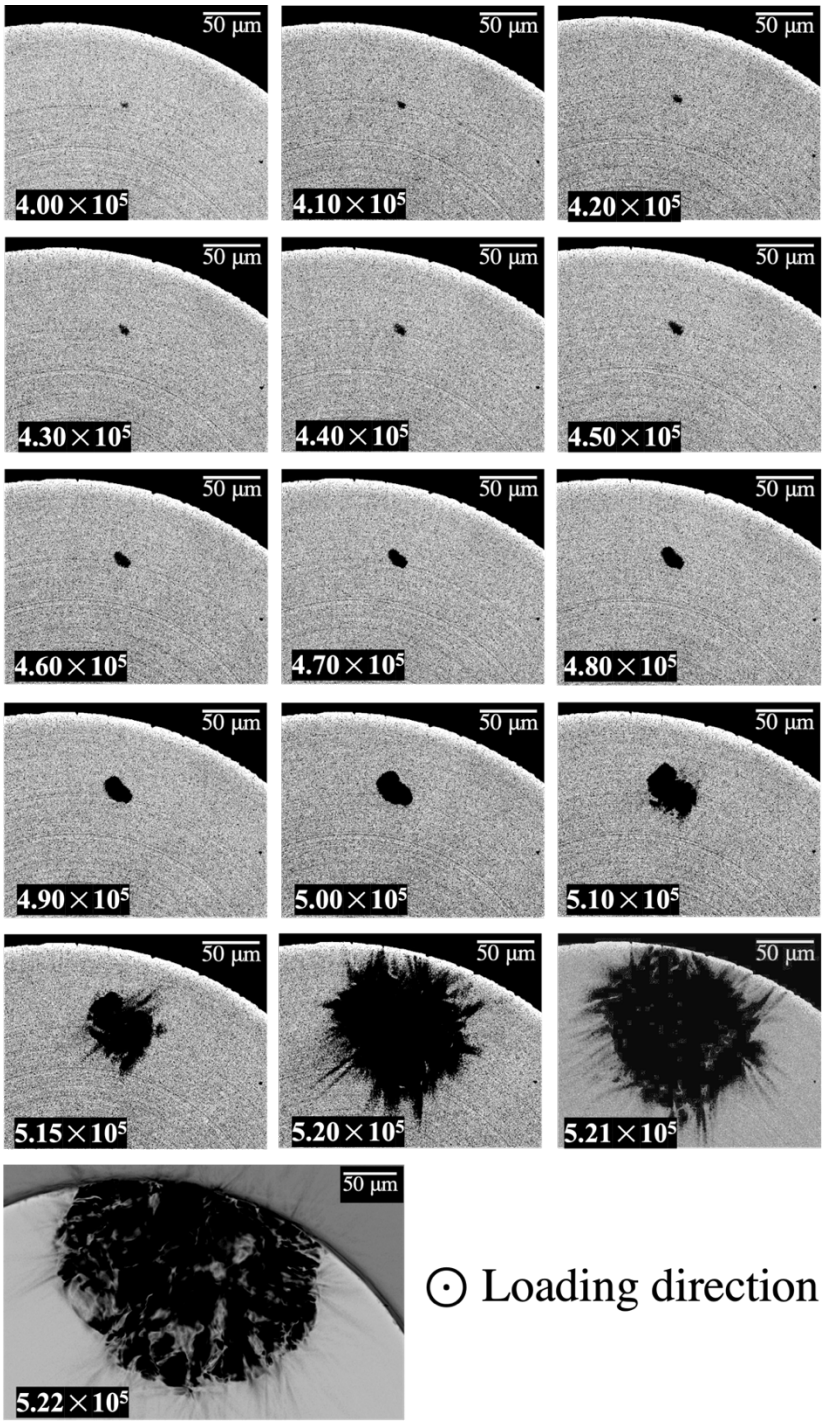



Fig. 5-4. Propagation process of an internal crack is shown by projecting micro-CT images under 80% loading on a plane perpendicular to the loading axis in FP material (unit: cycles)

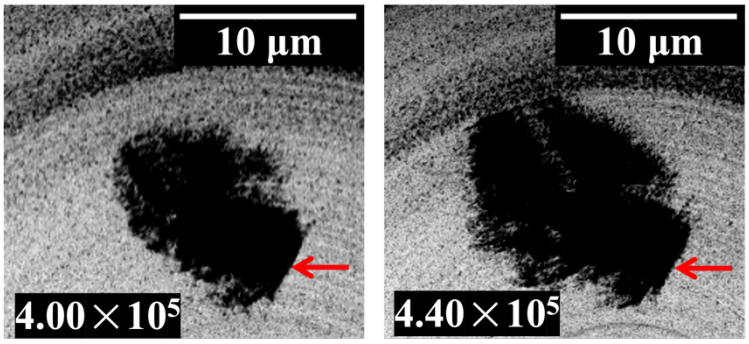



Fig. 5-5. Propagation process of an internal crack in its early stage is shown by projecting nano-CT images under 80% loading on a plane perpendicular to the loading axis in FP material (unit: cycles). Linear crack fronts are indicated by red arrows

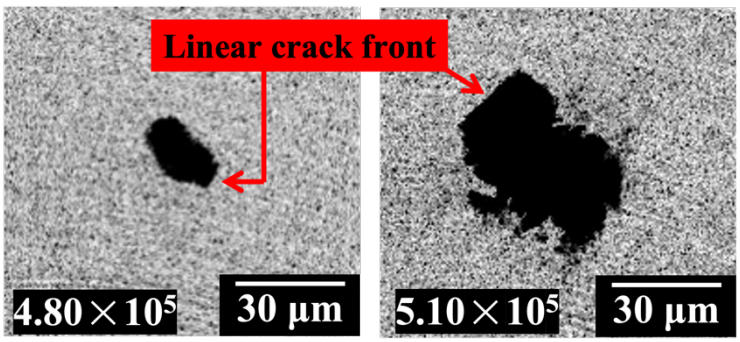



Fig. 5-6. Magnified micro-CT images of the crack at 4.80 × $10^5$ and 5.10 × $10^5$ cycles (FP material). Linear crack fronts are indicated by red arrows

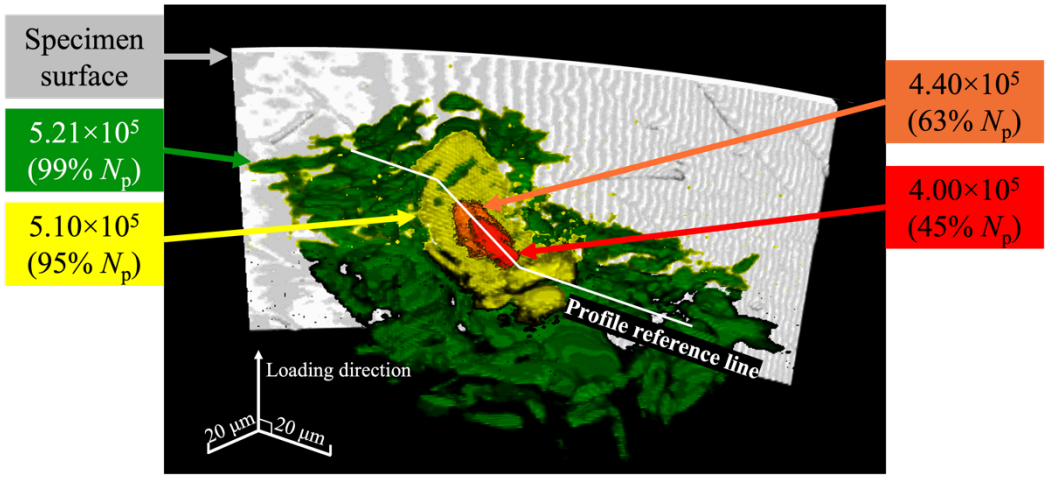


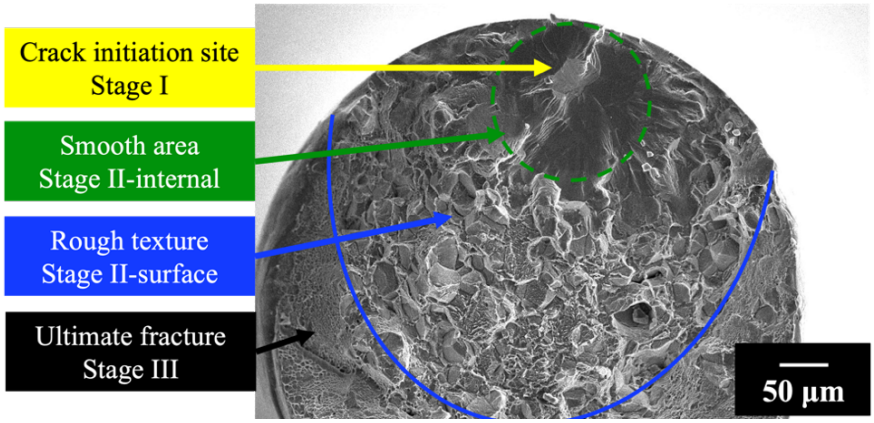

Fig. 5-7. 3D rendering results of the crack growth process (FP material).

5.3 Fractography features with regard to crack growth stages

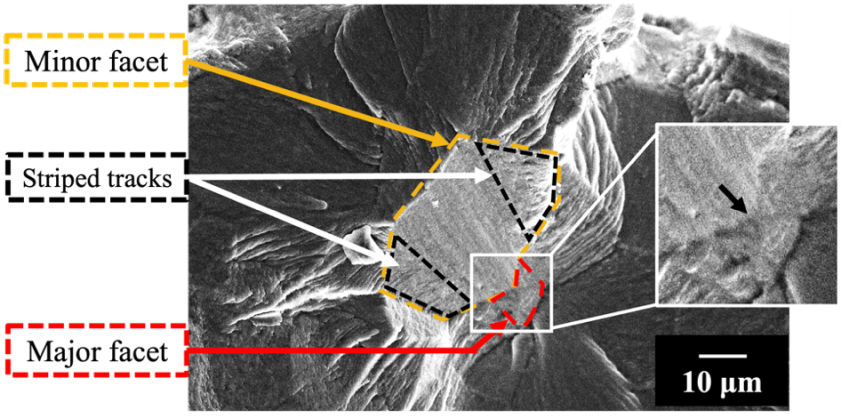
After the specimen was fractured, the fracture surface was observed using SEM, as shown in Fig. 5-8. In the low-magnification 2D-SEM image (Fig. 5-8 (a)), only one crack initiation site was observed at the fracture surface. Surrounding the initiation site, a smooth texture with an internal tangent circle ranging to the specimen surface could be recognized, which is referred to as the “smooth area” introduced in Chapter 2. Outside the smooth area, the fracture surface exhibited a rough texture, including intergranular fractures and dimples. The outermost represented a plastic deformation feature which corresponded to the ultimate fracture. Focusing on the magnified crack initiation site shown in Fig. 5-8 (b), two combined facets were observed, and they were separated by a clear boundary indicated by a black arrow. As mentioned in Chapter 2, this feature is called multiple facets, the formation of which significantly influences the internal crack growth in beta titanium alloys. The author pointed out that the formation of multiple facets is sequential rather than simultaneous. The major facet, which represents the first initiated facet, had no striped tracks on its surface. On the contrary, on the surface of the minor facet, which represents the subsequently initiated facet, striped tracks were recognized. The major and minor facets and striped tracks are shown in Fig. 5-8 (b). Fig. 5-8 (c) shows the 3D-SEM image with profile data at the largest gradient of the multiple facets, represented by white lines. The solid circles in the 3D-SEM image and profile graph indicate the same locations. The multiple facets were well aligned and were approximately 45° to the loading direction, indicating that the formation of the multiple facets was due to slippage. Moreover, the smooth area excluding multiple facets was horizontal to the X-Y surface, which implies that the crack propagation processes were different between the multiple facets and the smooth area.

Based on fractography, the crack growth stages are generally classified into three stages: Stages I, II, and III, [73]. Stage I is generally defined as the crack propagation by slip-plane fracture at approximately 45° to the stress axis. Stage II is corresponding to the crack propagation process which is usually normal to the direction of maximum tensile stress. Stage III represents the last stress cycle when the cross section can no

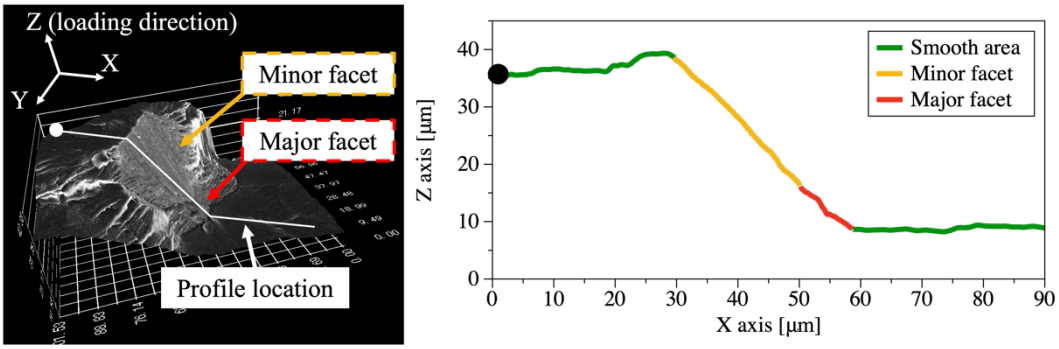
longer sustain the applied stress. The above growth stages are integrated into Fig. 5-8 (a) and (b) based on fractography features. In the present study, multiple facets represent Stage I (Fig. 5-8 (b)). In the case of Stage II, the smooth area represents the internal crack propagation in the matrix, thus is described as Stage II-internal. The rough texture, including intergranular fractures and dimples, represents the surface crack propagation, and is described as Stage II-surface. In addition, the plastic deformation feature representing the ultimate fracture, is described as Stage III.




(a) Low-magnification 2D-SEM image of fracture surface.




(b) High-magnification 2D-SEM image on the crack initiation site; the boundary separating the major and minor facet indicated by black arrow.




(c) 3D-SEM image with profile data at the largest gradient of the multiple facets indicated by white lines. The solid circles in the 3D-SEM image and profile graph indicate the same locations.

Fig. 5-8. SEM fractography results (FP material)

## 5.4 Comparison between fractography and SR-CT images

In fractography, each crack growth stage was clearly distinguished; however, it was still difficult to determine when and how the crack front extended during fatigue loading. In this study, SR-CT images are superimposed on the fracture surface to investigate this information further.

### 5.4.1 Stage I

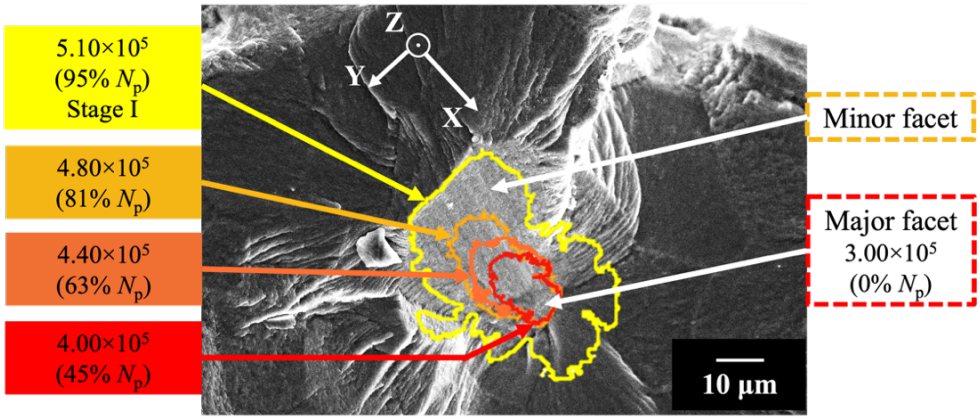
The crack fronts obtained using SR-CT were superimposed on a 2D-SEM image, as shown in Fig. 5-9. The crack fronts of the $4.00 \times 10^5$ and $4.40 \times 10^5$ cycles were obtained using nano-CT, whereas the other crack fronts were obtained using micro-CT.

Fig. 5-9 (a) shows a high-magnification view of the crack growth related to multiple facets. The coordinate in the 3D-SEM image (see Fig. 5-8 (c)) was also added. The linear crack front observed through SR-CT (Fig. 5-5 and Fig. 5-6) corresponded to the boundaries of multiple facets. The crack growth on the major and minor facets exhibited dissimilar behavior. The first crack was detected after $4.00 \times 10^5$ cycles; the crack front consisted of the entire major facet and a small area of the minor facet, indicating that the formation of multiple facets was sequential rather than simultaneous. Until $4.80 \times 10^5$ cycles, on the one hand, the crack propagated on the minor facet side more significantly along the X axis than the Y axis. On the other hand, the crack front was blocked by the major facet side, indicating that the multiple facets formation was uneven, and the resistance against crack growth was smaller in the minor facet growth process than in overcoming the grain boundary blocking effect. After $4.80 \times 10^5$ cycles, the major facet side overcame the blocking and started to propagate into the matrix. However, the minor facet side remained in the multiple facets regime. At $5.10 \times 10^5$ cycles, the crack front reached the boundary of the minor facet which was perpendicular to the X axis, indicating that crack growth on 45° related to multiple facets was accomplished. However, the stripe tracks indicated in Fig. 5-8 (b) on minor facet were not included in the crack front of $5.10 \times 10^5$ cycles. This phenomenon implies that the stripe tracks were formed in Stage II, leading it becomes a significant feature to distinguish the major and minor facet.

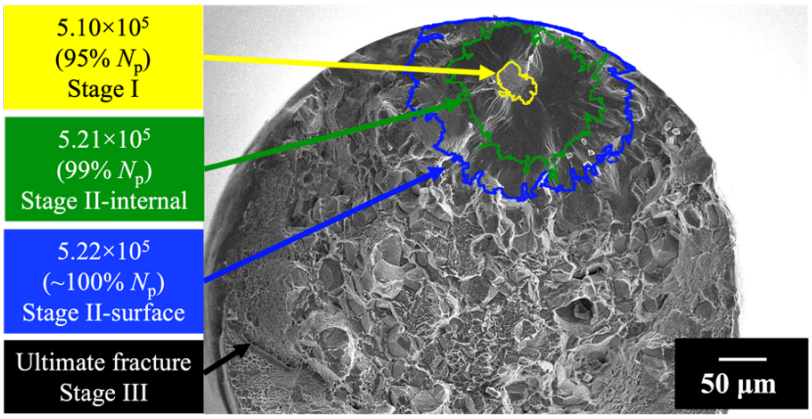
Consequently, Stage I was estimated to begin after the crack initiation ($3.00 \times 10^5$ cycles, 0% $N_p$) and finish at $5.10 \times 10^5$ cycles. This value corresponded to 95% of $N_p$, indicating that the internal fracture in beta titanium alloys was dominated by the multiple facets formation.

### 5.4.2 Stage II

Fig. 5-9 (b) shows a low-magnification view describing the relationship between the crack front behavior and fractography features (i.e., multiple facets, smooth area, rough texture). The crack front of $5.21 \times 10^5$ cycles, at which the crack front reached the specimen surface, was consistent with the boundary of the smooth area shown in Fig. 5-8 (a). Furthermore, the surface crack propagation process between the $5.21 \times 10^5$ and $5.22 \times 10^5$ cycles exhibited a range included in rough texture in Fig. 5-8 (a). Thus, Stage II-internal, which was represented by the smooth area, was processed between $5.10 \times 10^5$ and $5.21 \times 10^5$ cycles, representing 4% of $N_p$. Similarly, Stage II-surface, represented by the rough texture, consumed ~$0.01 \times 10^5$ cycles and occupied ~1% of $N_p$. Therefore, in this study, Stages II only accounted for 5% of $N_p$, indicating that the distance from the multiple facets to the specimen surface did not significantly influence the fatigue life of the internal fractures in the beta titanium alloy.




(a) High-magnification view of the crack initiation site.




(b) Low-magnification view of the fracture surface.

Fig. 5-9. 2D-SEM image superimposed with crack fronts under various number of cycles (FP material)

5.5 Crack opening and blunting behavior during crack growth on multiple facets

In Section 5.4, the crack propagation on the major facet side was blocked until $4.80 \times 10^5$ cycles. Herein, the trigger for overcoming the blocking effect is discussed in terms of the crack opening and blunting behavior. The CT images were re-sliced for the longitudinal sections along the profile line shown in Fig. 5-8 (c), illustrating the largest gradient of the multiple facets. Re-sliced micro-CT images of the longitudinal sections of the internal cracks are shown in Fig. 5-10. Crack images were obtained using the same contrast adjustment. Therefore, the crack opening displacement (*COD*) could be qualitatively reflected by the various pixel intensities of the crack.

In the images of 0% loading shown in the left column in Fig. 5-10, cracks were hardly observed at $4.00 \times 10^5$ cycles immediately after its initiation. Then, the crack gradually became apparent and finally reached a consistent *COD* at approximately $4.80 \times 10^5$ cycles. Conversely, in the images with 80% loading shown in the middle column in Fig. 5-10, during the increase in loading cycles, the crack maintained similar visibility and was recognized more easily than the crack under 0% loading. Therefore, the crack under 80% loading had a relatively consistent and large *COD* regardless of the loading cycles. Consequently, the range of *COD* ($\Delta COD$, from 80% to 0% loading in the present study) decreased with increasing loading cycles. A schematic of the crack blunting process is shown in Fig. 5-11. The increase in the crack length is not shown in the schematic. With the increase in the loading cycles, the *COD* at high-stress levels (② and ④) remained consistent, whereas the *COD* at low-stress levels (①, ③, and ⑤) increased with an increase in loading cycles and finally reached a certain value. This trend suggested that the irreversible deformation of the crack tips accumulated and saturated during the loading cycles, which was strongly related to the blunting process at the crack tips.

Regarding the relationship between crack blunting and crack propagation, Lankford et al. mentioned that a crack cannot propagate until it reaches its limit [74]. Based on this concept, crack blunting could be key to triggering cracks to overcome the blocking effect. To determine when the crack overcame the blocking effect, the

blocked crack tip on the major facet side under 80% loading was magnified with a reference line, as shown in the right column of Fig. 5-10. Up to $4.80 \times 10^5$ cycles, the crack tip did not extend; after $4.80 \times 10^5$ cycles, the crack started to propagate horizontally into the matrix. As mentioned earlier, $\Delta COD$ became constant at approximately $4.80 \times 10^5$ cycles; therefore, the crack blunting process and its saturation based on the accumulation of irreversible deformation were considered critical for the internal crack to propagate into the adjacent grain.

In addition, internal cracks were observed with a more significant blunted tip than the surface cracks in Ti-6Al-4V [58]. Therefore, the crack blunting process possibly requires more cycles in internal cracks than in surface cracks, which leads to a longer fatigue life for internal fatigue fractures. However, the crack on the side of the minor facet could easily propagate under the same $\Delta COD$ at which the crack tip on the side of the major facet was blocked. This indicates that the minor facet had a smaller resistance against crack growth than the grain boundary blocking effect. Considering these, the effect of the local microstructure is indispensable for accurately understanding the behavior and life consumption of the crack blunting process.

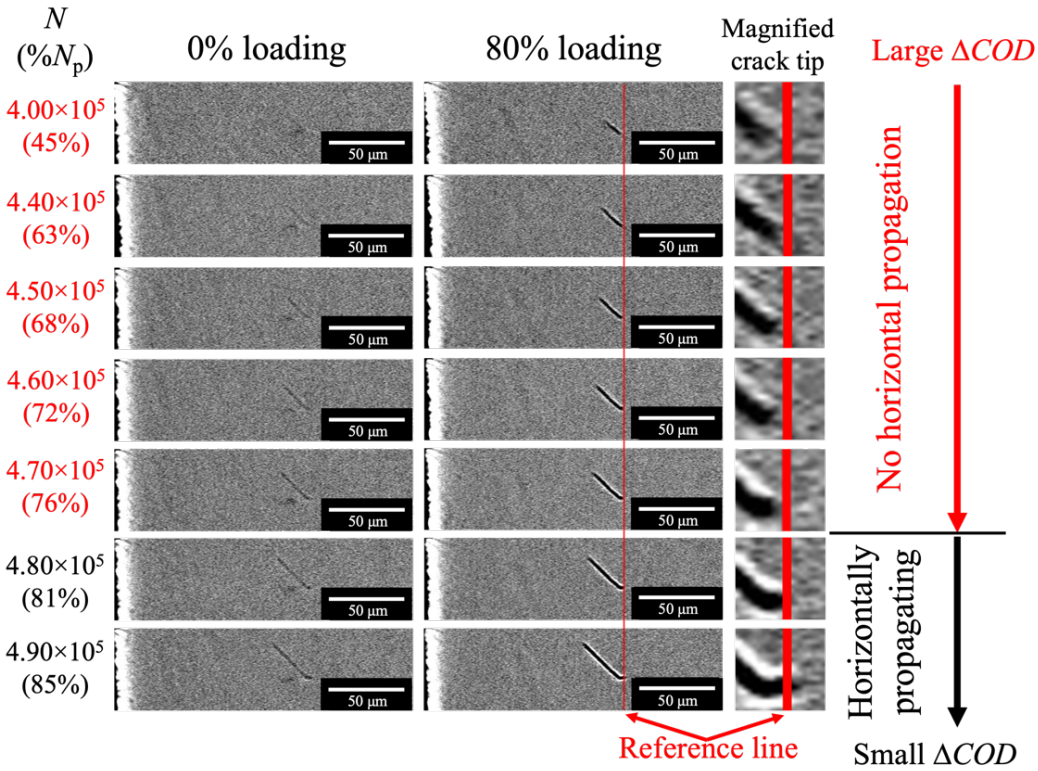



Fig. 5-10. Micro-CT images of the longitudinal sections of the internal crack illustrating the crack blunting process (FP material)

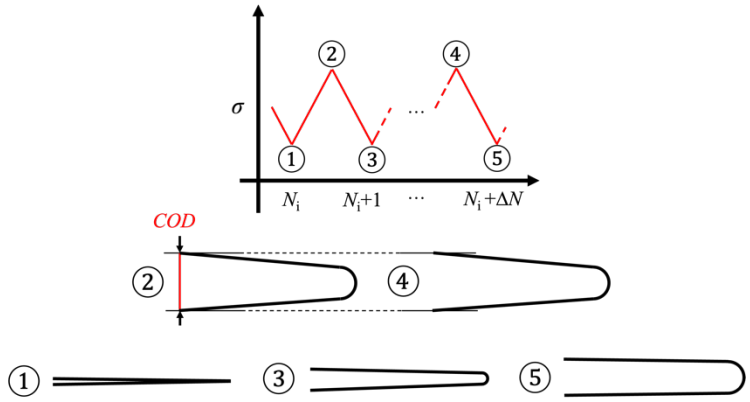



Fig. 5-11. Schematic of the crack blunting process during a fatigue test. Note that the increment of the crack length is not provided in the schematic

5.6 Crack propagation rate

The crack propagation rate was demonstrated by its relationship with the stress intensity factor range $\Delta K$ in this study. As a three-dimensional asymmetric crack, the crack sizes were represented by the root of the area of the crack projected onto the plane perpendicular to the loading axis, $\sqrt{area}$ [5]. The crack area between $4.00 \times 10^5$ and $4.40 \times 10^5$ cycles was measured from the nano-CT images, and the others were obtained from the micro-CT images. The crack area was measured five times for each cycle. The maximum coefficients of variation for the internal and surface cracks were 8.9% and 3.7%, respectively. Then, the corresponding $\Delta K$ values for the surface and internal cracks were calculated using Murakami's equations described in Eqs. (5-1) and (5-2), respectively [5].

$$\Delta K = 0.65\Delta\sigma\sqrt{(\pi\sqrt{area})} \text{ (surface crack),} \quad (5\text{-}1)$$

$$\Delta K = 0.5\Delta\sigma\sqrt{(\pi\sqrt{area})} \text{ (internal crack),} \quad (5\text{-}2)$$

where $\Delta\sigma$ is the range of applied stress. Finally, to allow the present work to be comparable with the conventional d$a$/d$N$−$\Delta K$ curve, the d$\sqrt{area}$/d$N$ for the surface and internal cracks were adjusted using a coefficient, as described in Eqs. (5-3) and (5-4), respectively.

$$\frac{2}{\sqrt{\pi}} \times d\sqrt{area}/dN = da/dN \text{ (surface crack),} \quad (5\text{-}3)$$

$$\frac{1}{\sqrt{\pi}} \times d\sqrt{area}/dN = da/dN \text{ (internal crack),} \quad (5\text{-}4)$$

where the internal crack length is defined as an embedded circular internal crack in infinite bulk [75]. In the case of a surface crack, the crack length is defined as equal to the crack depth [69]. Consequently, the crack propagation rate was described by the d$a$/d$N$−$\Delta K$ curve derived from the $\sqrt{area}$. The d$a$/d$N$–$\Delta K$ curve of the monitored internal crack is shown in Fig. 5-12. For comparison, using the same type of alloy Ti-22V-4Al, a surface crack d$a$/d$N$−$\Delta K$ obtained through a compact tension test

conducted by Tokaji et al. [33] is shown in Fig. 5-12. Consequently, the propagation rate of the internal cracks was slower than that of the surface cracks at the same $\Delta K$, with a maximum difference of two orders of magnitude in the low $\Delta K$ regime, and this difference decreased with the increase in $\Delta K$. Moreover, the surface crack propagation rate obtained was generally in agreement with that reported by Tokaji et al., indicating the reproducibility of the present study.

In addition, the crack growth stages defined in Section 5.3 are described individually by the $da/dN-\Delta K$ curve with the equations and the fraction of $N_p$ in Fig. 5-12. The curvature was obtained using the LOESS method, and linear relationships were calculated through least square linear regression. The $R^2$ values for all regimes exceeded 98%. Consequently, apparent shape changes were observed in the $da/dN-\Delta K$ curve between each crack growth stage.

First, in the early Stage I, the crack blunting regime in which the crack only propagated on multiple facets in a 45° direction, exhibited a curvature shape $da/dN-\Delta K$. It is because the "driving force" for crack propagation equivalent to the gradient of $da/dN-\Delta K$ curve, is related to $\Delta COD$ which decreases during the crack blunting process. Then, in the remaining Stage I, the crack propagated on both multiple facets (45° direction) and the matrix (horizontal direction), exhibiting a linear shape associated with the Paris law. After reaching Stage II-internal, the crack fully propagated horizontally in the matrix; and $da/dN-\Delta K$ still followed the Paris law but under a larger gradient, implying that there was less resistance to crack propagation in Stage II-internal than in Stage I. Finally, in Stage II-surface, the $da/dN-\Delta K$ transitioned similarly to that of a surface crack. These shape changes indicate that the crack growth stages can be reflected by the $da/dN-\Delta K$ curve. In addition, the characteristics of the monitored internal cracks in terms of the crack growth stages are listed in Table 5-3. Each growth stage corresponded to a fractography feature, crack behavior, and $da/dN-\Delta K$ curve feature.

Notably, in this study, only one crack growth behavior was observed, and the crack initiation life (number of cycles before Stage I) appeared to dominate the fatigue life of the internal fracture. However, a previous study on Ti-6Al-4V identified that

the $N_i$ of internal cracks could range from 20 to 70% of the fatigue life, but had little influence on the propagation behavior [53]. Therefore, the crack propagation rate in the present study can be considered reproducible. In addition, future studies should focus on crack initiation and Stage I behavior to thoroughly understand the internal fatigue fractures in beta titanium alloys.

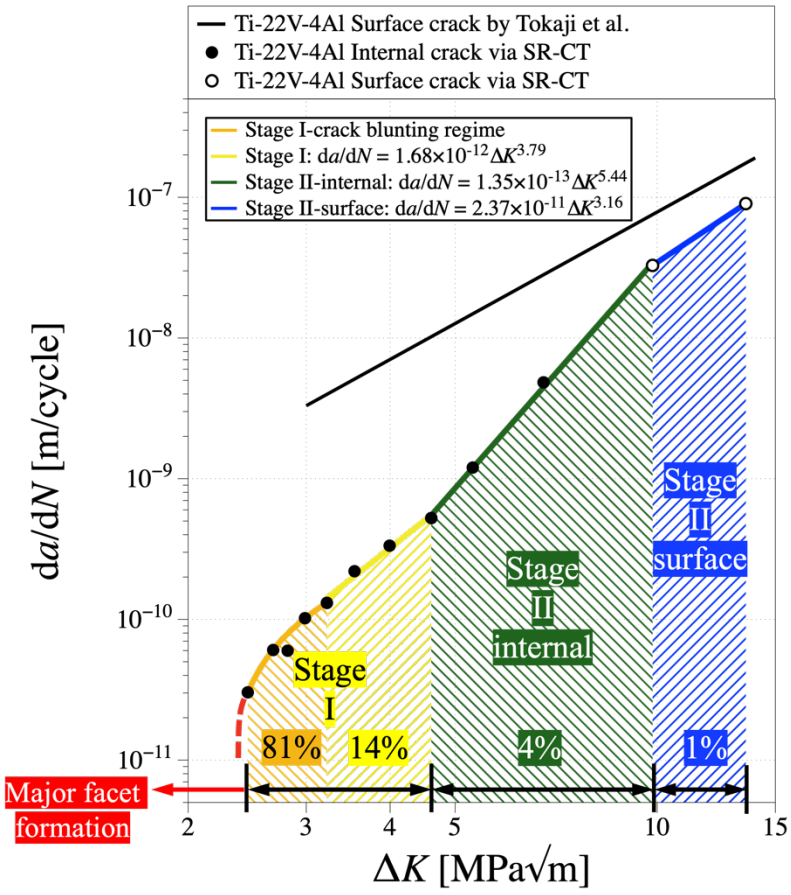



Fig. 5-12. Crack propagation rate with the crack growth stages and fraction of crack propagation life $N_p$ (FP material)

Table 5-3. Characteristics of crack growth stages of the monitored internal crack

| Stage | | Fractography | Crack behavior | $da/dN-\Delta K$ | $\%N_p$ | $\%N_f$ |
|---|---|---|---|---|---|---|
| - | | Major facet | Crack initiation | - | - | 57% |
| I | | Multiple facets | Crack blunting with 45° propagation | Curvature | 81% | 43% |
| | | | 45° and horizontal matrix propagation | Linear under the Paris law | 14% | |
| II | internal | Smooth area | Horizontal matrix propagation | Linear under the Paris law | 4% | |
| | surface | Rough texture | Horizontal matrix propagation | Linear under the Paris law | 1% | |
| III | | Plastic deformation | Ultimate fracture | - | - | - |

## 5.7 Summary in Chapter 5

This experiment monitored a naturally initiated internal crack in FP material via *in situ* fatigue tests using multiscale X-ray tomography comprising micro-CT and nano-CT. The crack fronts at various cycles were superimposed on the fracture surface from the perspective of crack growth stages, including Stage I, Stage II-internal, Stage II-surface, and Stage III. The crack propagation process consisted of multiple facets formation (Stage I) and subsequent growth into the matrix (Stage II-internal/surface) and was dominated by the former process. The crack opening and blunting behaviors triggered crack growth from the facets to the surrounding matrix. The relationship between crack propagation rate with stress intensity factor range ($\mathrm{d}a/\mathrm{d}N$-$\Delta K$) was successfully obtained for internal fatigue crack in beta titanium alloy. The overall crack propagation rate of the internal crack was revealed to be slower than the surface crack.

# Chapter 6

## Effect of environment and microstructure on internal crack propagation

# 6. Effect of environment and microstructure on internal crack propagation

The internal fatigue crack behaviors in beta titanium alloy have been directly observed. However, why the internal fracture could occur much earlier than the VHCF regime mentioned in Chapter 2 has not been answered. In Chapter 6, the reason will be discussed from viewpoint of crack propagation. The internal crack propagation of beta titanium alloy will be compared with that of a dual-phase (alpha + beta) titanium alloy Ti-6Al-4V whose internal fractures start to occur in the VHCF regime. Furthermore, the difference in their crack propagation rate is discussed based on the environment surrounding the crack, thus surface crack growth tests in a vacuum have been conducted for beta titanium alloy with FP microstructure, which is the same as the material used for the internal crack observation by SR-CT. In addition, the microstructural factors influencing the internal crack propagation rate are also discussed.

## 6.1 Comparison of fatigue properties and crack propagation behaviors between beta and (alpha + beta) titanium alloys

The fatigue properties under stress ratio 0.1 of the applied beta titanium alloy Ti-22V-4Al (FP material, fatigue properties also included in Fig. 2-5) and a dual-phase (alpha + beta) titanium alloy Ti-6Al-4V are shown in Fig. 6-1. The earliest internal fatigue fracture in Ti-6Al-4V occurred around $10^7$ cycles, which is 100 times longer than that of FP material represented in $10^5$ cycles. To clarify the reason in terms of crack propagation, their crack propagation rate was compared as shown in Fig. 6-2. Focusing on internal crack propagation rate plotted by solid marks, the internal crack

propagation rate of Ti-6Al-4V is in the range of $10^{-14}$ ~ $10^{-10}$ m/cycle. However, the internal crack propagation rate of FP material is in the range of $10^{-11}$ ~ $10^{-8}$ m/cycle, which is about 100 times faster than that of Ti-6Al-4V. The fast internal crack propagation rate in FP material can be the superficial reason for the peculiar early fatigue life of internal fracture in FP materials.

On the other hand, comparing the significant difference of internal crack propagation rate between FP material and Ti-6Al-4V, their surface propagation rate do not exhibit apparent difference. In other words, the difference between the surface and internal crack propagation rate is much less in FP material than in Ti-6Al-4V, and the instinct explanation for this phenomenon remain unclear.

As mentioned in the Introduction, a major difference between the surface and internal cracks is the surrounding environment [44]. Surface cracks propagate in the surrounding environment of air, but internal cracks propagate in a vacuum-like environment in which gas adsorption, such as the oxidization process, is missing. Consequently, the absence of gas adsorption near the crack tip increased crack closures from plastic deformation (plastic-induced crack closure, PICC) and rough surface contact (roughness-induced crack closure, RICC) [76,77]. Moreover, the lack of new formed oxide layer can decrease the slip irreversibility [78,79], which slows the propagation rate. In addition, the vacuum pressure also influences crack propagation. In the previous study on a surface crack growth test in Ti-6Al-4V under vacuum environments, it was found that with a decrease in vacuum pressure, the crack propagation rate decreased, and the internal crack matched the surface crack in a high vacuum level.

Two hypotheses are proposed for faster internal crack propagation in beta titanium alloy. The first is that the vacuum pressure surrounding the internal crack in beta

titanium alloy is at a higher pressure (i.e. lower vacuum level) than Ti-6Al-4V, thus leading to a lower vacuum effect. The second is that the internal crack in beta titanium alloy is surrounded by a similar vacuum pressure to that of Ti-6Al-4V, but the crack growth process in beta titanium alloy is not sensitive to the vacuum pressure, which makes no significant difference in the crack propagation rate between various vacuum pressures. To clarify the above ideas, crack growth tests in various environments for beta titanium alloy conducted and will be introduced in this section.

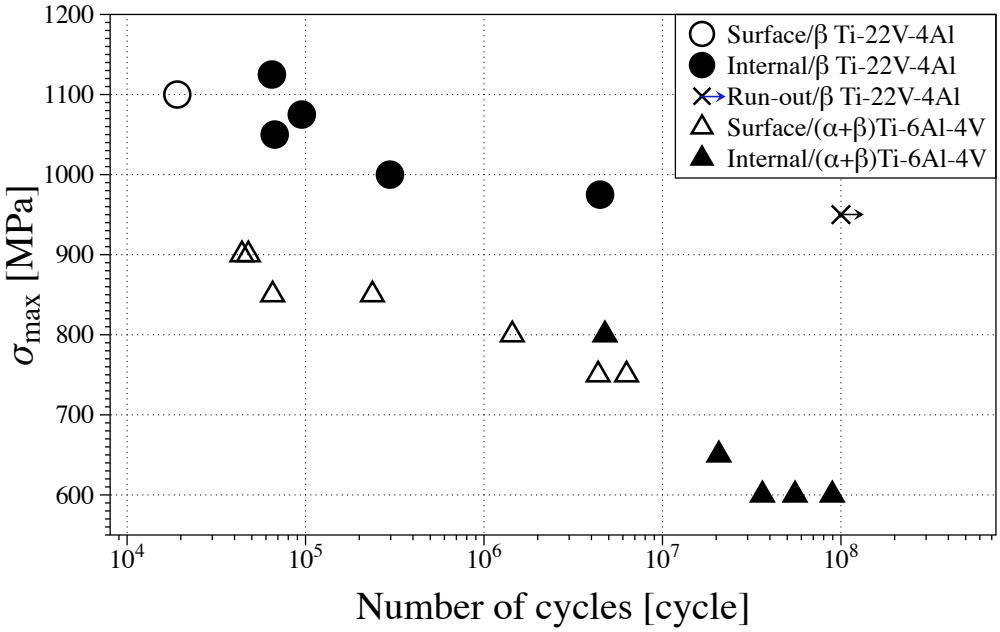



Fig. 6-1. Fatigue properties between beta (FP, Ti-22V-4Al) and (alpha+ beta) titanium alloys (Ti-6Al-4V) in $R$ = 0.1

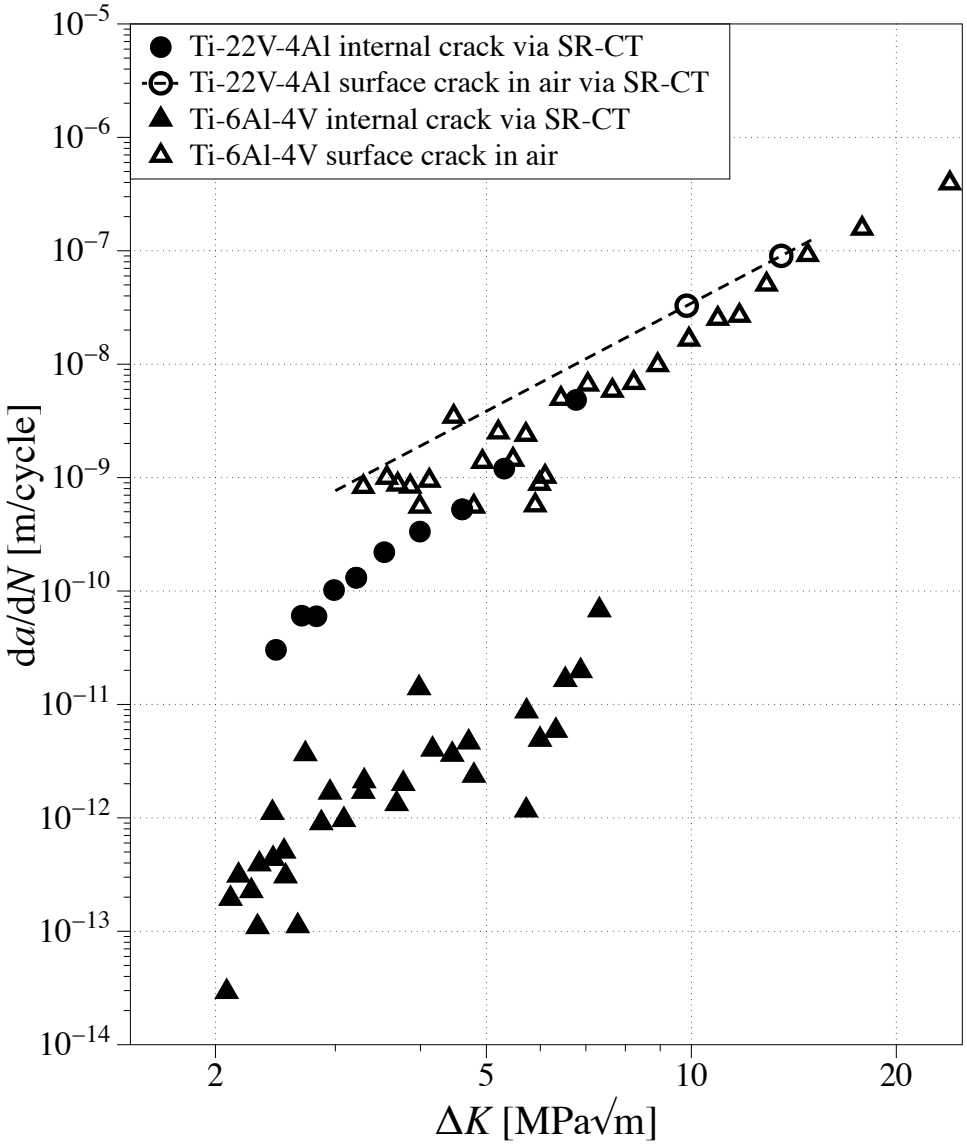



Fig. 6-2. Crack propagation rate of beta titanium alloy Ti-22V-4Al (FP material) and a dual-phase (alpha + beta) titanium alloy Ti-6Al-4V

## 6.2 Methodology

### 6.2.1 Material and Specimen

The beta titanium alloy applied for the crack growth tests in a vacuum was the FP material with a fine and homogeneous alpha-phase precipitation which is the same as the material used in the direct observation experiment of internal fatigue crack observation by SR-CT (see Chapter 5). The specimens were fabricated into an hourglass shape shown in Fig. 6-3 from the heat-treated bars via lathe machining. Then, the specimens were polished with emery paper until #2000 to reach Ø4 × 6 mm straight sections. Finally, straight sections were buffed with diamond abrasive to obtain a mirror surface.

As a crack started, an artificial surface defect was introduced at the center of the straight section. As mentioned in Chapter 2, the crack initiation site in beta titanium alloy is related to the grain size which is about 20 μm for the applied FP material. In this study, a picosecond laser characterized by its negligible heat accumulation due to its short-pulse duration, was used to create a defect with a smaller size. The size of this artificial defect was closer to the actual facet size and more convenient for investigating the crack propagation rate at a lower $\Delta K$. Fig. 6-4 (a) and (b) show the image of the small defect on the fracture surface and the specimen surface, respectively. As shown in Fig. 6-4 (a), the fatigue crack initiated from the artificial defect, which showed a cone-like shape with a depth of around 15 μm. To enable the crack to propagate perpendicular to the loading direction more naturally, the author designed the bottom of the cone to have an elliptic shape, as shown in Fig. 6-4 (b). The lengths of the major axis and minor axis were 20 μm and 10 μm, respectively.

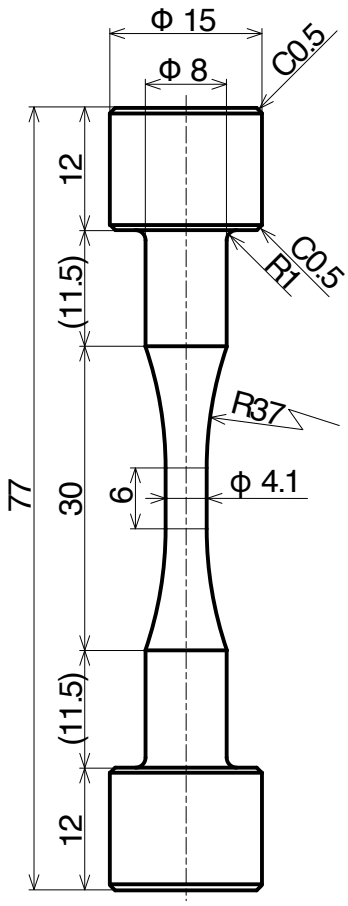
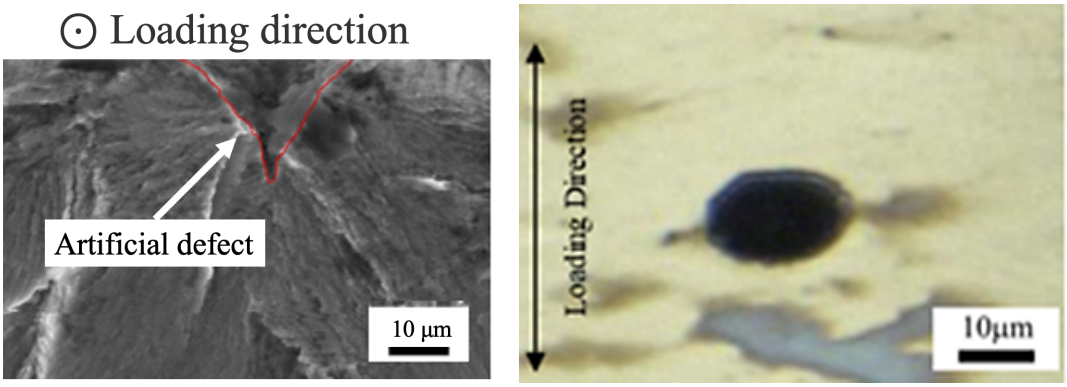



Fig. 6-3. Specimen configuration for the crack growth test in vacuum. (unit: mm)




(a) Shape on the fracture surface. (b) Shape on the specimen surface.

Fig. 6-4. Configuration of the small defect

6.2.2 Experimental setup and conditions

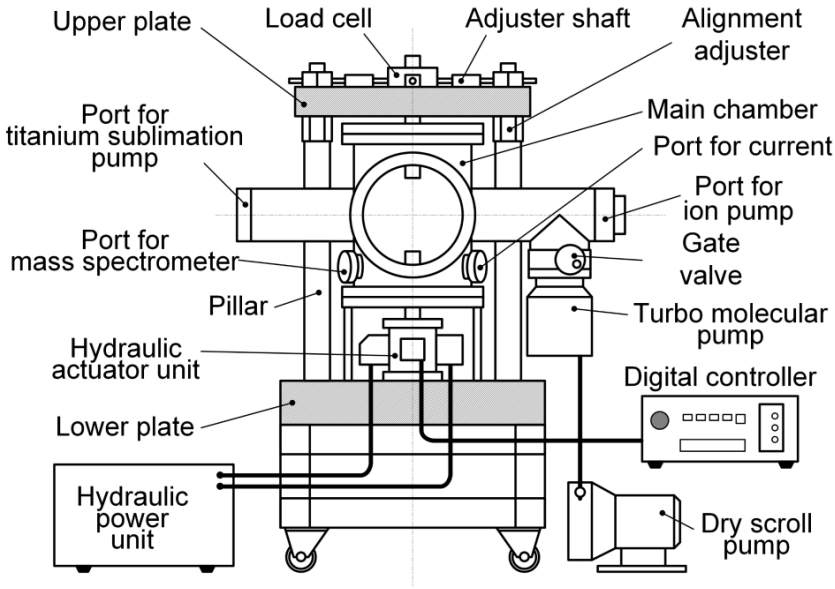
The vacuum fatigue testing machine shown in Fig. 6-5 was used to carry out fatigue tests in vacuum environments. A dry scroll pump and a turbo-molecular pump work concurrently to evacuate the gas in the vacuum chamber. The applied digital controller was developed by MOOG, Japan. In order to observe the crack length and the crack propagation behavior during the fatigue test, the vacuum chamber equipped with a viewport. A digital microscope with a high spatial resolution of submicron order (Keyence VHX-2000) was utilized to capture the image in the vacuum chamber through the viewport as shown in Fig. 6-6.

The crack propagation tests were conducted by the $\Delta K$-increasing test under a constant load amplitude. Tests were carried out at the high vacuum level with a pressure of $1.95\times10^{-5}$ MPa. The tests were carried out under sinusoidal waveform loading at a stress ratio of 0.1 and maximum stress of 1050 MPa, which is the same as the SR-CT experiment mentioned in Chapter 5. The test frequency was 10 Hz. The fatigue test was suspended after specific cycles in order to acquire images of the cracks. The intervals between each imaging step were 500 cycles.

The crack length $2a$ was the measure target which was defined as the length between two crack tips on the specimen surface projected to the plane perpendicular to the loading direction. Other crack parameters, including, crack depth $b$, and the radius of the specimen $r$, are illustrated in Fig. 6-7 which is the same as Fig. 4-5 in Chapter 4. During crack propagation tests, it is assumed that $b$ is equal to $a$ during crack growth and the crack propagated semi-circularly. The sequential $\Delta K$ calculation was consistent with the method applied in Chapter 4.



(a) Setup in the experimental room




(b) Schematic of the testing machine system

Fig. 6-5. The ultra high vacuum fatigue testing machine

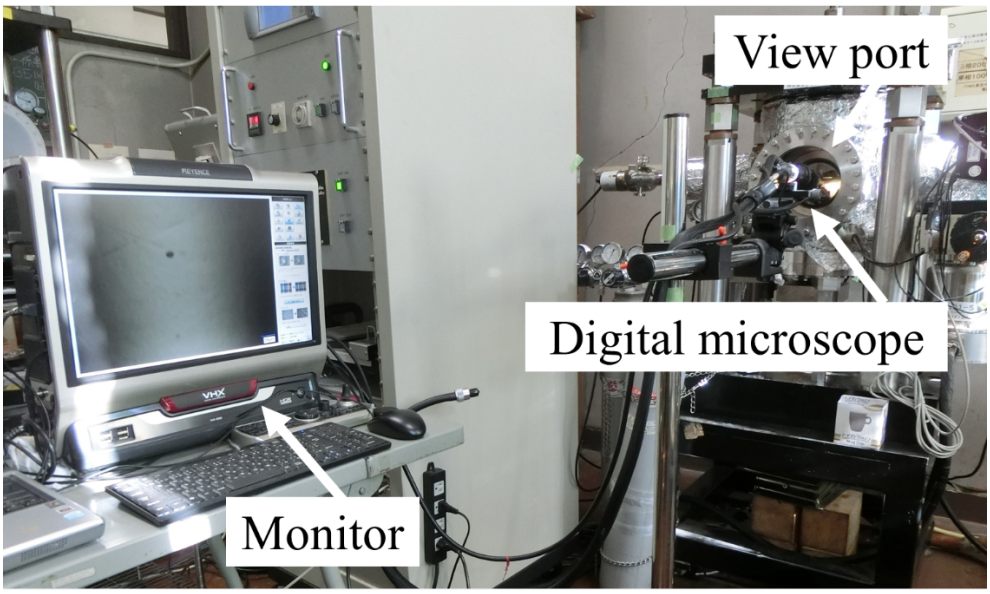



Fig. 6-6. Observation system of the crack growth test in vacuum

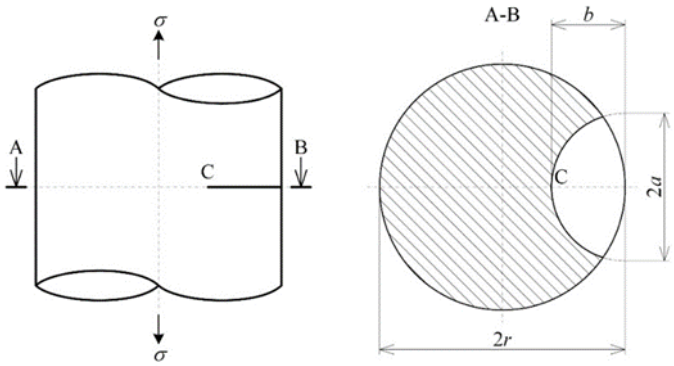



Fig. 6-7. Schematic of crack shape with relevant parameter (the same as Fig. 4-5)

## 6.3 Crack propagation behaviors

### 6.3.1 Relation between crack length and the number of cycles

During the test, small cracks were initiated from the artificial defect at the specimen surface for all specimens. The relationship between the crack length $2a$ and the number of cycles $N$ is demonstrated in Fig. 6-8. The crack initiation and specimen fracture were observed at 10000 cycles and 19666 cycles, respectively, thus the crack propagation life is 9666 (19666-10000) cycles. Because the crack propagation in vacuum was activated by an artificial defect which means the formation of facet was skipped. Therefore, the propagation life in the vacuum was comparable to the number of cycles in the Stage II-internal regime from the SR-CT observation which was 11000 cycles (see Section 5.4.2).

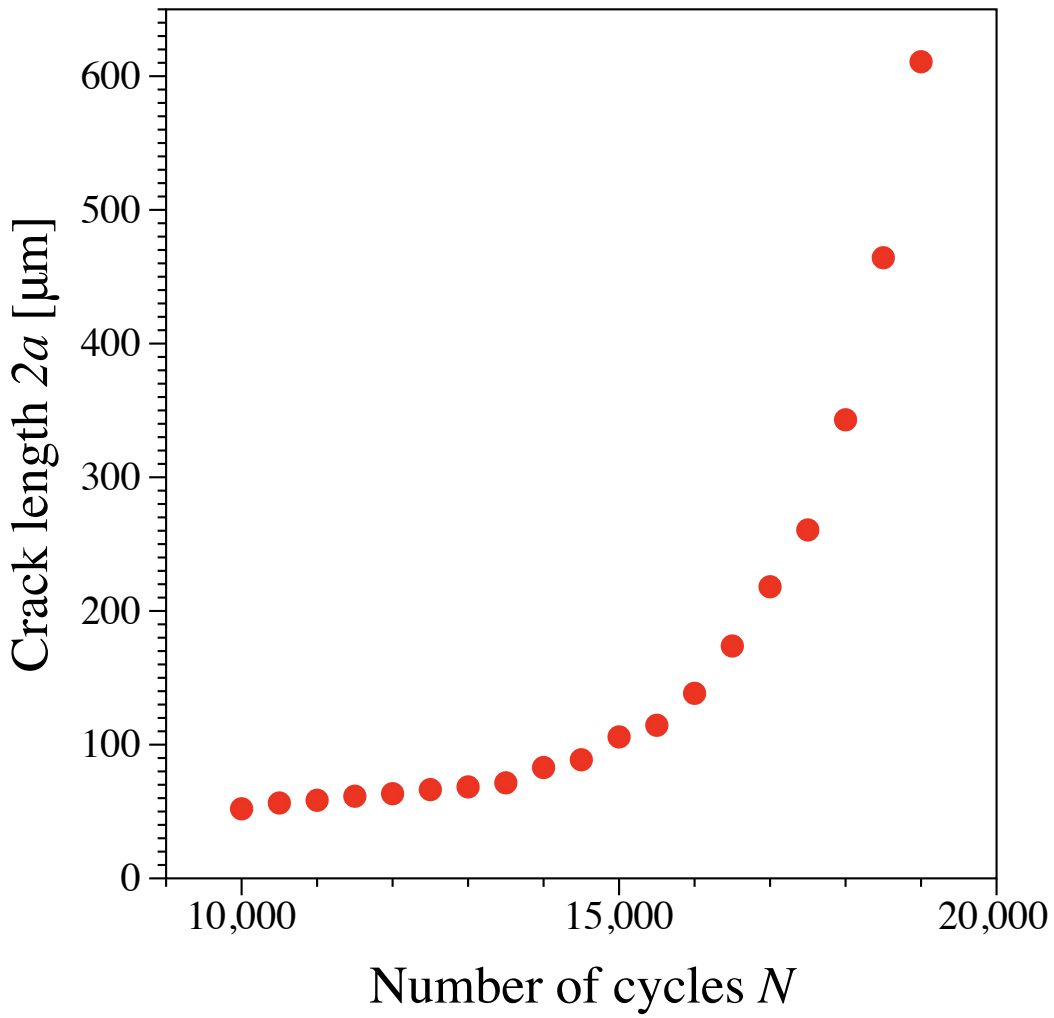



Fig. 6-8. Relationship between the crack length 2*a* and the number of cycles *N* (FP material)

### 6.3.2 Crack propagation rate

The crack propagation rate of beta titanium alloy in a high vacuum is plotted in Fig. 6-9 with those from SR-CT observation. The surface crack from SR-CT represent the crack behaviors in air. It is seen that the crack propagation rate of high vacuum is slower than that of in air but is in good agreement with the internal crack. These results indicate that the vacuum environment can slow down the crack propagation in beta titanium alloy, and the vacuum level surrounding internal fatigue cracks in FP material could be a high vacuum level which is consistent with that of Ti-6Al-4V.

Moreover, the crack propagation rate of surface cracks in the air and high vacuum of beta titanium alloy are compared with those of Ti-6Al-4V in Fig. 6-10. As for the crack propagation rate in air, beta titanium alloy in FP is slightly faster than that of Ti-6Al-4V. However, in the case of high vacuum, with the decrease of $\Delta K$, crack propagation rate of Ti-6Al-4V decrease more significantly than beta titanium alloy. As a result, crack in high vacuum level propagates 20~1000 times faster in beta titanium alloy than in Ti-6Al-4V. In other words, the difference between crack propagation rate in air and high vacuum is much less in beta titanium alloy than Ti-6Al-4V. Therefore, it can be concluded that the crack propagation in FP material is less sensitive to the vacuum environment than Ti-6Al-4V.

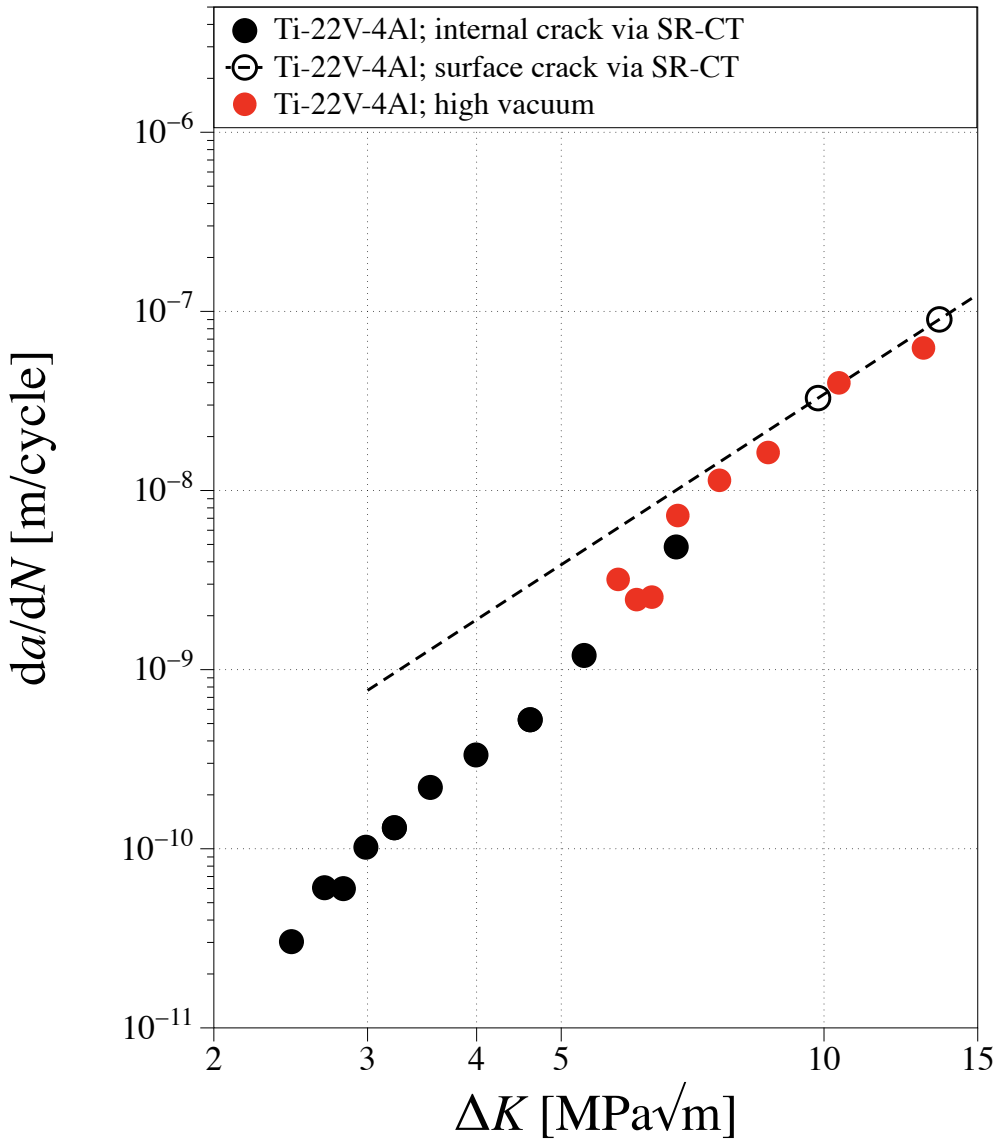



Fig. 6-9. Relationship between crack propagation rate d$a$/d$N$ and stress intensity factor range $\Delta K$ with the surface crack in a high vacuum, surface crack (in air) by SR-CT and the internal crack by SR-CT (FP material)

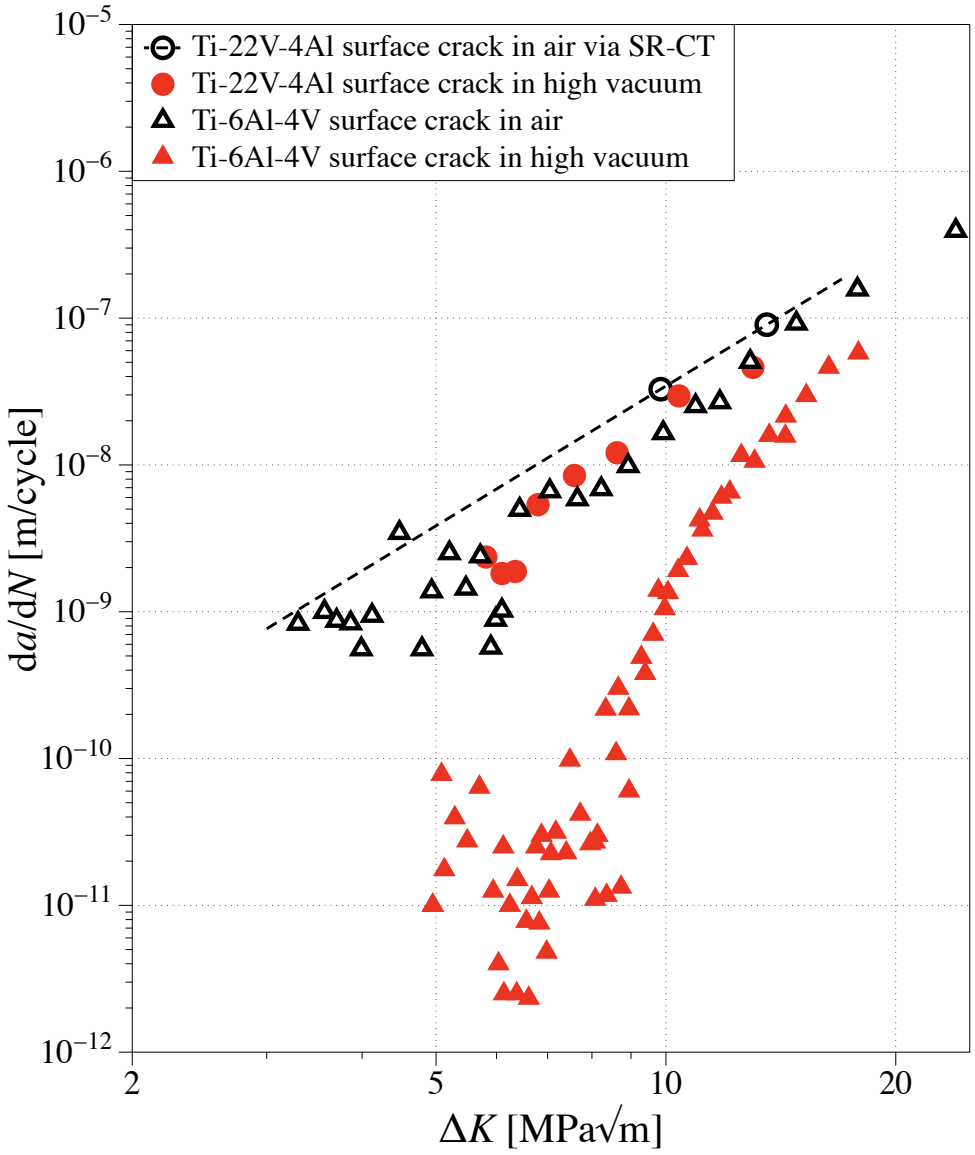



Fig. 6-10. Relationship between crack propagation rate d$a$/d$N$ and stress intensity factor range $\Delta K$ with the surface crack in air and a high vacuum for beta titanium alloy (FP material) and Ti-6Al-4V

6.4 Microstructural factors in beta and (alpha + beta) titanium alloys related to various vacuum sensitivity on crack propagation

As mentioned in Section 6.1, the vacuum effects of slowing the crack propagation are mostly based on increasing the crack closure and weakening the slip irreversibility. In this section, the reason for the different vacuum sensitivity will be discussed for the microstructure of beta and (alpha + beta) titanium alloy. The microstructures of the vacuum-tested (alpha + beta) titanium alloy Ti-6Al-4V are exhibited in Fig. 6-11. Compared with beta titanium alloy with FP (Fig. 2-1 (a)), the dual phase Ti-6Al-4V has smaller grains and a more complex phase arrangement, which could enhance the effect of vacuum in crack propagation.

First, smaller grains mean more chances of grain boundary blocking during crack propagation. From the result of beta titanium alloy in Section 5.5, when the crack tip is facing high resistance for propagation such as grain boundary, plasticity saturation at the crack tip is necessary which consumes 81% of crack propagation life. Assuming this behavior also exists in Ti-6Al-4V, more grain boundary blocking would lead to a longer fatigue life consumed by plastic saturation at the crack tip. Moreover, in a vacuum environment, the material has a greater capacity for plastic deformation. In other words, the plasticity saturation could take more number of loading cycles to be achieved in a vacuum than in air. Therefore, the effect of grain boundary blocking could be magnified more in Ti-6Al-4V than in beta titanium alloy with FP.

Then, in Ti-6Al-4V, complex phase arrangement provides complex crack paths, leading to a rough fracture surface. An example of a rough fracture surface is exhibited in Fig. 6-12 [44]. The Stage II-a referred to as the "rough area" [80], which is comparable with the Stage II-internal (characterized by smooth area) of beta titanium alloy mentioned in Chapter 5. Therefore, compared with the smooth fracture surface

in beta titanium alloy with FP, such rough morphology of fracture surface in Ti-6Al-4V would increase the RICC, thus slow down the crack propagation rate, resulting a larger difference in crack propagation rate between the above two materials.

In addition, precipitates in beta titanium alloy also need to be taken into account since they might reduce slip reversibility and the vacuum effect on crack propagation. For a material without precipitates, in one loading cycle (i.e. $\sigma_{min} \rightarrow \sigma_{max} \rightarrow \sigma_{min}$), a fresh surface will be created by the slip deformation on the fracture surface. In air environment, the oxide layer could be instantly formed on the fresh surface, acting as an obstacle to block the reverse slip. Therefore, all the segments of the fresh surface could be considered as effective deformation in one loading cycle. In the case of a vacuum, the absence of an oxide layer leads to the reverse slip being unstoppable, thus the effective deformation in one loading cycle is less than that in air. On the other hand, for a material with precipitates, precipitates might be embedded on the fresh surface which can also act as obstacles for reverse slip. Therefore, even if there is no oxide layer in the vacuum, the reverse slip could still be suppressed by the precipitates, resulting in fast crack propagation. The relatively later fatigue life of internal fracture for CP material with less precipitation than FP material illustrated in Fig. 2-6 might be one of the proofs for the effect of precipitates on slip reversibility. However, it is important to note that precipitation hardening is widely used for enhancing the mechanical properties of structural metals such as titanium and aluminum alloys. Therefore, the trade-off between mechanical properties and fatigue properties needs to be considered in metallurgy and heat treatment fields.

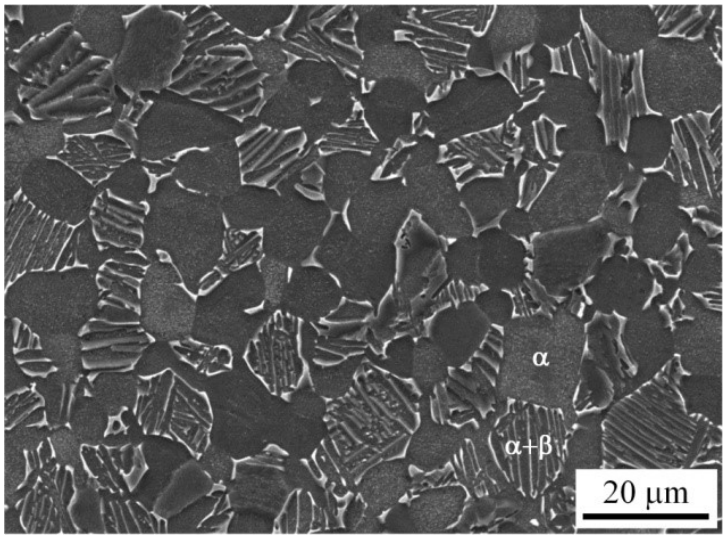
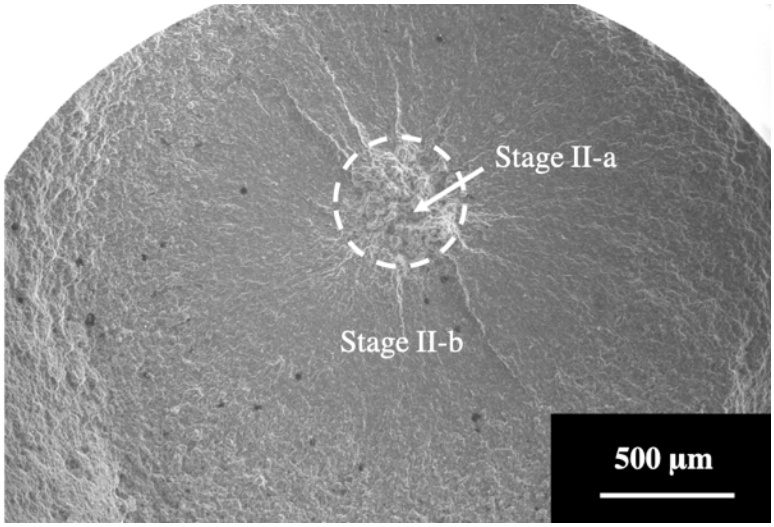
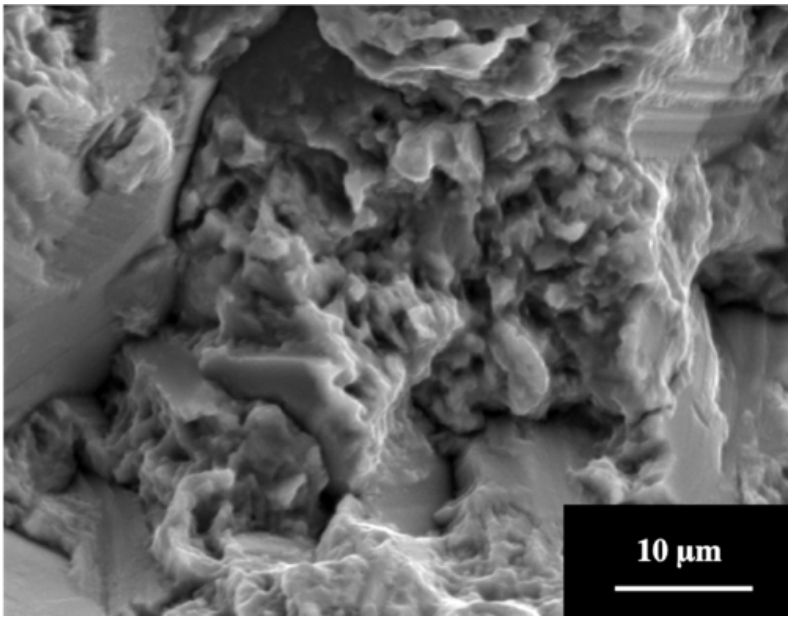



Fig. 6-11. Dual-phase (alpha + beta) titanium alloy Ti-6Al-4V with equiaxed alpha grains and grains containing alternating lamellae of alpha and beta phases. Ave. grain size is 10 μm




(a) Low magnification image




(b) High magnification image in Stage II-a

Fig. 6-12. Fracture surface image of an internal crack in Ti-6Al-4V ($R$ = 0.1, $\sigma_{max}$= 600 MPa, $f$ = 120 Hz)

## 6.5 Summary of Chapter 6

The internal crack propagation rate was found much faster in FP material than in Ti-6Al-4V, which is one of the reason for the peculiar early fatigue life of internal fracture in FP material.

It was also found that the difference of crack propagation rate between surface and internal crack is much less in FP material than in Ti-6Al-4V. Based on the concepts of internal crack surrounded by a vacuum environment and the vacuum pressure may affect on the crack propagation rate, surface crack propagation test in high vacuum was conducted in FP material. The purpose is to clarify whether the less difference between the surface and internal crack in FP material is caused by the low vacuum environment or the less vacuum sensitivity from the microstructure. Surprisingly, the internal crack propagation rate was in agreement with the surface crack in a high vacuum, which is the consistent result with Ti-6Al-4V. Therefore, the low vacuum sensitivity of FP microstructure could account for the less difference between surface and internal crack. The relationship between microstructural factors with vacuum sensitivity was discussed for both Ti-6Al-4V and FP material. In Ti-6Al-4V, some evidences shows that the small grains with complex phase arrangements could enhance the vacuum sensitivity. In contrast, the precipitates in FP materials might be responsible for the low vacuum sensitivity by reducing the slip reversibility in a vacuum.

# Chapter 7

# Conclusions

# 7. Conclusions

This study integrally investigated the characteristics of internal fatigue fractures from a small crack regime through fractography, direct observation via s multiscale X-ray CT, and replicating internal fatigue crack behaviors by surface crack growth tests in a vacuum. The following conclusions were drawn.

1. Fatigue properties were investigated for beta titanium alloy Ti-22V-4Al with two different microstructures: FP and CP materials. The *S*-*N* curves under negative stress ratios exhibit a step-wise shape with a fatigue limit of the surface fracture. However, under a positive stress ratio, the fatigue limit of the surface fracture becomes less remarkable, and the *S*-*N* curve exhibited an asymptote shape with a missing of "knee point". In addition, under the stress ratio of 0.1, the internal fatigue fracture could be found from $10^5$ cycles which was much earlier than the VHCF regime. On the fracture surface of both FP and CP material, multiple facets could be found at the crack initiation site, while surrounded by the smooth area. The concepts of major and minor facet(s) and the classification of the facet bonding patterns were established to differentiate the various characteristics of the multiple facets. (Chapter 2)

2. Multiscale X-ray CT including micro-CT and nano-CT located at BL20XU, SPring-8 were conducted to non-destructively observe the interior of beta titanium alloys. A small specimen with a diameter ~ 0.7 mm was designed to fulfill sufficient X-ray transmittance for multiscale SR-CT. The imaging conditions were optimized for micro-/nano-CT individually using a needle shape specimen made from CP material. (Chapter 3)

3. An in situ piezoelectric fatigue testing system was developed for continuously observing the crack growth behaviors. By the attempt on a small surface crack growth test using CP material, the crack initiation distribution, evolution of crack shape, and

interaction between crack tip with local microstructure were successfully obtained. The crack shape was uneven in the early crack growth stage, but it has minimal effect on describing crack propagation rate with the corresponding stress intensity factors. (Chapter 4)

4. The full-life growth process of an internal fatigue crack was monitored by multiscale CT in FP material. Multiple facets formed sequentially, rather than simultaneously. The crack propagation at 45° associated with multiple facets, described as Stage I, occupied 95% of *N*p and was therefore the dominant crack propagation process of the internal fracture. The internal crack propagation in the matrix (Stage II-internal) and the surface crack propagation in the matrix (Stage II-surface) were represented by the smooth area and rough texture on the fracture surface, respectively. Stages II-internal and II-surface accounted for only 4% and 1% of *N*p, respectively. Therefore, the distance from the facet to the specimen surface was not a critical factor for internal fractures in beta titanium alloys. The internal crack propagation rate was measured for each crack growth stage individually and was found to be lower than that of a surface crack at the same $\Delta K$, with a maximum difference of two orders of magnitude in the low $\Delta K$ regime. (Chapter 5)

6. In beta titanium alloy, the internal crack propagation rate was found to be much faster, and the difference in propagation rate between the surface and internal fatigue crack is much smaller than in the Ti-6Al-4V. This could be one of the reasons for the peculiar early fatigue life of internal fracture and the missing of "knee point" in the *S*-*N* curves of beta titanium alloys. The vacuum environment surrounding the internal crack was found to be a high vacuum level in both beta titanium alloy and Ti-6Al-4V. Therefore, the less difference between surface and internal crack propagation rate could be caused by the relatively low vacuum sensitivity on crack propagation in beta

titanium alloy. Microstructural factors in Ti-6Al-4V, including grain size and phase arrangement, might increase its vacuum sensitivity. On the other hand, precipitates in beta titanium alloy, which play an important role in enhancing the mechanical properties, might accelerate the internal crack propagation. Therefore, the trade-off between mechanical properties and fatigue properties needs to be considered in the future. (Chapter 6)

# Reference


[1] Oguma H, Nakamura T. The effect of microstructure on very high cycle fatigue properties in Ti–6Al–4V. Scr Mater 2010;63:32–4. https://doi.org/10.1016/J.SCRIPTAMAT.2010.02.043.

[2] Neal DF, Blenkinsop PA. Internal fatigue origins in α-β titanium allols. Acta Metallurgica 1976;24:59–63. https://doi.org/10.1016/0001-6160(76)90147-4.

[3] Marines I, Bin X, Bathias C. An understanding of very high cycle fatigue of metals. Int J Fatigue 2003;25:1101–7. https://doi.org/10.1016/S0142-1123(03)00147-6.

[4] Furuya Y. Effects of mns on gigacycle fatigue properties of SCM440 steel. Tetsu-To-Hagane/Journal of the Iron and Steel Institute of Japan 2020;106:799–806. https://doi.org/10.2355/TETSUTOHAGANE.TETSU-2020-051.

[5] Murakami Y, Kodama S, Konuma S. Quantitative evaluation of effects of non-metallic inclusions on fatigue strength of high strength steels. I: Basic fatigue mechanism and evaluation of correlation between the fatigue fracture stress and the size and location of non-metallic inclusions. Int J Fatigue 1989;11:291–8. https://doi.org/10.1016/0142-1123(89)90054-6.

[6] Atrens A, Hoffelner W, Duerig TW, Allison JE. Subsurface crack initiation in high cycle fatigue in Ti6A14V and in a typical martensitic stainless steel. Scripta Metallurgica 1983;17:601–6. https://doi.org/10.1016/0036-9748(83)90385-X.

[7] Masuda K, Oguma N, Ishihara S, McEvily AJ. Investigation of subsurface fatigue crack growth behavior of D2 tool steel (JIS SKD11) based on a novel measurement method. Int J Fatigue 2020;133. https://doi.org/10.1016/j.ijfatigue.2019.105395.

[8] Sun C, Song Q, Zhou L, Pan X. Characteristic of interior crack initiation and early growth for high cycle and very high cycle fatigue of a martensitic stainless steel. Materials Science and Engineering A 2019;758:112–20. https://doi.org/10.1016/J.MSEA.2019.04.015.

[9] Shiozawa K, Lu L, Ishihara S. S-N curve characteristics and subsurface crack initiation behaviour in ultra-long life fatigue of a high carbon-chromium bearing steel. Fatigue Fract Eng Mater Struct 2001;24:781–90. https://doi.org/10.1046/j.1460-2695.2001.00459.x.

[10] Tokaji K, Ohya K, Kariya H. Subsurface fatigue crack initiation in beta titanium alloys. Fatigue Fract Eng Mater Struct 2000;23:759–66. https://doi.org/10.1046/j.1460-2695.2000.00325.x.
[11] Shiozawa K, Kuroda Y, Nishino S. Effect of stress ratio on subsurface fatigue crack initiation behavior of beta-type titanium alloy. Nihon Kikai Gakkai Ronbunshu, A Hen/Transactions of the Japan Society of Mechanical Engineers, Part A 1998;64:2528–35. https://doi.org/10.1299/kikaia.64.2528.
[12] Serrano-Munoz I, Buffiere JY, Verdu C, Gaillard Y, Mu P, Nadot Y. Influence of surface and internal casting defects on the fatigue behaviour of A357-T6 cast aluminium alloy. Int J Fatigue 2016;82:361–70. https://doi.org/10.1016/J.IJFATIGUE.2015.07.032.
[13] Liu Y, Chen Y, He C, Liu F, Yang K, Li L, et al. Vacuum retarding and air accelerating effect on the high-cycle and very-high-cycle fatigue behavior of a ZK60 magnesium alloy. Mater Des 2021;198:109310. https://doi.org/10.1016/J.MATDES.2020.109310.
[14] Cotton JD, Briggs RD, Boyer RR, Tamirisakandala S, Russo P, Shchetnikov N, et al. State of the art in beta titanium alloys for airframe applications. JOM 2015;67:1281–303. https://doi.org/10.1007/s11837-015-1442-4.
[15] Weiss I, Semiatin SL. Thermomechanical processing of beta titanium alloys—an overview. Materials Science and Engineering: A 1998;243:46–65. https://doi.org/10.1016/S0921-5093(97)00783-1.
[16] Kolli RP, Devaraj A. A review of metastable beta titanium alloys. Metals (Basel) 2018;8. https://doi.org/10.3390/met8070506.
[17] Boyer RR, Briggs RD. The use of β titanium alloys in the aerospace industry. J Mater Eng Perform 2005;14:681–5. https://doi.org/10.1361/105994905X75448.
[18] Ivasishin OM, Markovsky PE, Matviychuk Y V., Semiatin SL, Ward CH, Fox S. A comparative study of the mechanical properties of high-strength β-titanium alloys. J Alloys Compd 2008;457:296–309. https://doi.org/10.1016/j.jallcom.2007.03.070.
[19] Sakamoto T, Takiue K, Higaki Y, Kobayashi S, Nakai K. Effects of α Phase Nucleating at Transition Phase and Dislocation on Mechanical Properties in Metastable β Titanium Alloy Ti-6.8Mo-4.5Fe-1.5Al. Mater Trans 2017;58:986–92. https://doi.org/10.2320/matertrans.M2016382.
[20] Nakai M, Niinomi M, Oneda T. Improvement in fatigue strength of biomedical β-type Ti-Nb-Ta-Zr alloy while maintaining low young's modulus

through optimizing ω-phase precipitation. Metall Mater Trans A Phys Metall Mater Sci 2012;43:294–302. https://doi.org/10.1007/s11661-011-0860-3.

[21] Fan JK, Li JS, Kou HC, Hua K, Tang B. The interrelationship of fracture toughness and microstructure in a new near β titanium alloy Ti-7Mo-3Nb-3Cr-3Al. Mater Charact 2014;96:93–9. https://doi.org/10.1016/j.matchar.2014.07.018.

[22] Jha SK, Ravichandran KS. High-cycle fatigue resistance in beta-titanium alloys. Jom 2000;52:30–5. https://doi.org/10.1007/s11837-000-0097-x.

[23] Qiu J, Feng X, Ma Y, Lei J, Liu Y, Huang A, et al. Fatigue crack growth behavior of beta-annealed Ti-6Al-2Sn-4Zr-xMo (x = 2, 4 and 6) alloys: Influence of microstructure and stress ratio. Int J Fatigue 2016;83:150–60. https://doi.org/10.1016/j.ijfatigue.2015.10.009.

[24] Kocan M, Rack HJ, Wagner L. Fatigue performance of metastable β titanium alloys: Effects of microstructure and surface finish. J Mater Eng Perform, vol. 14, Springer; 2005, p. 765–72. https://doi.org/10.1361/105994905X75583.

[25] Huang C, Zhao Y, Xin S, Tan C, Zhou W, Li Q, et al. Effect of microstructure on high cycle fatigue behavior of Ti–5Al–5Mo–5V–3Cr–1Zr titanium alloy. Int J Fatigue 2017;94:30–40. https://doi.org/10.1016/j.ijfatigue.2016.09.005.

[26] Kazuaki S. effect of stress ratio on subsurface fatigue crack initiation behavior of beta-type titanium alloy. JSME Annual Meeting 2009;2009:157–8. https://doi.org/10.1002/adma.200400767.

[27] Xue G, Nakamura T, Fujimura N, Takahashi K, Oguma H. Initiation and propagation processes of internal fatigue cracks in β titanium alloy based on fractographic analysis. Applied Sciences 2020;11:131. https://doi.org/10.3390/app11010131.

[28] Osovski S, Srivastava A, Williams JC, Needleman A. Grain boundary crack growth in metastable titanium β alloys. Acta Mater 2015;82:167–78. https://doi.org/10.1016/j.actamat.2014.08.062.

[29] Tokaji K, Kariya H. Mean stress dependence of fatigue strength and subsurface crack initiation in Ti-15Mo-5Zr-3Al alloy. Materials Science and Engineering A 2000;281:268–74. https://doi.org/10.1016/S0921-5093(99)00710-8.

[30] Wu Z, Kou H, Chen N, Zhang Z, Qiang F, Fan J, et al. Microstructural influences on the high cycle fatigue life dispersion and damage mechanism in a metastable β titanium alloy. J Mater Sci Technol 2021;70:12–23. https://doi.org/10.1016/j.jmst.2020.07.018.

[31] Campanelli LC, da Silva PSCP, Bolfarini C. High cycle fatigue and fracture behavior of Ti-5Al-5Mo-5V-3Cr alloy with BASCA and double aging treatments. Materials Science and Engineering A 2016;658:203–9. https://doi.org/10.1016/j.msea.2016.02.004.

[32] Uematsu Y, Kakiuchi T, Hattori K. EBSD-assisted fractography of sub-surface fatigue crack initiation mechanism in the ultrasonic-shot-peened βeta-type titanium alloy. Fatigue Fract Eng Mater Struct 2018;41:2239–48. https://doi.org/10.1111/ffe.12812.

[33] Tokaji K, Takafuji S, Ohya K, Kato Y, Mori K. Fatigue behaviour of beta Ti-22V-4Al alloy subjected to surface-microstructural modification. J Mater Sci 2003;38:1153–9. https://doi.org/10.1023/A:1022880914473.

[34] Berg A, Drechsler A, Wagner L. Fatigue Behavior of Titanium Alloys 1999.

[35] Benedetti M, Fontanari V, Lütjering G, Albrecht J. The effect of notch plasticity on the behaviour of fatigue cracks emanating from edge-notches in high-strength β-titanium alloys. Eng Fract Mech 2008;75:169–87. https://doi.org/10.1016/j.engfracmech.2007.03.037.

[36] Tanaka K, Akiniwa Y. Fatigue crack propagation behaviour derived from S-N data in very high cycle regime. Fatigue Fract Eng Mater Struct 2002;25:775–84. https://doi.org/10.1046/j.1460-2695.2002.00547.x.

[37] Furuya Y. Small internal fatigue crack growth rate measured by beach marks. Materials Science and Engineering A 2016;678:260–6. https://doi.org/10.1016/j.msea.2016.09.109.

[38] Furuya Y. A new model for predicting the gigacycle fatigue strength of high-strength steels. Materials Science and Engineering A 2019;743:445–52. https://doi.org/10.1016/j.msea.2018.11.109.

[39] Oguma H, Nakamura T. Fatigue crack propagation properties of Ti-6Al-4V in vacuum environments. Int J Fatigue 2013;50:89–93. https://doi.org/10.1016/j.ijfatigue.2012.02.012.

[40] YOSHINAKA F, NAKAMURA T. Effect of vacuum environment on fatigue fracture surfaces of high strength steel. Mechanical Engineering Letters 2016;2:15–00730. https://doi.org/10.1299/MEL.15-00730.

[41] Nakamura T, Oguma H, Shinohara Y. The effect of vacuum-like environment inside sub-surface fatigue crack on the formation of ODA fracture surface in high strength steel. Procedia Eng 2010;2:2121–9. https://doi.org/10.1016/J.PROENG.2010.03.228.

[42] Snowden KU. The effect of atmosphere on the fatigue of lead. Acta Metallurgica 1964;12:295–303. https://doi.org/10.1016/0001-6160(64)90205-6.

[43] Gao M, Wei RP, Pao PS. Chemical and metallurgical aspects of environmentally assisted fatigue crack growth in 7075-T651 aluminum alloy. Metallurgical Transactions A 1988;19:1739–50. https://doi.org/10.1007/BF02645142/METRICS.

[44] Yoshinaka F, Xue G, Fujimura N, Nakamura T. Effect of vacuum pressure on small crack propagation in Ti-6Al-4V. Int J Fatigue 2021;142:105961. https://doi.org/10.1016/j.ijfatigue.2020.105961.

[45] Hu YN, Wu SC, Withers PJ, Zhang J, Bao HYX, Fu YN, et al. The effect of manufacturing defects on the fatigue life of selective laser melted Ti-6Al-4V structures. Mater Des 2020;192:108708. https://doi.org/10.1016/j.matdes.2020.108708.

[46] Serrano-Munoz I, Buffiere JY, Verdu C. Casting defects in structural components: Are they all dangerous? A 3D study. Int J Fatigue 2018;117:471–84. https://doi.org/10.1016/J.IJFATIGUE.2018.08.019.

[47] Wu Z, Wu S, Bao J, Qian W, Karabal S, Sun W, et al. The effect of defect population on the anisotropic fatigue resistance of AlSi10Mg alloy fabricated by laser powder bed fusion. Int J Fatigue 2021;151:106317. https://doi.org/10.1016/j.ijfatigue.2021.106317.

[48] Guo Y, Burnett TL, McDonald SA, Daly M, Sherry AH, Withers PJ. 4D imaging of void nucleation, growth, and coalescence from large and small inclusions in steel under tensile deformation. J Mater Sci Technol 2022;123:168–76. https://doi.org/10.1016/J.JMST.2022.01.024.

[49] Wu S, Xiao T, Withers PJ. The imaging of failure in structural materials by synchrotron radiation X-ray microtomography. Eng Fract Mech 2017;182:127–56. https://doi.org/10.1016/j.engfracmech.2017.07.027.

[50] Qian W, Wu S, Wu Z, Ahmed S, Zhang W, Qian G, et al. In situ X-ray imaging of fatigue crack growth from multiple defects in additively manufactured AlSi10Mg alloy. Int J Fatigue 2022;155:106616. https://doi.org/10.1016/J.IJFATIGUE.2021.106616.

[51] Messager A, Junet A, Palin-Luc T, Buffiere JY, Saintier N, Ranc N, et al. In situ synchrotron ultrasonic fatigue testing device for 3D characterisation of internal crack initiation and growth. Fatigue Fract Eng Mater Struct 2020;43:558–67. https://doi.org/10.1111/ffe.13140.

[52] King A, Ludwig W, Herbig M, Buffire JY, Khan AA, Stevens N, et al. Three-dimensional in situ observations of short fatigue crack growth in magnesium. Acta Mater 2011;59:6761–71. https://doi.org/10.1016/j.actamat.2011.07.034.
[53] Yoshinaka F, Nakamura T, Takeuchi A, Uesugi M, Uesugi K. Initiation and growth behaviour of small internal fatigue cracks in Ti-6Al-4V via synchrotron radiation microcomputed tomography. Fatigue Fract Eng Mater Struct 2019;42:2093–105. https://doi.org/10.1111/ffe.13085.
[54] Xue G, Nakamura T, Fujimura N, Takahashi K, Oguma H, Takeuchi A, et al. Initiation and propagation of small fatigue crack in beta titanium alloy observed through synchrotron radiation multiscale computed tomography. Eng Fract Mech 2022;263:108308. https://doi.org/10.1016/j.engfracmech.2022.108308.
[55] Chapman TP, Kareh KM, Knop M, Connolley T, Lee PD, Azeem MA, et al. Characterisation of short fatigue cracks in titanium alloy IMI 834 using X-ray microtomography. Acta Mater 2015;99:49–62. https://doi.org/10.1016/j.actamat.2015.07.069.
[56] Takeuchi A, Suzuki Y. Recent progress in synchrotron radiation 3D-4D nano-imaging based on X-ray full-field microscopy. Microscopy 2020;69:259–79. https://doi.org/10.1093/jmicro/dfaa022.
[57] Takeuchi A, Uesugi K, Uesugi M, Toda H, Hirayama K, Shimizu K, et al. High-energy X-ray nanotomography introducing an apodization Fresnel zone plate objective lens. Review of Scientific Instruments 2021;92:023701. https://doi.org/10.1063/5.0020293.
[58] Xue G, Tomoda Y, Nakamura T, Fujimura N, Takahashi K, Yoshinaka F, et al. Detection of small internal fatigue cracks in Ti-6Al-4V via synchrotron radiation nanocomputed tomography. Fatigue Fract Eng Mater Struct 2022:1–10. https://doi.org/10.1111/ffe.13765.
[59] Takahashi K, Shoya R, Matsuo T, Sato W, Nakamura T, Takeuchi A, et al. X-ray nanoimaging of a transversely embedded carbon fiber in epoxy matrix under static and cyclic loads. Sci Rep 2022;12:1–12. https://doi.org/10.1038/s41598-022-12724-1.
[60] Suzuki Y, Uesugi K, Takimoto N, Fukui T, Aoyama K, Takeuchi A, et al. Construction and commissioning of A 248 m-long beamline with X-ray undulator light source. AIP Conf Proc, vol. 705, American Institute of PhysicsAIP; 2004, p. 344–7. https://doi.org/10.1063/1.1757804.
[61] Takeuchi A, Uesugi K, Uesugi M, Yoshinaka F, Nakamura T. Nondestructive multiscale X-Ray tomography by combining microtomography and high-

energy phase-contrast nanotomography. Microscopy and Microanalysis 2018;24:108–9. https://doi.org/10.1017/s1431927618012928.

[62] Daido Steel Co., Ltd. DAT51 (High Strength β-Titanium Alloy) with improved press workability. n.d. https://www.daido.co.jp/en/products/titanium/strength/index.html (accessed December 19, 2020).

[63] Schneider CA, Rasband WS, Eliceiri KW. NIH Image to ImageJ: 25 years of image analysis. Nat Methods 2012;9:671–5. https://doi.org/10.1038/nmeth.2089.

[64] Pande A, Sainis S, Rajaraman S, Manivasagam G, Nageswara Rao M. Influence of rate of heating to aging temperature on precipitation hardening in a metastable β titanium alloy. Adv Mat Res 2014;1025–1026:445–50. https://doi.org/10.4028/www.scientific.net/AMR.1025-1026.445.

[65] Jha SK, Szczepanski CJ, Golden PJ, Porter WJ, John R. Characterization of fatigue crack-initiation facets in relation to lifetime variability in Ti-6Al-4V. Int J Fatigue 2012;42:248–57. https://doi.org/10.1016/j.ijfatigue.2011.11.017.

[66] Tanaka K, Akiniwa Y, Nakai Y, Wei RP. Modelling of small fatigue crack growth interacting with grain boundary. Eng Fract Mech 1986;24:803–19. https://doi.org/10.1016/0013-7944(86)90266-3.

[67] Lankford J. The growth of small fatigue cracks in 7075–T6 aluminum. Fatigue Fract Eng Mater Struct 1982;5:233–48. https://doi.org/10.1111/j.1460-2695.1982.tb01251.x.

[68] Zhai T, Wilkinson AJ, Martin JW. Crystallographic mechanism for fatigue crack propagation through grain boundaries. Acta Mater 2000;48:4917–27. https://doi.org/10.1016/S1359-6454(00)00214-7.

[69] Nisitani H, Chen DH. Stress intensity factor for a semi-elliptic surface crack in a shaft under tension. Transactions of the Japan Society of Mechanical Engineers Series A 1984;50:1077–82. https://doi.org/10.1299/kikaia.50.1077.

[70] Yoshinaka F, Nakamura T, Takaku K, Sshiozawa D, Nakai Y, Uesugi K. Observation of the initial process of internal fracture in very high cycle fatigue in Ti-6Al-4V by synchrotron radiation μCT imaging. Transactions of the JSME (in Japanese) 2017;83:1–15. https://doi.org/10.1299/transjsme.17-00104.

[71] Pilchak AL. Fatigue crack growth rates in alpha titanium: Faceted vs. striation growth. Scr Mater 2013;68:277–80. https://doi.org/10.1016/J.SCRIPTAMAT.2012.10.041.

[72] Lütjering G, Albrecht J, Sauer C, Krull T. The influence of soft, precipitate-free zones at grain boundaries in Ti and Al alloys on their fatigue and fracture behavior. Materials Science and Engineering A 2007;468–470:201–9. https://doi.org/10.1016/j.msea.2006.07.168.

[73] Brett A. Miller, Roch J. Shipley, Ronald J. Parrington, and Daniel P. Dennies. ASM Handbook Volume 11: Failure Analysis and Prevention. vol. 11. 1987.

[74] Lankford J, Davidson DL. Fatigue crack micromechanisms in ingot and powder metallurgy 7xxx aluminum alloys in air and vacuum. Acta Metallurgica 1983;31:1273–84. https://doi.org/10.1016/0001-6160(83)90189-X.

[75] Anderson TL. Fracture Mechanics: Fundamentals and Applications, Fourth Edition. CRC Press 2017;76:1255–69.

[76] McEvily AJ, Velasquez G. Fatigue crack tip deformation processes as influenced by the environment. Metallurgical Transactions A, Physical Metallurgy and Materials Science 1992;23 A:2211–21. https://doi.org/10.1007/BF02646014.

[77] Sugano M, Kanno S, Satake T. Fatigue behavior of titanium in vacuum. Acta Metallurgica 1989;37:1811–20. https://doi.org/10.1016/0001-6160(89)90066-7.

[78] Pelloux RMN. Crack extension by alternating shear. Eng Fract Mech 1970;1. https://doi.org/10.1016/0013-7944(70)90008-1.

[79] Shyam A, Milligan WW. A model for slip irreversibility, and its effect on the fatigue crack propagation threshold in a nickel-base superalloy. Acta Mater 2005;53:835–44. https://doi.org/10.1016/J.ACTAMAT.2004.10.036.

[80] Liu X, Sun C, Hong Y. Effects of stress ratio on high-cycle and very-high-cycle fatigue behavior of a Ti-6Al-4V alloy. Materials Science and Engineering A 2015;622:228–35. https://doi.org/10.1016/j.msea.2014.09.115.